EFFECTS OF OPERATING DAMAGE OF LABYRINTH SEAL ON SEAL LEAKAGE AND WHEELSPACE HOT GAS INGRESS

A Dissertation

by

JINMING XU

Submitted to the Office of Graduate Studies of
Texas A&M University
in partial fulfillment of the requirements for the degree of

DOCTOR OF PHILOSOPHY

May 2006

Major Subject: Mechanical Engineering

EFFECTS OF OPERATING DAMAGE OF LABYRINTH SEAL ON SEAL LEAKAGE AND WHEELSPACE HOT GAS INGRESS

A Dissertation

by

JINMING XU

Submitted to the Office of Graduate Studies of
Texas A&M University
in partial fulfillment of the requirements for the degree of

DOCTOR OF PHILOSOPHY

Approved by:

Chair of Committee,	David L. Rhode
Committee Members,	Sai Lau
	Malcolm Andrews
	Hamn-Chin Chen
Head of Department,	Dennis L. O'Neal

May 2006

Major Subject: Mechanical Engineering

ABSTRACT

Effects of Operating Damage of Labyrinth Seal
on Seal Leakage and Wheelspace Hot Gas Ingress. (May 2006)
Jinming Xu, B.E., Jiangsu Institute of Petrochemical Technology, China;
M.E., Tsinghua University, China
Chair of Advisory Committee: Dr. David L. Rhode

The labyrinth seal is widely used in turbomachinery to minimize or control leakage between areas of different pressure. The present investigation numerically explored the effect of damage and wear of the labyrinth seal on the turbomachinery flow and temperature fields. Specifically, this work investigated: (1) the effect of rub-groove downstream wall angle on seal leakage, (2) the effect of tooth bending damage on the leakage, (3) the effect of tooth "mushrooming" damage on seal leakage, and (4) the effect of rub-groove axial position and wall angle on gas turbine ingress heating. To facilitate grid generation, an unstructured grid generator named OpenCFD was also developed. The grid generator is written in C++ and generates hybrid grids consisting primarily of Cartesian cells.

This investigation of labyrinth seal damage and wear was conducted using the Reynolds averaged Navier-Stokes equations (RANS) to simulate the flows. The high-Reynolds $k-\epsilon$ model and the standard wall function were used to model the turbulence. STAR-CD was used to solve the equations, and the grids were generated using the new code OpenCFD.

It was found that the damage and wear of the labyrinth seal have a significant effect on the leakage and temperature field, as well as on the flow pattern. The leakage increases significantly faster than the operating clearance increase from the wear. Further, the specific seal configuration resulting from the damage and wear was

found to be important. For example, for pure-bending cases, it was found that the bending curvature and the percentage of tooth length that is bent are important, and that the mushroom radius and tooth bending are important for the mushrooming damage cases. When an abradable labyrinth seal was applied to a very large gas turbine wheelspace cavity, it was found that the rub-groove axial position, and to a smaller degree, rub-groove wall angle, alter the magnitude and distribution of the fluid temperature.

TABLE OF CONTENTS

CHAPTER Page

CHAPTER Page

Page

LIST OF TABLES

LIST OF FIGURES

FIGURE Page

FIGURE Page

FIGURE Page

FIGURE Page

CHAPTER I

INTRODUCTION

A. Background

Among different sealing devices, the labyrinth seal is the most widely used, due to its low-cost, simplicity and reliability. According to the layout of their teeth, labyrinth seals can be classified into two categories: straight-through and stepped. Figure 1 shows the configuration of a stepped labyrinth seal with rub-grooves. Figure 2 gives the meridional view of a wheelspace between a turbine stator and a rotor. One can see three labyrinth seals are used in the wheelspace. One one-tooth labyrinth seal at the inner and outer regions of the wheelspace respectively, while a straight-through three-tooth labyrinth seal is in the middle of the wheelspace. The inner and outer labyrinth seals have no rub-grooves, while the middle one has rub-grooves opposite all the three teeth.

The basic mechanism of the labyrinth seal is well known. When fluid passes through the narrow slot formed by the tooth and the stator housing, a portion of its pressure energy is converted into mean flow kinetic energy. As a result, turbulence is generated due to the intense shear stress. As a fluid particle traverses the subsequent labyrinth chamber, a portion of the turbulence kinetic energy is converted into thermal energy by turbulence dissipation. This cycle of energy conversion repeats at each tooth-cavity unit.

Ideally, the labyrinth teeth and stator housing are non-contacting. But this non-contacting nature is hard to maintain when the turbomachine undergoes a wide range of running conditions that are unavoidable. For example, when a gas turbine

---

´ The journal model is *IEEE Transactions on Automatic Control.*

engine is starting up or shutting down, shaft eccentricity and misalignment often occurs, resulting from the different thermal expansion rates of the rotor and stator, the accumulation of tolerances, rotordynamics, pressure loads and maneuver loads (aircraft engines).

To avoid efficiency loss and mechanical failure, two strategies have been used to allow contact between the labyrinth tooth and the opposite surface. One strategy is to use an abradable material for the surface opposite to the labyrinth teeth. In this case, the teeth cut into the abradable surface and form rub-grooves on it. This is especially true for modern gas turbines which are designed with smaller and smaller pre-rub clearances to obtain low-leakage and high efficiency. The other strategy is to have the teeth made from a soft material, while the opposite surface is made from a regular hardness material. Thus when impact and/or rubbing occurs, the teeth tips will bend or erode away and avoid substantial damage to the opposite surface. With this strategy, damage can appear in many forms, such as tooth tip wear, tooth tip "mushrooming" and permanent tooth bending. The damage depends on the design and material of the teeth and various details of the impact and rub intensity and duration.

The labyrinth seal is used in most turbomachines. Even in a single turbomachine, it is used in many places. The function of the labyrinth seal can be: (1) to minimize the leakage, or (2) to control the leakage to provide necessary cooling air for example. In many cases the labyrinth seal is used to minimize the leakage between a higher pressure region and a lower pressure region. An example of this is the labyrinth seals used between the shrouded blade tip and the casing of a turbomachine. There are other cases, conversely, that the labyrinth seal is used to control, rather than to minimize, the leakage. A typical example where it is used to control the leakage is the labyrinth seal in the wheelspace between the rotating and the stationary component

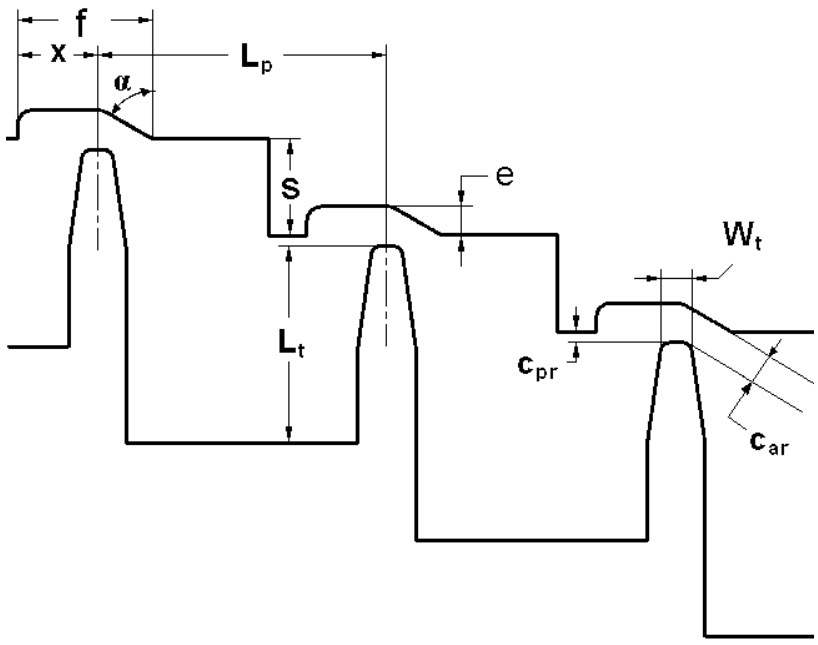

Fig. 1. Geometry and dimensions of the labyrinth seal with rub-groove.

of Fig. 2. Since the application of the labyrinth seal to the wheelspace is to be discussed later, the following paragraphs will provide a general introduction of this.

The labyrinth seal in the wheelspace controls the leakage of the secondary flow, which is used to suppress the ingress of hot gas from the mainstream annulus into the wheelspace. The ingress has long been an anathema for gas turbine designers. The wheelspace, which might consist of several cavities, must accommodate the relative movement between the rotor and stator. The ingestion of hot gas, if not kept within a tolerable range, leads to turbine disc overheating, putting the whole engine into jeopardy. To suppress hot gas ingress, it is a common practice to divert from the compressor a small portion of air, which is relatively cool and under high pressure, to the wheelspace. The bypassed compressor air, commonly referred to as secondary flow, is deprived of power generation. It thus imposes an efficiency penalty to the engine. To achieve an optimal balance between overheating and efficiency, an in-

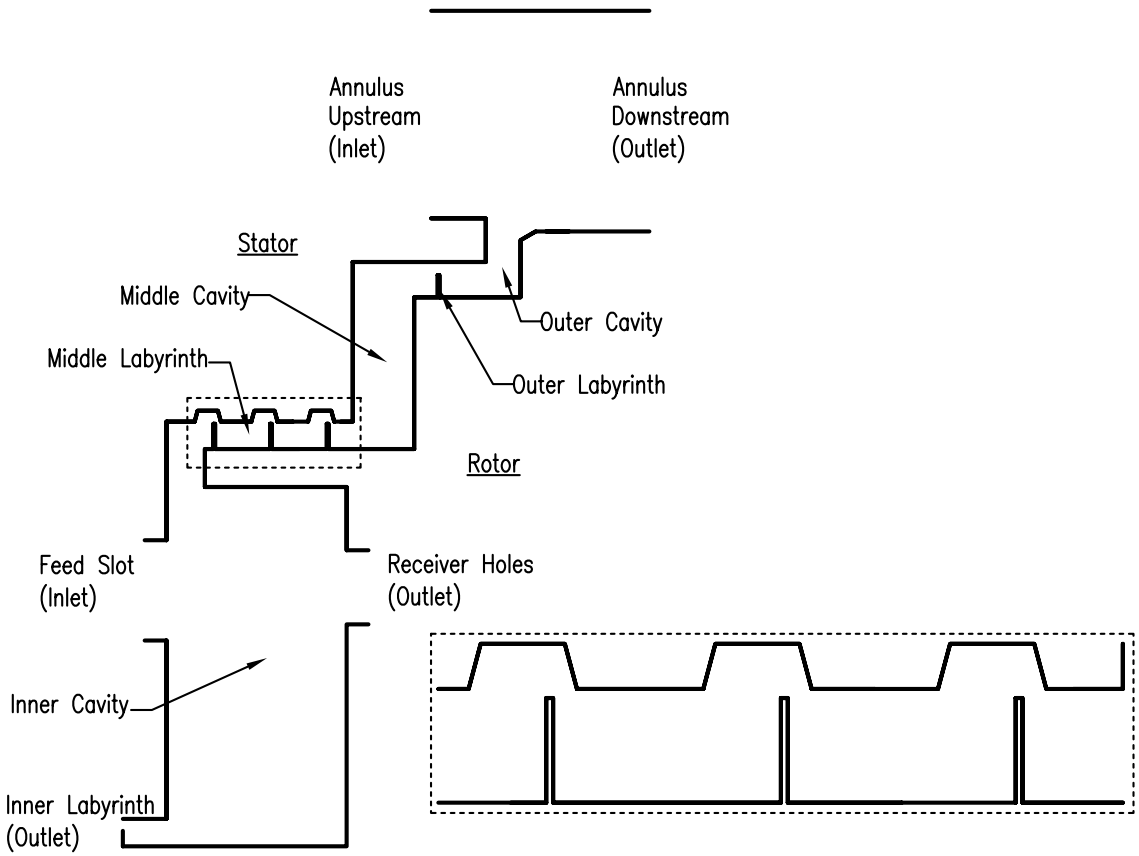

Fig. 2. Meridional view of the computational domain of the gas turbine wheelspace.

depth understanding of hot gas ingress is necessary to guide the turbine design. For gas turbines operating with high pressure and high temperature, hot gas ingress is an especially important concern. To minimize hot gas ingress for high pressure turbines, especially for large industrial ones, labyrinth seals are often used in the wheelspace. The present work investigates the wheelspace of a very large industrial gas turbine under high pressure and at high temperature. Figure 2 shows a section of the wheelspace and mainstream annulus under present research. It contains several labyrinth seals that divide the wheelspace into several cavities.

Though the overall geometry of labyrinth seal (refer to Fig. 1) appears to be not complicated, it is difficult to generate a computational grid of good quality. The difficulties lie in the nature of the labyrinth seal flow as well as the geometry involved. When fluid passes through the narrow slot formed between the tooth and the stator housing, there is a large change in velocity and pressure, along with intense turbulence generation. To accurately predict the flow, the grid around the clearance is necessary to have very good quality. Otherwise, the convergence and accuracy of the solution will be jeopardized. But due to the small size of the clearance, typically 1/20 - 1/100 of the whole domain, it is not easy to obtain a good grid around these regions. An ideal grid should have a sufficient number of cells to handle the abrupt change in the flow variables, and should also satisfy the requirements for solving the viscous sub-layer flow along the wall. The other difficulty for grid generation involves the geometrical details which may exist in the rub-groove and labyrinth tooth region. These details include the exact shape of the rub-groove and the shape of the tooth tip which might make a difference for labyrinth seal performance. To simulate the effects of the worn tooth, for example, it is necessary to preserve the rounding of the labyrinth tooth. And the radius of the rounding is usually only 1/100 - 1/10000 times that of the whole domain. These details impose a major challenge to many

grid generators which tend to smooth them out or produce ill-shaped cells in these regions.

For labyrinth seal flow the quality of the grid is vital to the convergence and the accuracy of the solution. Though a grid can have cells of various shapes, some shapes are superior to others in terms of grid quality. Experience as well as theoretical work from many researchers shows Cartesian cells are the most favorable, as they excel in both the accuracy and the convergence. But a purely Cartesian grid cannot utilize body-fitted cells along the boundaries. So the grid generator developed in this study generates hybrid grids, with the majority of cells being Cartesian.

B. Previous Work

1. Labyrinth Seal Rub-Groove

The labyrinth seal has long been a subject of research. Researchers began to study the leakage of labyrinth seals early in the last century. Among the earlier researchers are Martin [1], Egli [2] and Kearton[3]. Later researchers studied many parameters of the labyrinth seal, such as the honeycomb land [4], scaling effects [5], friction and wear [6] shaft rotation[7] and tooth axial position[8].

Only very limited work has been devoted to the presence of a rub-groove. The early investigation of rub-grooves was conducted by researchers from industry. Stocker, et al [9] included a few cases with rub-grooves while testing labyrinth seals for aircraft engines. The groove was radially 0.25mm deep and axially 0.6 mm wide, with a narrowed width of 0.51 mm at the groove bottom. The tooth pre-rub clearances tested were 0.13 mm, 0.25 mm and 0.51 mm. Stocker, et al found that the presence of a rub-groove somewhat decreased the leakage, which is surprising and does not agree with what was found by later researchers. This anomaly, however, was apparently caused

by the closing-off of the abradable porous surface (i.e. the leakage path through the porous land material) that resulted from the rub-groove fabrication process. Further, Zimmerman, et al [10] investigated a few labyrinth seals, both straight-through and stepped, with rub-grooves. The rub-groove was rectangular, 0.75 mm wide in the axial direction and 0.2 mm deep in the radial direction. The tooth pre-rub clearances studied were 0.2 mm and 0.4 mm. It was found that seal leakage increased substantially due to the presence of rub-grooves, especially for the stepped seal. Researchers from academia also conducted a few investigations considering rub-grooves. Yu and Childs [11] investigated labyrinth seals experimentally. One case investigated had rectangular rub-grooves in the honeycomb stator housing. It was found that the mass flow is not affected very much by the shaft speed and upstream swirl. There was only a very slight leakage decrease observed with an increase of shaft speed, and very slight leakage increase with an increase of upstream swirl. More extensive research on rub-grooves was conducted by Rhode and his coworkers. To explore the leakage effects of rub-grooves, Rhode and Allen [12] built a very large scale ($\times$ 30) labyrinth seal test rig shown in Fig. 3.

The rub-grooves tested were rectangular, and the working fluid was water. Their size and shape were chosen to encompass those few cases studied by industrial researchers, specifically Stocker, et al [9] and Zimmerman, et al [10]. It was found that, at least for incompressible fluids, the shape of the groove bottom corner has only a slight effect on leakage. Further, it was found that the leakage resistance decreases sharply with increasing groove width. Using the same test rig, Rhode and Allen [13] also examined rub-groove effects for stepped labyrinth seals. It was found that the leakage resistance decreases due to the presence of a rub-groove, at least for the incompressible cases studied. For the large step height studied, the leakage resistance decrease was 85%, 55% and 70% for the small, medium and large rub-groove clear-

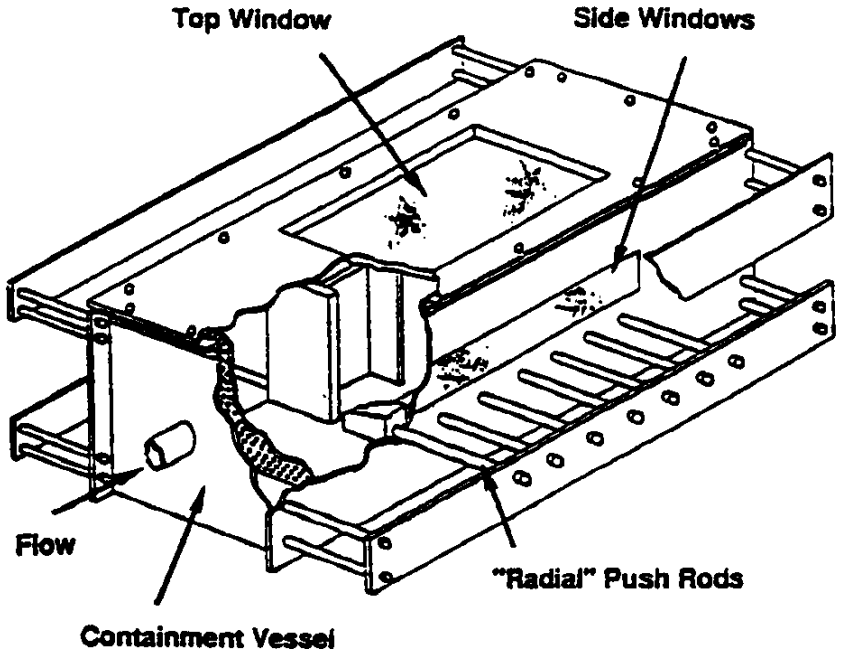

Fig. 3. The cut-away view of the large-scale labyrinth seal test rig.

ance respectively. The findings were later confirmed by Denecke, et al [14]. To further explore the effects of rub-groove size on leakage, Rhode and Adams [15] conducted a numerical investigation on straight-through labyrinth seals for compressible flow. The groove axial widths studied were 0.762 mm and 1.524 mm with radial depths of 0.102 mm and 0.203 mm. The cases studied had clearances of 0.102 mm and 0.203 mm, with step heights of 0.406 mm, 0.813 mm and 1.63 mm. It was found that the presence of the rub-groove of all sizes has appreciable effects on the leakage as well as on the global flow pattern. But the effects on leakage vary with the size of the rub-groove, as well as the radial clearance and the step height. For example, for the case of a wide and deep rub-groove, a small clearance and an intermediate step height, the leakage increases as high as 194% of the pre-rub value. To explore the effects of rub-groove width and depth, Rhode and Adams [16] undertook another numerical investigation on straight-through labyrinth seals for compressible flow. The groove axial widths studied were 0.762 mm, 1.524 mm and 2.286 mm with radial depths of 0.102 mm, 0.203 mm and 0.305 mm. The cases studied have clearances of 0.102 mm, 0.203 mm and 0.305 mm. It was found for the cases with large clearance and narrow rub-groove width, that the leakage remains almost constant with or without the presence of a rub-groove. For all the other cases, the presence of the rub-groove increases the leakage appreciably. The flow pattern variation is also observed for the cases with a rub-groove of different width and depth. For example, the case of a narrow rub-groove and a small clearance gives a flow pattern that are sharply different of others.

2. Labyrinth Seal Tooth Damage

When an abradable sealing surface is used, the seals are often referred to as abradable seals, and a considerable amount of research has been done on this. For example,

Chupp, et al [17] studied the application of abradable seals to certain types of gas turbines. The thermally sprayed coating he applied to a stage 1 gas turbine improved the engine performance as high as 0.8%; while a honeycomb seal applied to a stage 2 and 3 gas turbines improved the engine performance as high as 0.6%. It was concluded that abradable seals are very effective in improving turbine performance via reduced clearances. He gave a brief summary of the rub mechanism. Dowson, et al [18] studied the application of abradable seals to centrifugal compressors and steam turbines. He presented the efficiency gained with the use of abradable seals. When the inlet flow varied from 0.472 to 4.72 m^3/s (or from 1000 to 10000 CFM), Dowson found that, due to the use of abradable seals, the stage efficiency gained 0.3% - 2.4%, total efficiency 0.9% - 5.9%. As noted previously, rub-grooves form on the abradable surface when rubbing occurs.

Concerning the effect of rub-grooves, some research has been conducted over the recent years, especially the effect on leakage. A literature survey on this is available in Xu, et al's paper [19]. Regarding tooth bending damage, the effect on leakage has never been quantitatively reported in the literature. The particular type of tooth damage depends mostly on the design and materials used for the teeth, but also on the running condition of the labyrinth seal. For example, if made from soft materials such as aluminum, the teeth will likely be mushroomed or eroded at the tip in a gentle rub situation. Alternatively, in the event of an intense impact by the rotor, teeth made of any metal (including steel alloys) have been found with various degrees of bending damage. Of course, this bent tooth type of damage gives a major increase of clearance and thus a significant increase of leakage. If made from a highly flexible polymer, the teeth will generally only be temporarily flexed. Whalen, et al [20], [21], Ross, et al [22] and Ghasripoor, et al [23] all discussed these different situations from their industry experience. Many polymers for making the teeth have been developed over

the recent years due to their superiority over traditional materials such as aluminum. Polymer teeth will survive a rubbing by giving a deflecting and then regaining their original shape and clearance, due to the polymer's flexible nature. More discussion on polymer seals, especially their application to centrifugal compressors, can be found in the Whalen, et al papers [20], [21].

3. Gas Turbine Annulus Hot Gas Ingress

To avoid overheating while minimizing the efficiency penalty at the same time, extensive research has been conducted to the annulus gas ingress. Earlier researchers noticed the ingestion effects of a rotating disc, which draws flow from the mainstream annulus due to centrifugal disc pumping. For example, Bayley [24] conducted an experiment on flat disks in the absence of blades and vanes, later followed by Chew[25] and Khilnani[26].

For gas turbines under realistic operating conditions, however, the research suggests that the primary culprit of the ingestion is the circumferential pressure variation within the mainstream [27], [28], [29], [30], [31], [32], [33], [34], [35]. For example, Hamabe [29] conducted an experiment on a test rig with both the blades and vanes present. He found that the effect of disk pumping is relatively small when Re_z and Re_θ are of the same order. He found the mainstream ingress is dominated by the circumferential pressure variation, which affects the sealing effectiveness considerably. Based on their experimental and numerical work, Bohn, et al [34] concluded that the hot gas ingestion, due to the pressure asymmetry, can not be completely suppressed. Johnson [36] gave a discussion on the ingestion mechanisms.

Another issue that significantly affects both the ingress and the secondary coolant air flow is the configuration of the wheelspace. A wheelspace with an advanced geometry proves to be more effective in suppressing the gas ingress, or in cooling the

rim cavities. For example, Khilnani [26] found double-toothed rim seals are much more effective in suppressing the gas ingress, compared to that with simpler geometries. Teramachi, et al [37] also found that "fish mouth" type rim seals are superior in ingress prevention to single-fin types, and they are less affected by the fin overlap. Okita, et al [38] found, by judiciously placing a divider plate into the wheelspace, that rim cavities can be more effectively cooled. Rim seals usually have only one or two teeth. Long labyrinth rim seals with three or more teeth, normally installed inside the wheelspace of only extremely large gas turbines, have not received much attention until recently. With the escalating efficiency requirement, more attention is directed to wheelspace secondary air seals. For example, Mirzamoghadam, et al [39] investigated the flow and heat transfer inside an industrial rim cavity which has a labyrinth seal with nine teeth on both the rotor and the stator. Also, Choi [40] investigated an industrial gas turbine with a three-tooth labyrinth seal and found that the seal clearance and tooth pitch significantly affect the gas ingress and secondary throughflow cooling.

Most of the researchers who numerically studied gas ingress assumed the flow to be steady state. They found reasonably good agreement between numerical prediction and measurements [41], [42] and [43]. Recently, numerical researchers began to simulate the flow for transient conditions. Hills [44], Laumert [45] and Bohn [46] found or suggested that the transient effects are important based on their operating conditions. They also obtained better agreement between their numerical predictions and measurements. Further, Cao [47] and Jakoby [48] found that these transient effects are sometimes due to a large scale rotating structure in the stator-rotor (front cavity). It appears that under certain conditions this structure is very sensitive to the cooling air mass flow [48]. On the other hand, unsteadiness does not alway play an important role. For example, Benim [49] found it was not important for his case.

Apart from the gas turbine hot gas ingress, the labyrinth seal is also under active research. Labyrinth seals are also widely used, in many other locations within turbomachinery. The effect of a rub-groove for these seal applications has also received researchers' attention. For example, Zimmerman, et al [10], Rhode, et al [15] and Denecke, et al [14] all found the presence of rub-groove increases the leakage substantially, especially for stepped seals. Rhode and Allen [12] found that seal leakage resistance decreases strongly with increasing groove width. Rhode and Adams [15] also found that the effect of a rub-groove on the leakage varies with its size.

A further investigation from Rhode and Allen [16] showed that the leakage of labyrinth seals with large clearance is almost not affected by the presence of a rub-groove with a narrow width. For other cases, the rub-groove increased the leakage appreciably. Further, Xu, et al [19] conducted an investigation focusing on the rub-groove wall angle and tooth position. They found the considerable influence of downstream wall angle of a rub-groove on the leakage, as well as on the flow pattern. It was found that the degree of influence varies with tooth position and radial clearance. All the aforementioned work on labyrinth seals is conducted in a general context. Most of the attention is focused on the effect of leakage, with a little attention given to the effect of flow pattern. Little of the above research, however, is focused on the effect of the labyrinth seal on the heat transfer and temperature fields.

4. Grid Generator Development

The Cartesian grid is probably the most primitive grid ever used in the community of numerical computation. Compared to more sophisticated grids, Cartesian grids are easy to generate. They also offer more accurate solutions and better convergence rates due to their inherent orthogonality. All of these merits make Cartesian grids the first choice for earlier researchers. But on the other hand, Cartesian grids are

geometrically very "stiff", i.e. not easily adapted to complicated boundaries. With the development of numerical methods, the computational domain becomes more and more complex, and Cartesian grids are used less frequently. As an emerging trend, unstructured grids almost dominate the computational community. But due to their simplicity, accuracy and benefit to convergence, researchers have revived their interest in Cartesian grids, and equipped them with unstructured technology (called "hybrid" grids) [50], [51], [52], [53], [54], [55], [56], [57].

The overall methodology employed by many researchers to generate such hybrid grids can be generally described as follows. It firstly creates an initial or background grid which covers the entire geometrical domain, then removes the cells outside of the domain. Now a very raw Cartesian grid is obtained which has the rough shape of the domain. The last step is for the computational domain boundaries to approach the real boundaries by refining the cells along the boundaries.

To fit the physical boundaries, several near-boundary strategies are employed with unstructured Cartesian grids: cell subdivision, cell adjustment and cell cutting. The cell subdivision strategy recursively subdivides each cell along the boundaries into four smaller Cartesian cells, until the resultant boundaries of the Cartesian grid geometrically approach the real boundaries well enough. This strategy offers simplicity to both the grid generator and the flow solver. The grid generated with this approach, however, is unable to compute quantities such as the heat transfer coefficient that require two or more cells along the wall to be body-fitted and well layered. Quirk [50] and Yiu [55] used this cell subdivision approach to generate the Cartesian grid. Another strategy to approach boundaries is through cell adjustment, proposed by Schneiders [51] [52] [53]. This approach adjusts the vertices of one or two layers of cells along boundaries, to make boundary cells fit the physical boundaries. After vertex adjustment, boundary cells turn into quadrilaterals, and the final grid in a whole

domain is no longer purely Cartesian. The third strategy to approach boundaries is cell-cutting.

Wang [56] and Zhang [58] employed cell cutting to approach the boundary. This approach cuts boundary cells according to the real boundaries, leaving one portion of the boundary cells cut out. As a result, non-Cartesian cells are created along the boundaries. With both the strategies of cells adjustment and cell cutting, the final grid ends up being hybrid, with boundary cells of shapes other than Cartesian. However, these two approaches advantageously generate body-fitted cells along boundaries, without generating hanging vertices which occur with the cell subdivision approach. And they also make it possible to generate layers of body-fitted quadrilateral cells along the wall to solve flow variables which require that. Among the three strategies, cell cutting possesses the most flexibility due to the greater freedom in choosing boundary cells, the other two being restricted to Cartesian and quadrilateral cells respectively. The new grid generator code developed herein, OpenCFD, adopts the cell cutting strategy to approach the boundaries. But it applies a further subdivision to the cut-out boundary cells to decompose all cells into either quadrilateral or triangular ones. This is enforced to enhance the compatibility with other flow solvers. Most of them, for the two-dimensional grid concerned, can handle only quadrilateral and triangular cells.

Apart from approaching the physical boundaries, another issue each grid generator needs to handle is grid refinement. Quirk [50], Yiu [55], Wang [56] and Zhang [58] refined the grid by simply subdividing all cells to be divided into four equal-sized small Cartesian cells. And the division can be applied to cells recursively if necessary. This however creates hanging vertices which are unacceptable, requiring additional work for many flow solvers on the neighboring cells which are not subdivided. To avoid hanging vertices, Schneiders [53] used a more sophisticated approach to subdi-

vide cells. Care is exercised to subdivide the outer cells of the region to be refined, so that no hanging vertices occur. After refinement, the cells inner to the refinement region are still Cartesian, while the outer cells are quadrilateral. OpenCFD uses a similar concept to refine the local grid density, but it allows the outer cells to be triangular for the sake of simplicity. Figure 59 in Chapter VII shows what a grid will look like after local refinement.

As far as data structure is concerned, almost all researchers used quadtree to store the two-dimensional Cartesian grids [50], [51], [52], [53], [54], [55], [56]. Quadtree naturally supports subdivision of one cell into four small cells. But quadtree is inept to handle other cell subdivision. For example, to support the refining strategy proposed by Schneiders [53], which is a variant of the 1-to-4 subdivision, the original quadtree has to be revised to achieve this ability, because 1-to-4 subdivision refines cells in both horizontal and vertical directions at the same time, disallowing refinement in a single direction. To avoid this restriction, OpenCFD uses interrelated vectors to store the grid and thus gain unlimited flexibility in the grid layout and cell subdivision. More discussion on quadtree can be found in references [52] and [56].

For modern grid generators, it is very important to accept the geometry to be meshed in some standard formats which are supported by mainstream CAD software. This spares the user from learning how to specify the geometry for each grid generator. The user has the freedom to draw the geometry with his favorite CAD packages, then to import it into the grid generator. It is then up to the developer to figure out a way to read the geometry from the CAD file. Beall [59] gives an overview of how to access the CAD geometry file. For simplicity, OpenCFD uses DXF as the CAD format, extracting the geometry by parsing the geometry file. The DXF format stores the two-dimensional geometry in plain text. It is developed and maintained by Autodesk, but is fully open to the public. The specification of DXF is available at Autodesk's

website.

For modern commercial CFD software, it is vital to have scripting capability. That is, the CFD program itself serves as a platform, and the user is allowed to communicate with it through a certain scripting language. For example, Fluent and Gambit use Scheme, a variant of LISP; STAR-CD and CFX use Tcl; Tetgen uses Lua. More information on Tetgen and Lua is available at http://tetgen.berlios.de and http://www.lua.org respectively. Other scripting languages are also available. OpenCFD uses Python (ref http://www.python.org) as its scripting language due to: (1) its being inherently object-oriented, and (2) its syntax being more like a modern language such as C/C++ and hence easy to use.

C. Research Need

1. Labyrinth Seal Rub-Groove Wall Angle

Many gas turbine engines contain a large number of abradable labyrinth seals. Rub-grooves are generally formed in gas turbine labyrinth seals of the abradable type during various transients. The engine performance is influenced by the effect of rub grooves on seal leakage. The rub-groove shape, especially the slope angle of the groove downstream wall, varies depending largely on the rotordynamics and the thermal expansion rates of the rotor and the stator. Researchers and manufacturers have only very limited knowledge and understanding of worn and damaged labyrinth seals. Only a few investigations concerning rub groove effects on labyrinth leakage have been reported, and these essentially considered only rectangular-shaped grooves of various sizes. Nearly all labyrinth design models, however, do not attempt to account for the leakage effects of rub grooves. Chupp, et al [60] pointed out that a modest leakage change in labyrinth seal flow can significantly impact engine performance.

The inaccuracy of most simple design leakage models, due to the lack of knowledge of rub-groove wall angles for example, can lead to performance deficiency in labyrinth seals. Consequently, the engine efficiency decreases and the cost increases.

2. Labyrinth Seal Tooth Damage

Unavoidable rotordynamic impacting on labyrinth seal teeth sometimes occurs when centrifugal compressors, for example, undergo transients. Consequently, the labyrinth seal teeth are damaged or disfigured in various ways when the surface opposite to the teeth is non-abradable. Previous researchers and refurbishment personnel both suggest that the labyrinth seal tooth damage can lead to considerable leakage increase. The leakage increase, in turn, affects turbomachinery efficiency. In some cases, this efficiency degradation can be considerably large. But prior to this investigation, no specific quantitative information concerning the effect of labyrinth seal tooth damage, specifically tooth bending and tooth "mushrooming", on seal leakage was available.

3. Gas Turbine Annulus Hot Gas Ingress

Large industrial gas turbines usually use labyrinth seals with multiple teeth in the wheelspace to control the secondary flow, which is used to suppress the annulus hot gas ingress heating. Previous work has found the wheelspace hot gas ingress is strongly influenced by the configuration of rim and wheelspace labyrinth seals. It has also been found that the rub-groove, for example its wall angle and tooth position, generally significantly affects the labyrinth seal leakage and flow pattern, which strongly influence the temperature in the wheelspace. But how the rub-groove geometry, in terms of wall angle and tooth position, would affect the flow and temperature field inside the gas turbine wheelspace has not been reported.

4. Grid Generator Development

With the advancement of grid generation algorithms and computer technology, commercial grid generators become more and more powerful. But almost all of them are aimed toward general purpose applications and are not well suited for the grid generation required for a labyrinth seal. Though it is possible to use an existing code to generate the grid, it usually takes quite a long time and significant manual intervention to generate a desirable grid due to the aforementioned difficulties and special requirements for the labyrinth seal grid. Considering the large quantity of cases involved in the present research, this will consume a large mount of time. For the sake of efficiency, it was desirable to develop a grid generator which can produce the grid for the labyrinth seal quickly and efficiently, and at the same time have good quality.

D. Research Objectives

1. Labyrinth Seal Rub-Groove

The present objective regarding rub-grooves is to obtain an enhanced understanding of the effects of rub groove shape, i.e. rub-groove downstream wall slope for a fixed groove size, on compressible flow leakage through stepped labyrinths.

2. Labyrinth Seal Tooth Damage

The objective regarding labyrinth seal tooth damage is to quantitatively investigate the effect of permanently damaged teeth on the leakage of labyrinth seals. Two forms of damage will be specifically addressed: (1)tooth bending damage, and (2) tooth tip mushrooming damage. The present work studies the leakage effect of each of the two individual damage, as well as their combined form.

3. Gas Turbine Annulus Hot Gas Ingress

This work aims to numerically investigate the effect of rub-groove wall angle and axial position on the hot-gas ingress in the gas turbine. An enhanced understanding of the wheelspace flow patterns and temperature field, under the influence of rub-grooves, is also sought.

4. Grid Generator Development

Another objective was the development of a grid generator with special capabilities for generating grids quickly and efficiently for labyrinth seal. The grid generated should be able to preserve any small geometrical details involved in the computational domain. To help the discussion in the subsequent chapters, the grid generator is referred to as OpenCFD.

CHAPTER II

NUMERICAL MODEL

This chapter gives a brief review of the numerical model which applies to all the numerical simulations in this study. That is, what is covered in this chapter, unless specifically stated otherwise, generally applies to the labyrinth seal study of rub-groove wall angle, tooth bending, tooth mushrooming and turbine ingress heating. The portions which are specific to each of the sub-topics will be discussed in the pertaining chapters.

The fluid flow is simulated by solving the Reynolds-averaged Navier-Stokes (RANS) equations. STAR-CD, a commercial CFD code based on finite-volume methodology, is used as the flow solver. For all the cases studied herein, the flow is steady, compressible and fully turbulent.

A. Governing Equations

The well-known Navier-Stokes equations can be used to describe any general fluid flow. The mass and momentum conservation equations can be written, in Cartesian tensor notation [61], as:

$$\frac{\partial \rho}{\partial t} + \frac{\partial}{\partial x_j}(\rho u_j) = 0 \tag{2.1}$$

$$\frac{\partial}{\partial t}(\rho u_i) + \frac{\partial}{\partial x_j}(\rho u_j u_i - \tau_{ij}) = -\frac{\partial p}{\partial x_i} \tag{2.2}$$

In Eq. 2.2, p is the piezometric pressure,

$$p = p_s - \rho_0 g_j x_j \tag{2.3}$$

where x_j represents coordinates of the location where ρ_0 is defined.

τ_{ij} in Eq. 2.2 is the stress tensor with components,

$$\tau_{ij} = 2\mu s_{ij} - \frac{2}{3}\mu\frac{\partial u_k}{\partial x_k}\delta_{ij} - \bar{\rho}\overline{u_i' u_j'} \tag{2.4}$$

The last term $\bar{\rho}\overline{u_i' u_j'}$ on the right-hand side of Eq. 2.4 is the shear stress contribution due to turbulence fluctuation, which does not exist for laminar flow. The fluctuation term cannot be solved directly and has to be modeled.

The energy equation can be written as

$$\frac{\partial}{\partial t}(\rho h) + \frac{\partial}{\partial x_j}(\rho h u_j - F_{h,j}) = \frac{\partial p}{\partial t} + u_j\frac{\partial p}{\partial x_j} + \tau_{ij}\frac{\partial u_i}{\partial x_j} \tag{2.5}$$

In this equation, h is the static enthalpy as defined by:

$$h \equiv \bar{c}_p T - c_p^0 T_0 + \sum Y_m H_m \tag{2.6}$$

where $\overline{c_p}$ is the mean constant-pressure specific heat at temperature T, c_p^0 is the reference specific heat at temperature T_0, while Y_m and H_m are the mass fraction and heat of formation of mixture constituent m, respectively.

In Eq. 2.5, $F_{h,j}$ is the diffusional flux, whose time-averaged expression is

$$F_{h,j} \equiv \lambda\frac{\partial T}{\partial x_j} - \bar{\rho}\overline{u_j' h'} + \sum_m h_m \rho D_m \frac{\partial Y_m}{\partial x_j} \tag{2.7}$$

Here the term $\bar{\rho}\overline{u_j' h'}$ represents the static enthalpy transportation due to turbulent diffusional flux [62]. It disappears when the flow is laminar. Like $\bar{\rho}\overline{u_i' u_j'}$, $\bar{\rho}\overline{u_j' h'}$ can not be solved directly, and has to be modeled.

B. Turbulence Modeling

High-Reynolds $k-\epsilon$ model is used. It is applied outside of the log-law region. The fluctuation terms in Eqs. 2.4 and 2.7 are modeled as:

$$-\bar{\rho}\overline{u_i'u_j'} = 2\mu_t s_{ij} - \frac{2}{3}\Big(\mu_t\frac{\partial u_k}{\partial x_k} + \rho k\Big)\delta_{ij} \tag{2.8}$$

$$\bar{\rho}\overline{u_j'h'} = -\frac{\mu_t}{\sigma_{h,t}}\frac{\partial h}{\partial x_j} \tag{2.9}$$

where

$$k \equiv \frac{\overline{u_i'u_i'}}{2} \tag{2.10}$$

is the turbulence kinetic energy, and $\sigma_{h,t}$ the turbulent Prandtl number.

Here s_{ij} is the mean strain, given as

$$s_{ij} = \frac{1}{2}\Big(\frac{\partial u_i}{\partial x_j} + \frac{\partial u_j}{\partial x_i}\Big) \tag{2.11}$$

And μ_t is the turbulent viscosity, which relates k and ϵ as

$$\mu_t = C_\mu\rho\frac{k^2}{\epsilon} \tag{2.12}$$

where C_μ is an empirical coefficient.

The basic wall function, proposed by Launder and Spalding[63], was used to account for the distribution of velocity and turbulence adjacent to the walls. It links the wall shear stress to the velocity as

$$u^+ = \begin{cases} y^+ & y^+ \le y_m^+ \\ \dfrac{1}{\kappa}ln(Ey^+) & y^+ > y_m^+ \end{cases} \tag{2.13}$$

where y_m^+ is determined by

$$y_m^+ - \frac{1}{\kappa} ln(E y_m^+) = 0 \tag{2.14}$$

It has been found by Rhode and Adams [15] that the above modeling agrees well with measurements of labyrinth seals with rub-grooves. In predicting wheelspace hot gas ingestion, Jakoby [48] found that the basic wall function gives better agreement with experiment than the enhanced wall function [48] in the wheelspace hot gas ingestion for higher secondary flows. For lower secondary flows, the two wall functions gave about the same results.

C. Grid Generation

Due to the nature of axisymmetry, the grids for studying the rub-groove wall angle, tooth bending and tooth mushrooming are two dimensional, while the grids for studying the wheelspace hot gas ingress are three dimensional. All the two dimensional grids in the present study were generated by the in-house grid generator OpenCFD. The three dimensional grids were created by first generating a two dimensional grid for the $r - z$ plan with OpenCFD, then revolving the grid into a three dimensional one in STAR-CD. The griding for the feed slot, which spans circumferentially only a small fraction of the computational domain, is also done within STAR-CD. To obtain better resolution for the middle and outer cavities in the wheelspace, embedded refinement is also employed in the circumferential direction. This is also done with STAR-CD.

Created by OpenCFD, all the grids bear the hallmarks of OpenCFD. The grids used are all unstructured, with a dominance of hexahedra (3D) or Cartesian (2D) cells. Only a small number of prisms (3D) or triangles (2D) are used as fillers. In

order to get accurate resolution around the labyrinth seals, which is very important in determining the leakage, the grid around those regions is refined. To resolve the viscous flow near the wall, two or three layers of body-fitted hexahedrons are used along all walls. The thickness of the layers varies along the wall in order to ensure a proper range of y^+. For all cases simulated in the present study, y^+ is kept from 12 to 160. For most of the regions, especially those around the labyrinth tooth tips, y^+ is controlled between 30 and 120.

For a more complete knowledge of the grids, one is advised to refer to the features of OpenCFD grid in Chapter VII, and also the individual grids in Chapters III, IV, V and VI.

D. Comparison with Measurements

1. Labyrinth Seal Leakage

To verify the accuracy of the CFD prediction, comparison with measurements was undertaken. The measurements were conducted using the same test rig as that used by Rhode, et al [12], [13] as shown in Fig. 3. The test rig housing was made of welded Hastelloy-X. The housing measures 2.438m $\times$ 0.914m $\times$ 0.914m. On three sides of the test rig, as well as on the lid, large plexiglass windows were installed to allow flow visualization. The labyrinth seal was constructed through the fabricated acrylic attachments which were positioned by the push rods shown in Fig. 3. This enables almost any geometry of labyrinth seal to be assembled through adjustment of the attachments. The flow rate and pressure drop of labyrinth seals were measured in the test rig. The flow rate was measured with a 10.16 cm (4 in) flange tap orifice meter located downstream of the test rig. The pressure drop was measured with a Validyne model DP-15 variable reluctance pressure transducer. The measurements were then

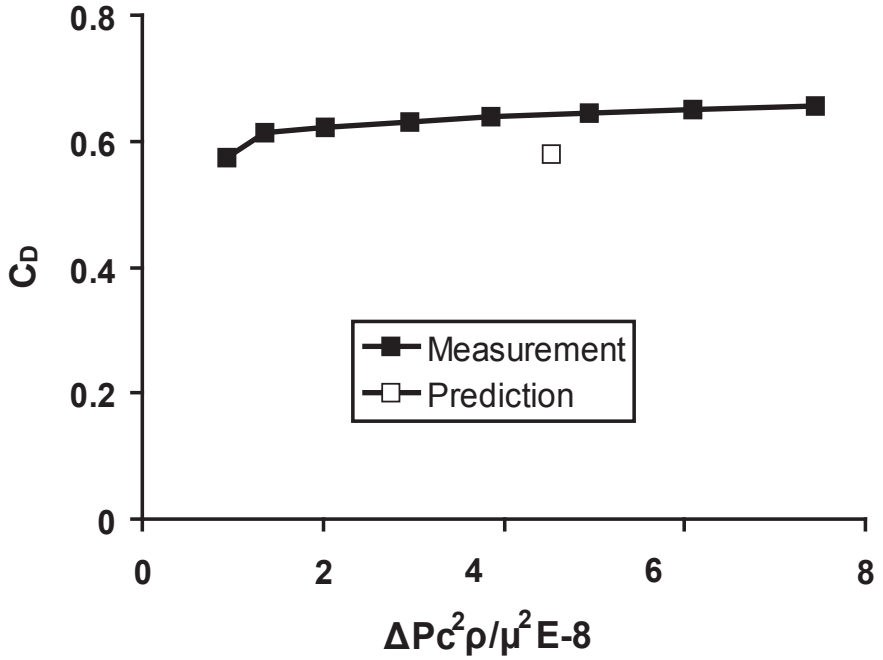

Fig. 4. Comparison between measurement and numerical prediction for labyrinth seal leakage.

compared with the numerical prediction obtained from STAR-CD, as shown in Fig. 4. The discharge coefficient was used here; it is associated with the leakage rate through Equations 2.15 and 2.16.

$$C_D = \frac{\dot{m}_{real}}{\dot{m}_{ideal}} \tag{2.15}$$

$$\dot{m}_{ideal} = \frac{A p_{t,u}}{\sqrt{R T_{t,u}}} \sqrt{\frac{1 - \pi^{-2}}{n + ln\pi}} \tag{2.16}$$

As one can see from Fig. 4, the numerical prediction agrees with the measurement within about 8.0%.

2. Gas Turbine Gas Ingress

For validation purposes, numerical predictions based on steady flow are also compared with experiment. The experiment conducted by Green [64] measured the concentration of a tracking gas, an alternative to estimate the mainstream hot gas ingress, on a stator-rotor test rig. The diameter of both the stator and the rotor is 400 mm, the seal gap ratio $G_c = c/R = 0.01$. The height of the mainstream annular channel is 30 mm. Air at room temperature is pulled into the annulus channel from the stator side. For test cases chosen to be compared in the present study, the trailing edge of the nozzle guide vanes (NGVs) coincides with the stator seal edge. The non-dimensional inlet pressure used is 2.5, defined as $P = 2\Delta p/\rho U_e^2$, where Δp is the peak-to-valley pressure difference, while ρ and U_e are the density and velocity of the air entering the annular channel respectively. The mainstream Reynolds number Re_z is defined as $Re_z = U_e r_o/\nu_e$, where r_o is the radius of the turbine disc and ν_e is the viscosity. The value of Re_z used in both the experiment and CFD is 5.1×10^5. The Rotation number R_o used is 1.57, defined as $R_o = V_\theta/U_e$, where V_θ is the circumferential velocity of the air measured at the NGV trailing edge. By adjusting the purge-coolant mass flow, i.e. the purge-coolant velocity, various U_m/U_e values were considered. Green measured scalar concentration for a series of U_m/U_e.

The comparison between the measurement and numerical prediction is shown in Fig. 5. The experimental data here are taken from Fig. 59-iii on page 141 from Green's PhD Thesis [64]. As one can see, the CFD prediction gives fairly good agreement with the experimental data, with a maximum discrepancy less than 10%. For the U_m/U_e considered here, the CFD prediction over-predicts the scalar concentration.

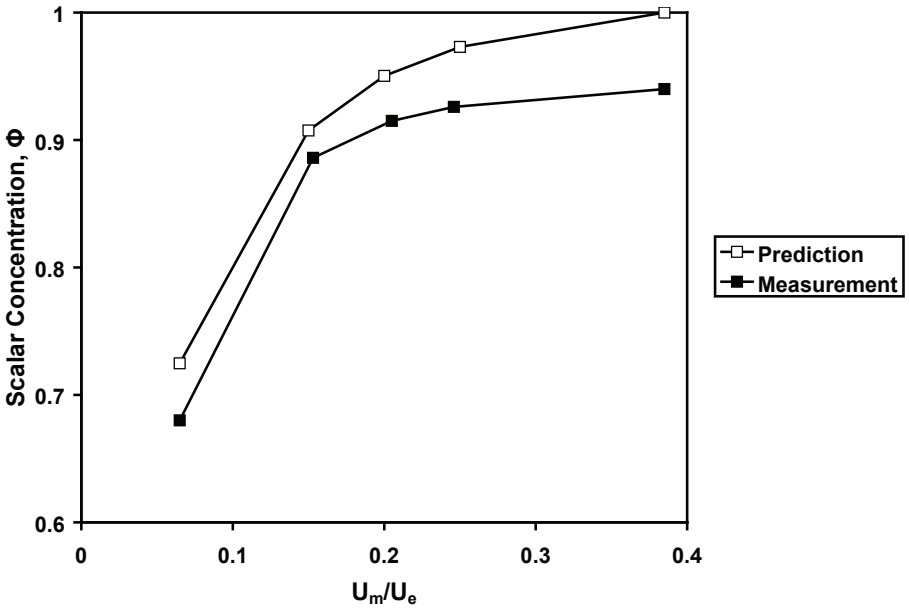

Fig. 5. Comparison between measurement and numerical prediction for the scalar concentration in the stator-rotor wheelspace.

CHAPTER III

EFFECT OF RUB-GROOVE DOWNSTREAM WALL ANGLE ON THE LEAKAGE OF LABYRINTH SEALS *

A. Problem Definition and Boundary Conditions

Because there is a very large range of gas turbines in existence, i.e. from missile engines to large power production units, it is not surprising that the size and shape of labyrinth rub grooves also vary widely. Rhode and Adams [15], [16] had previously found , for a rectangular groove shape, that rub groove axial width and radial depth have a significant leakage effect. Further, it had been previously determined experimentally by Rhode and Allen [13] that, at least for the cases considered, there was little leakage difference between a rectangular and a completely rounded groove shape of a given axial width and radial depth. Because the rectangular and completely rounded shapes are the two limiting cases, further testing had been discontinued. In addition, it was learned that gas turbine maintenance shops have encountered a wide range of groove shapes, including non-rounded groove corners and well rounded groove corners. The large variability of shape apparently depends on the degree of axial and radial transient thermal growth of the labyrinth rotor relative to the stator surface, as well as rotordynamic and centrifugal effects. The axial length and radial depth of the rub groove considered herein were held fixed, and the groove wall angle was

---

* Part of the data reported in this chapter is reprinted with permission from "Effect of Rub-Groove Wall Angle on the Leakage of Abradable Stepped Labyrinth Seals" by Jinming Xu, Matthew S. Ambrosia and David L. Rhode, 2005, *Tribology Transactions* Volume 48, Number 4, Pages 443 - 449. Copyright 2005 by Society of Tribologists and Lubrication Engineers.
Part of the data reported in this chapter is also reprinted with permission from "Effect of Rub-Groove Shape on the Leakage of Abradable Stepped Labyrinth Seals", AIAA-2004-3718, by Jinming Xu, Matthew S. Ambrosia and David L. Rhode, presented at 40th AIAA/ASME/SAE/ASEE Joint Propulsion Conference and Exhibit, Fort Lauderdale, Florida, July 11-14, 2004. Copyright 2004 by American Institute of Aeronautics and Astronautics.

varied for groove geometries that related to that considered in various studies by gas turbine manufacturers, i.e. Stocker, et al [9] and Zimmerman, et al [10]. Figure 1 in Chapter I shows the geometry and the definition of the dimensions. Specifically, the rub groove downstream wall slope angle α was varied from 0^o to 78^o; the axial width f = 3.556 mm and the radial depth e = 0.762 mm. Further, the labyrinth tooth pitch L_p = 7.62 mm; the tooth tip width W_t = 0.762 mm; the tooth height L_t = 5.207 mm; and the step height s = 2.54 mm. The three values of pre-rub radial clearance are c_{pr} = 0.381, 0.127 and - 0.127 mm, where a negative value indicates that the tooth tip lies within the rub groove. The after-rub radial clearance c_{ar} depends on the downstream wall angle α, tooth axial position x/f and the pre-rub clearance c_{pr}. The clearance specified was independent of the shaft radius. The operating conditions were fixed at $P_{t,u} = 1.379\times10^6$ Pa; $P_{s,d} = 1.149\times10^6$ Pa; $T_{t,u}$ = 394 K; ω = 1,047.2 rad/s (10,000 rpm); R_{sh} = 254 mm; and $\mu = 1.85\times10^5$ kg/(m-sec). At the upstream inlet, pressure boundary condition was used, and the operating pressure and temperature were prescribed. The direction and magnitude of the inlet velocity were not specified, and thus determined by the flow solution. The inlet entering turbulence is specified with an intensity of 0.1 and a length scale of 1 mm. At the downstream outlet, pressure boundary condition was also used. The downstream pressure was specified as the mean pressure across the outlet. On the two meridional surfaces, cyclic (also termed periodic) boundary conditions were used to account for the circumferential flow repetition.

In the subsequent discussion, clearances will be nondimensionalized by the radius to the inlet stator surface. After nondimensionalization, the three pre-rub radial clearances are c^*_{pr}=1.45×10^{-3}, 4.83×10^{-4} and -4.83×10^{-4}.

B. Grid and Grid Independence Test

Figures 6 and 7 show the grid around the tooth tip for two different rub-groove arrangements. The grid, generated by OpenCFD, is dominated by Cartesian cells. To resolve the flow around the tooth tip, which is vital to predicting an accurate value of leakage, embedded refinement is used. To eliminate the hanging vertices, triangular cells are used at the interface between the embedded region and the outer region. The extrusion layer along the wall has five sublayers. This is to ensure that every configuration of labyrinth seal has a sufficient number of cells between the labyrinth tooth tip and the opposite wall. As one can see in Fig. 6, there are about fourteen cells in the slot formed by the tooth tip and the opposite wall. This case has a dimensionless pre-rub clearance of c^*_{pr}=-4.83×10^{-4}, with x/f=0.75 and α=45^o. The after-rub clearance has the minimum value for the case with c^*_{pr}=4.83×10^{-4}, x/f=1.0, α=0^o (ref. Fig. 7). To get an adequate number of cells in the slot, the sublayer in the extrusion layer grows inwardly thinner and thinner, while the thickness of the outer sublayer facing the wall is fixed for all the cases.

Grid independence was verified and the result is shown in Table I. The case tested is similar in geometry to all the cases studied, and has a pre-rub clearance c^*_{pr} = - 4.83×10^{-4} and axial position x/f = 0.5. Table I shows the relative leakage difference among the grids. Table I also shows that, the solution of different grids is very close to each other, with the leakage difference less than 1%. The intermediate grid was used for all production computer runs in this study, since it has a fairly small number of cells, and differs only by 0.58% from the next finer grid in the leakage.

To ensure the proper velocity profile near the wall from the wall function, y^+ was carefully controlled through the thickness of an extrusion layer along the walls. As one can see, y^+ lies between 11 - 110 for all the grids.

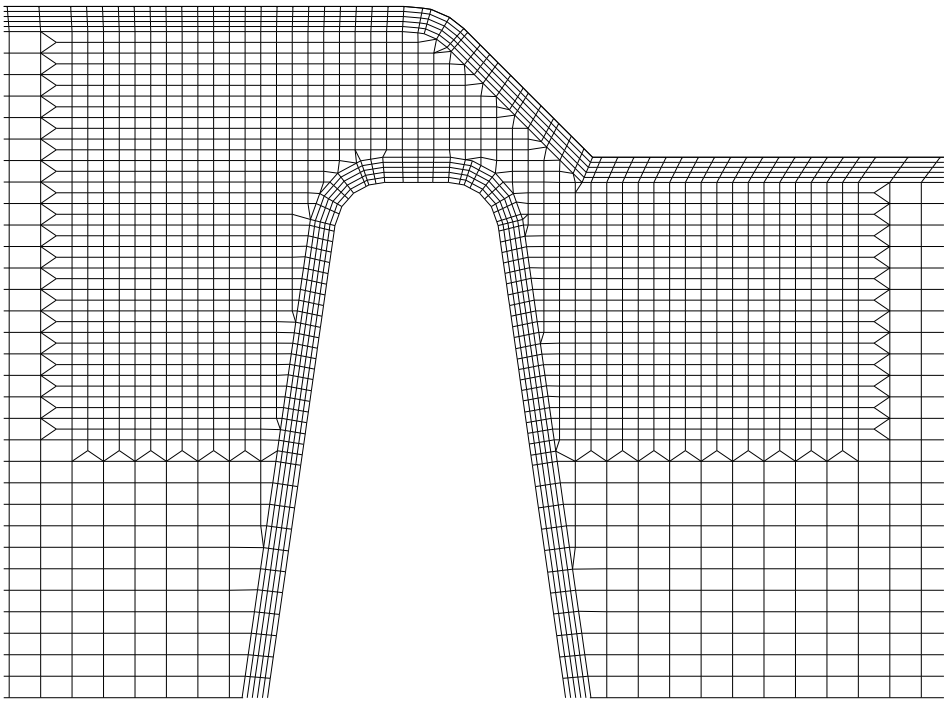

Fig. 6. Grid around the labyrinth tooth (c^*_{pr}=-4.83×10^{-4}, x/f=0.75, α=45^o).

Table I. Grid independence test for the study of rub-groove downstream wall angle of the labyrinth seal.

No. of Cells Used			y^+ along Wall	Seal Leakage (kg/s)	$\frac{\dot{m}-\dot{m}_f}{\dot{m}_f}$
Tooth	Streamwise	Transverse			
9	175	42	11 -102	0.806	-0.97%
10	218	52	11 - 103	0.815	-0.58%
11	260	66	11 - 106	0.819	-

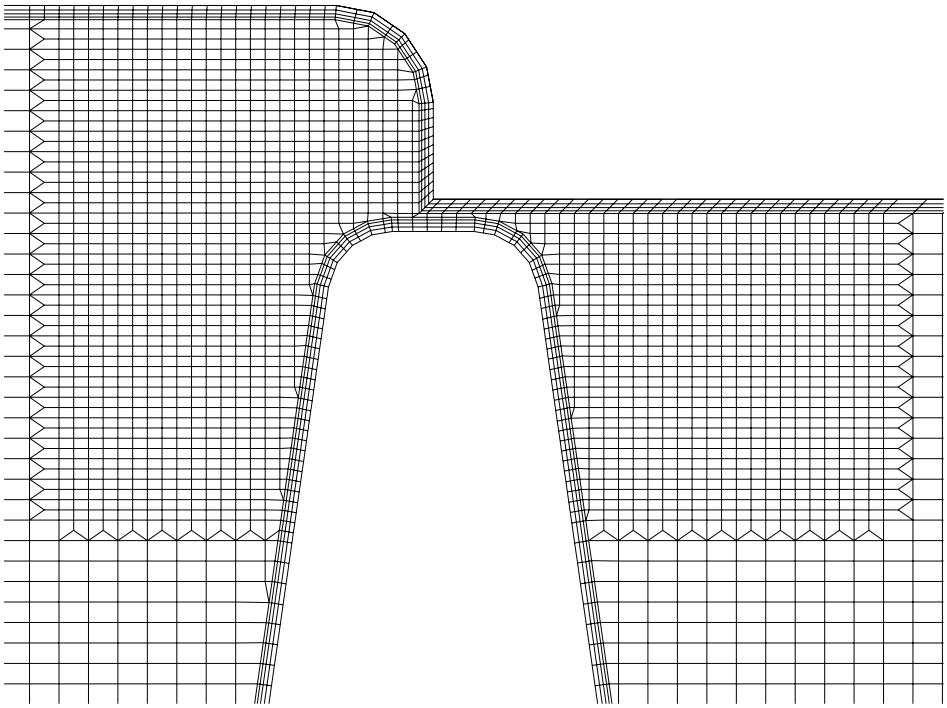

Fig. 7. Grid around the labyrinth tooth (c^*_{pr}=4.83×10^{-4}, x/f=1.0, α=0^o).

C. Results

1. Pre-Rub Clearance $c^*_{pr} = 1.45\times10^{-3}$

Figure 8 shows, for the given groove axial width, radial depth, and pre-rub clearance $c^*_{pr} = 1.45\times10^{-3}$, that various non-rectangular shapes can also have substantial leakage effects. The open symbols show the leakage Reynolds number, defined as $2\dot{m}/(\pi D\mu)$, for the three tooth axial positions, whereas the solid symbols show the after-rub clearance c^*_{ar}. Observe in Fig. 1 in Chapter I how the groove downstream wall angle α affects the after-rub clearance, especially for α greater than 60^o. Comparison of the trends of the predicted leakage Reynolds number and the after-rub clearance in Fig. 8 shows the very large, but not exclusive, effect of the after-rub clearance on leakage. Observe that each leakage curve is not quite parallel to that of the corresponding after-rub clearance, especially for tooth axial position x/f = 0.5. For example, at the axial position x/f = 0.5 the variation of leakage is much more gradual than that of the after-rub clearance for $\alpha > 60^o$, although for $\alpha < 60\ ^o$ they are almost the same. Also shown in Fig. 8 is that at x/f = 0.5 and $\alpha = 60^o$, an abrupt change of after-rub clearance occurs, whereas at x/f = 0.75 the change of after-rub clearance is much more gradual. Specifically, the variation of x/f from 0.5 to 1.0 gives an after-rub clearance decrease of about 65% for $\alpha = 0^o$ and of about 50% for $\alpha = 78^o$. Also notice that, at x/f = 1.0, the tooth tip lies downstream of the groove so that the after-rub clearance equals the pre-rub clearance

The non-parallel nature found for the leakage and after-rub clearance curves suggests that there are additional factors affecting leakage. To gain more insight, vector plots are shown in Figs. 9, 10 and 11 with the pre-rub clearance $c^*_{pr} = 1.45\times10^{-3}$ and x/f = 0.5 for $\alpha = 0^o$, 60^o and 78^o, respectively. For $\alpha = 0^o$, the through-flow jet exits the rub-groove at a certain flow angle, measured from the shaft axis direction,

as shown in Fig. 9. This flow pattern in Fig. 9 is referred to herein as the "sloping" (S) flow pattern. With an increase of α, the groove exit jet angle decreases. Observe that the exit jet is fairly horizontal when $\alpha = 60^o$ in Fig. 10, and it is essentially horizontal for $\alpha = 78^o$ as shown in Fig. 11. The Fig. 11 flow pattern is herein referred to as the "horizontal" (H) flow pattern. The change of groove exit jet flow pattern with increasing α can be explained in the light of how the throughflow jet approaches the downstream wall of the rub-groove. Specifically, the inertia of the through-flow jet impacting on the groove downstream wall causes the wall to apply a pressure force that tends to deflect the throughflow jet radially inward, while the inertia of the exit jet gives the tendency to maintain the direction of its approach to the wall. The ultimate direction of the groove exit jet is determined primarily by the balance of these two effects. With the increase of α, the force from the downstream wall changes dramatically so that the groove exit jet angle decreases accordingly.

Examination of the flow patterns for all the cases of x/f = 0.75 reveals the type S flow pattern with a close similarity to that of x/f = 0.5. Due to space limitations, only the flow pattern for $\alpha = 0^o$ with axial position x/f = 0.75 is given (see Fig. 12). Comparison of Fig. 12 to the corresponding case for x/f = 0.5 in Fig. 9 indicates the typical degree of similarity.

For the case of $\alpha = 0^o$ with x/f = 1.0 shown in Fig. 13, the presence of the tooth tip centered at the groove exit prevents the type S flow pattern, so that the type H pattern results. The flow pattern for the x/f = 1.0 cases reveals that all α values from 0 ^{o} through 78 ^{o} exhibit essentially flow pattern H.

2. Pre-Rub Clearance $c^*_{pr} = 4.83\times10^{-4}$

Figure 14 shows the effects of groove wall angle on leakage for cases with pre-rub clearance $c^*_{pr} = 4.83\times10^{-4}$. Comparison of Figs. 14 and 8 shows that downstream

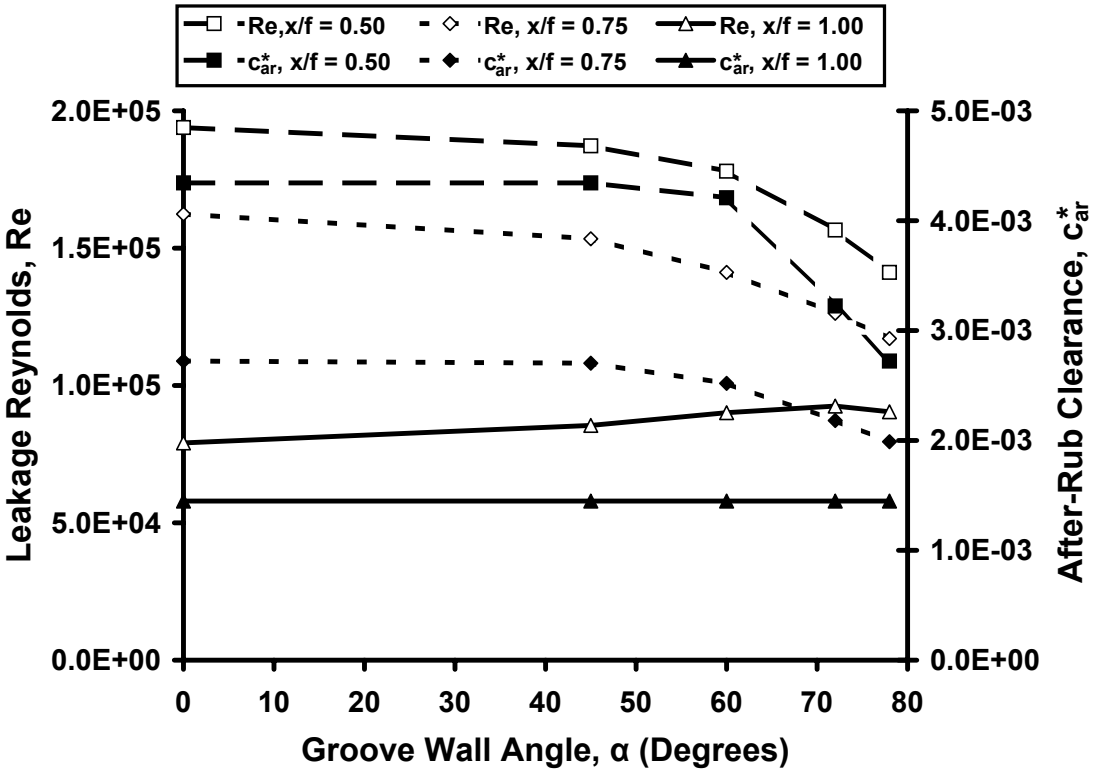

Fig. 8. Effect of the rub-groove slope wall angle for pre-rub clearance $c^*_{pr} = 1.45\times10^{-3}$ on seal leakage and on after-rub clearance for tooth axial position x/f = 0.5, 0.75 and 1.0.

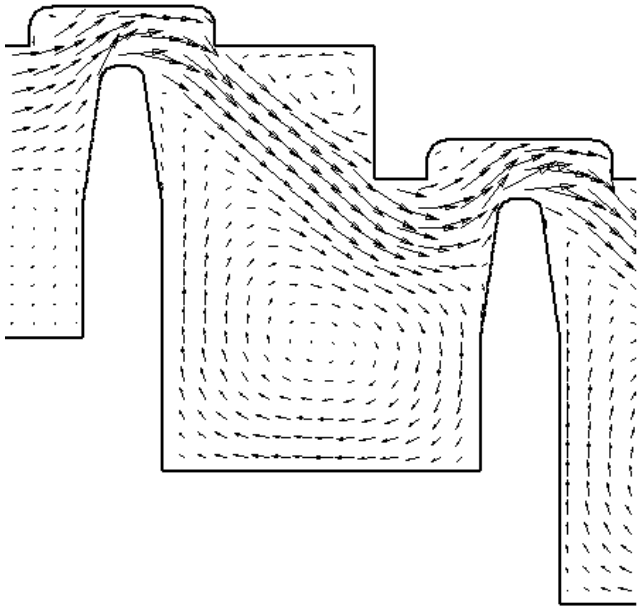

Fig. 9. Flow pattern showing the effect of rub-groove shape ($c^*_{pr} = 1.45\times10^{-3}$, x/f = 0.5, $\alpha = 0^o$).

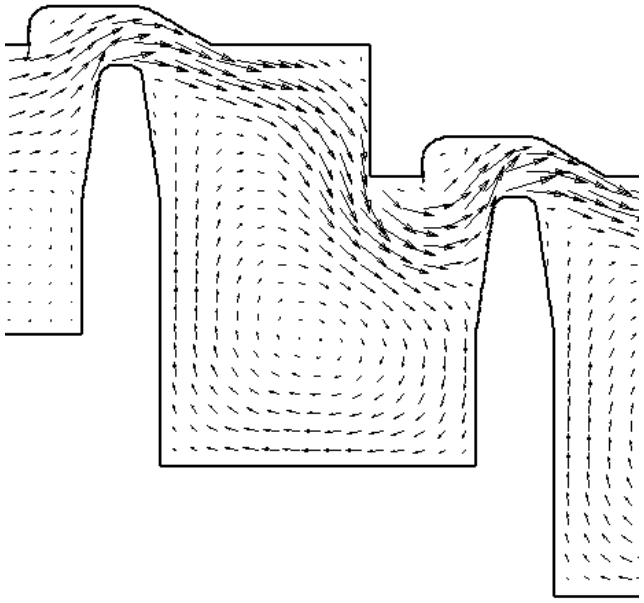

Fig. 10. Flow pattern showing the effect of rub-groove shape ($c^*_{pr} = 1.45\times10^{-3}$, x/f = 0.5, $\alpha = 60^o$).

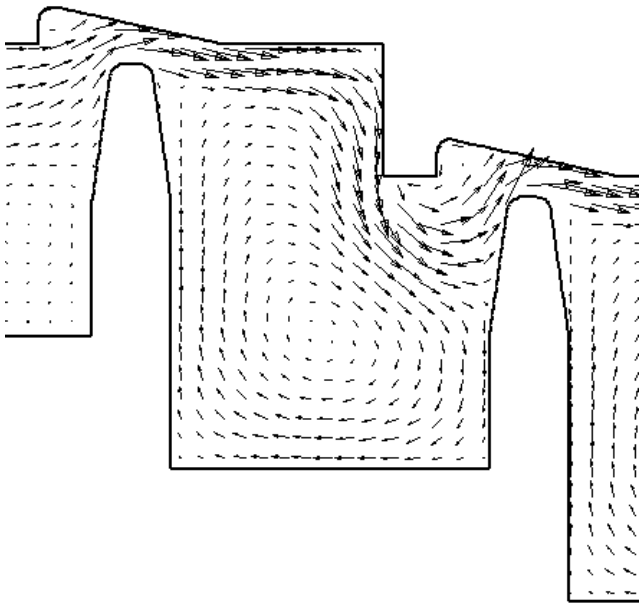

Fig. 11. Flow pattern showing the effect of rub-groove shape ($c^*_{pr} = 1.45\times10^{-3}$, x/f = 0.5, $\alpha = 78^o$).

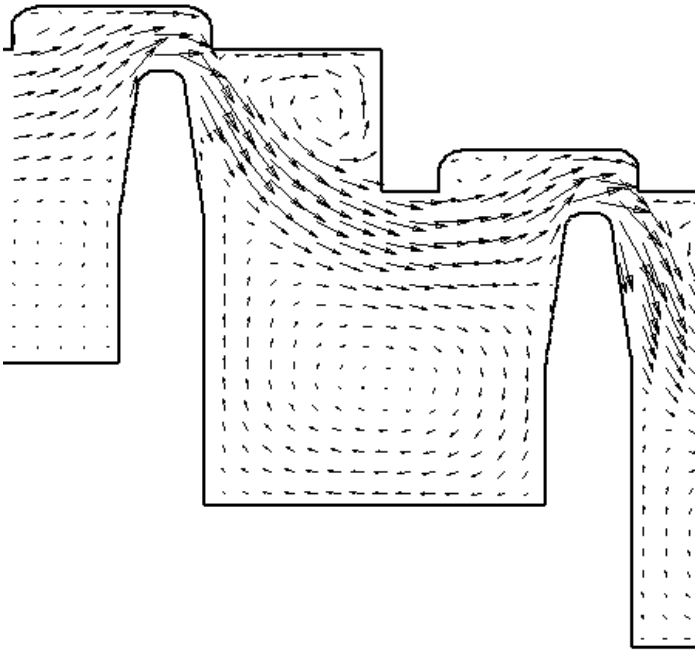

Fig. 12. Flow pattern showing the effect of rub-groove shape ($c^*_{pr} = 1.45\times10^{-3}$, x/f = 0.75, $\alpha = 0^o$).

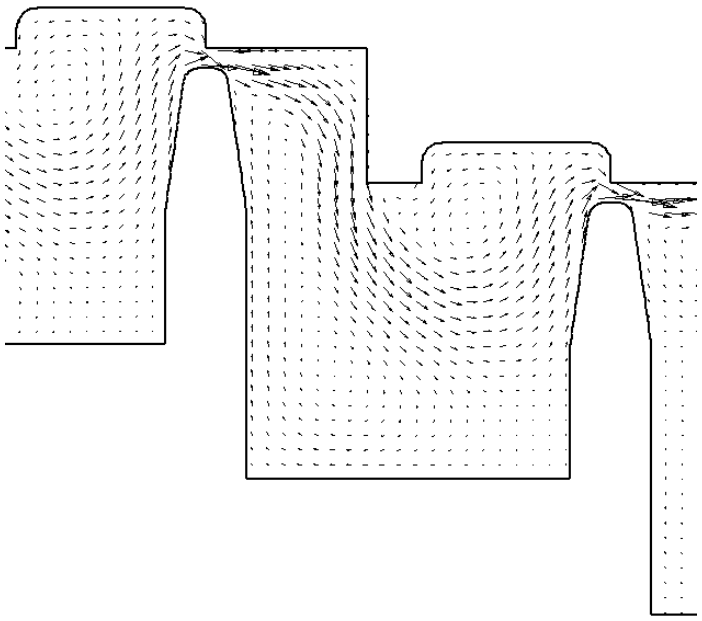

Fig. 13. Flow pattern showing the effect of rub-groove shape ($c^*_{pr} = 1.45\times10^{-3}$, x/f = 0.1, $\alpha = 0^o$).

wall angle α and the tooth axial position x/f have a combined effect on the leakage, as was found for $c^*_{pr} = 1.45\times10^{-3}$. Further examination of the flow patterns for the $c^*_{pr} = 4.83\times10^{-4}$ cases gives additional insight. All but two cases with $c^*_{pr} = 4.83\times10^{-4}$ are quite similar in flow pattern to their corresponding cases with $c^*_{pr} = 1.45\times10^{-3}$. The two exceptions are the case with x/f = 0.75 and $\alpha = 0$ and the case with x/f = 1.0 and α=0^o.

For the case with x/f = 0.75 and $\alpha = 0^o$, Fig. 15 shows that the throughflow jet groove exit angle is almost in the radially inward direction. This groove exit flow pattern is referred to herein as the "vertical" (V) flow pattern. This flow pattern strongly contrasts with that of the corresponding case for $c^*_{pr} = 1.45\times10^{-3}$ in Fig. 12, where flow pattern S occurs. The contrast in flow pattern results from the difference in the radial tooth position. For the case in Fig. 15, the axial tooth position x/f = 0.75 gives a rather small after-rub clearance. This induces very high pressure forces

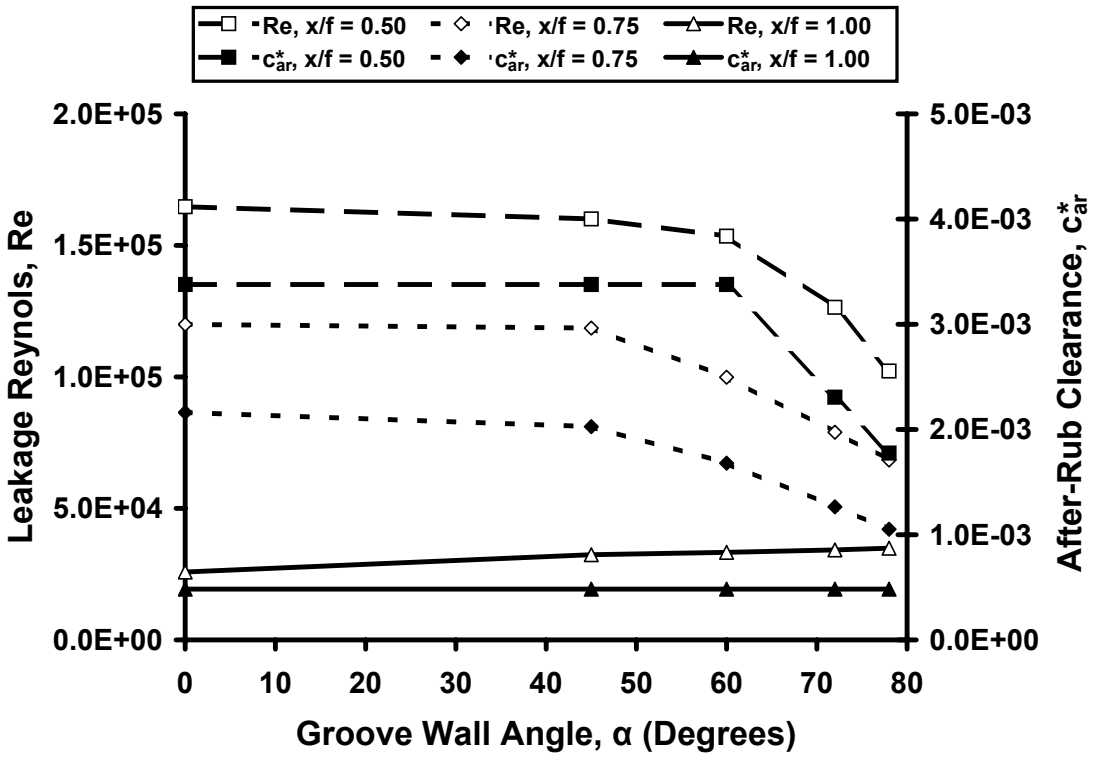

Fig. 14. Effect of the rub-groove slope wall angle for pre-rub clearance $c^*_{pr} = 4.83\times10^{-4}$ on seal leakage and on after-rub clearance for tooth axial position x/f = 0.5, 0.75 and 1.0.

acting on the groove exit fluid near the groove downstream wall, which drives the jet in the radially inward direction as shown.

A very interesting and somewhat different flow pattern occurs for the case of x/f = 1.0 and $\alpha = 0^o$ as shown in Fig. 16. Here the pressure force from the groove vertical wall attempts to deflect the flow radially inward. However, due to the axial and radial position of the tooth, the flow is partially turned in the shaft axis direction by the presence of the flat tooth tip. But before the exit jet is completely turned into the shaft axis direction, apparently its radially inward momentum carries it over the downstream edge of the tooth tip where it continues radially inward along the tooth

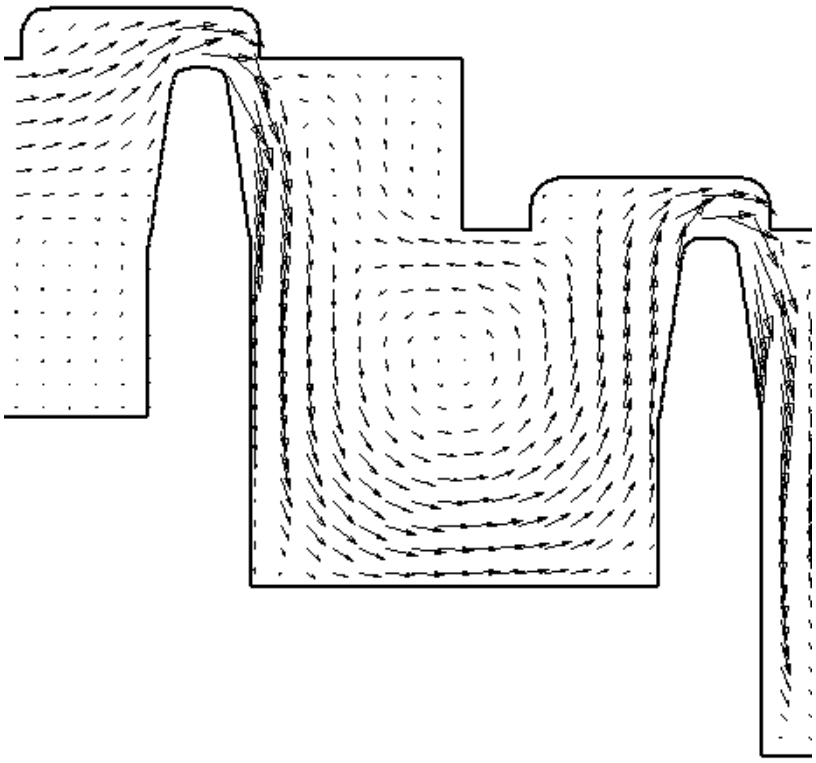

Fig. 15. Flow pattern showing the effect of rub-groove shape ($c^*_{pr} = 4.83\times10^{-4}$, x/f = 0.75, $\alpha = 0^o$).

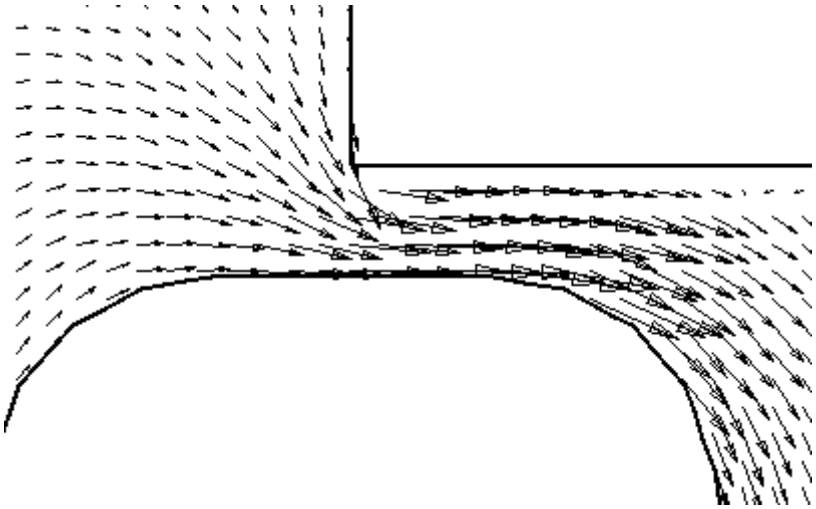

Fig. 16. Flow pattern showing the effect of rub-groove shape ($c^*_{pr} = 4.83\times10^{-4}$, x/f = 1.0, $\alpha = 0^o$).

approximately like that shown in Fig. 15.

3. Pre-Rub Clearance c^*_{pr} = -4.83×10^{-4}

Figure 17 shows the effects of groove wall angle on leakage for cases in which the tooth tip lies within the groove, i.e. c^*_{pr} = - 4.83×10^{-4}. All of the considered cases in Fig. 17 have a flow pattern that is very similar to that of their corresponding cases of pre-rub clearance $c^*_{pr} = 4.83\times10^{-4}$, including the case with x/f = 0.75 and $\alpha = 0^o$.

D. Summary

For a given rub-groove axial length and radial depth, the effect of groove downstream wall angle for a stepped labyrinth seal on compressible flow leakage, was investigated numerically for the first time. It was found that the rub-groove wall angle has significant effects on the leakage, varying with tooth axial position and seal pre-rub clearance. It also drastically affects the flow pattern for some cases. The groove

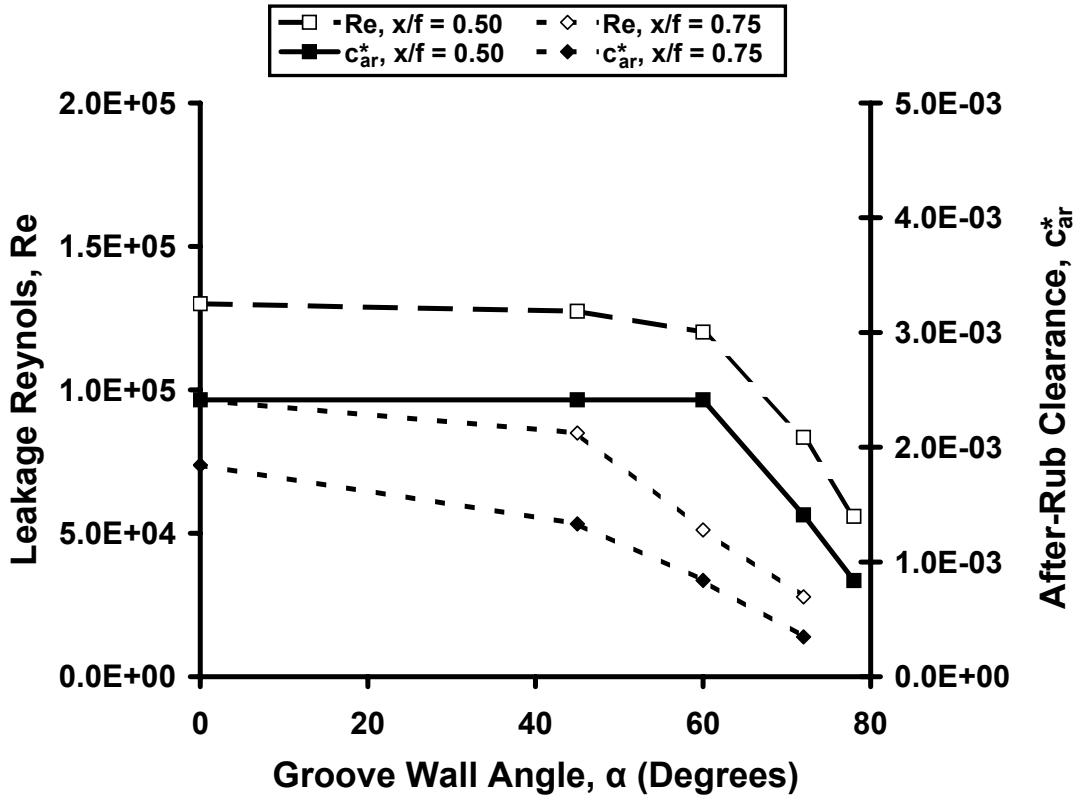

Fig. 17. Effect of the rub-groove slope wall angle for pre-rub clearance c^*_{pr} = -4.83×10^{-4} on seal leakage and on after-rub clearance for tooth axial position x/f = 0.5, 0.75 and 1.0.

shape studied herein has a downstream wall slope angle that was varied from 0^o to 78^o. For the cases considered here, the effects of rub-groove downstream wall angle are summarized as follows.

1. For the three pre-rub clearances considered, an increase of the groove downstream wall angle α decreases the leakage for labyrinth seal cases with tooth axial position x/f = 0.5 and 0.75, while generally increasing the leakage for cases with tooth position x/f = 1.0.

2. The groove wall angle α also affects the flow pattern. For fixed tooth axial position and fixed pre-rub clearance, the flow pattern typically changes fairly gradually with α. However, for certain cases of tooth axial position and pre-rub clearance, for example x/f = 0.75 and $c^*_{pr} = 4.83\times10^{-4}$, the flow pattern changes sharply from $\alpha = 0^o$ (flow pattern V) to $\alpha = 45^o$ (flow pattern H).

3. The effect of rub-groove downstream wall angle on leakage is due largely to the after-rub (minimum) clearance resulting from the rub-groove wall angle and the tooth tip axial and radial position. However, the after-rub (minimum) clearance does not solely determine the leakage. For cases with equal after-rub clearance, leakage variations were definitely observed.

CHAPTER IV

EFFECT OF TOOTH BENDING DAMAGE ON THE LEAKAGE OF LABYRINTH SEALS *

A. Bending Model

Figure 18 shows the schematic view of a tooth before and after bending damage. The broken lines show it before the damage, and solid lines show it afterward. To simulate the details of a specific bent-tooth shape assuming a single value of bend radius of curvature, a fixed-radius bending model was devised. The tooth shape is determined from the user input values for: (1) the location where bending starts, denoted by U, and (2) the after-bend clearance, denoted by c_{ab}. Since all labyrinth seals in the present study have the same pre-bend tooth height, the same pre-bend tooth configuration and the same pre-bend clearance, the use of U and c_{ab} specifies the fixed-radius bending very well. Three assumptions are used in the bending model. The first one is that the bent portion of the tooth centerline is an arc with a particular radius. The second assumption is that the arc of the centerline is tangential to the centerline of the unbent portion. The third assumption is that the only geometry change is due to simple bending as shown in Fig. 18, especially that there is no change of tooth thickness. These assumptions determine that the arc center, arc radius and arc circumferential distance all depend on parameters U and c_{ab}. The first assumption gives the relationship between the bend radius R_b and the bend angle β as

---

* Part of the data reported in this chapter is reprinted with permission from "Effect of Tooth Bending Damage on the Leakage of Straight-Through Labyrinth Seals", FEDSM2005-77455, by Jinming Xu, Matthew S. Ambrosia and David L. Rhode, presented at 2005 ASME Fluids Engineering Division Summer Meeting and Exhibition, June 19-23, 2005, Houston, TX.

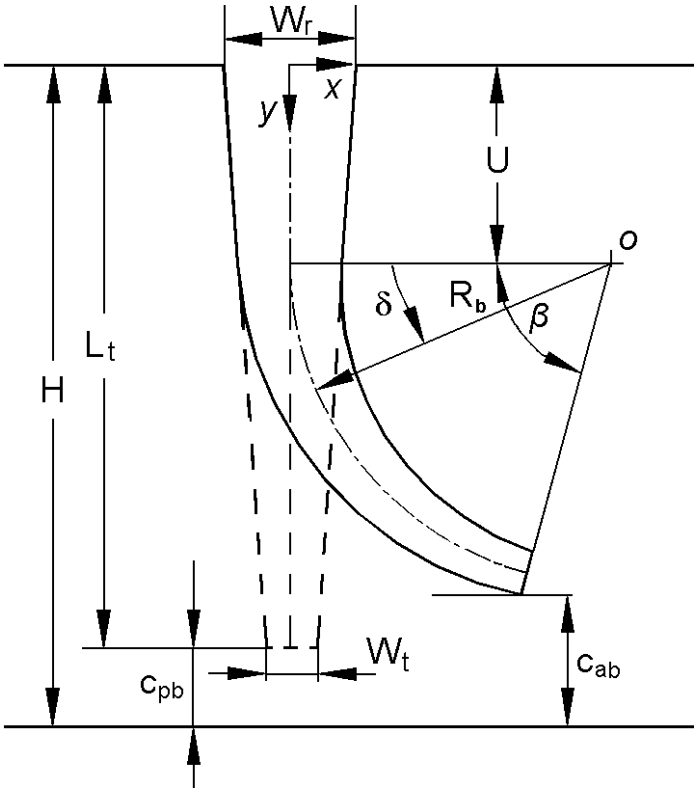

Fig. 18. Tooth geometry before and after permanent bending damage.

$$R_b\beta = L_t - U \tag{4.1}$$

Since the unbent teeth have the shape of a trapezoid, the local tooth width w at an arbitrary location can be expressed as

$$w = W_r - (W_r - W_t)\frac{l}{L_t} \tag{4.2}$$

where l is the distance from the tooth root, measured along the centerline. For a bent tooth, the local tooth width along the bent portion can be expressed using a polar coordinate system with origin at the arc center (see Fig. 18) as

$$w = W_r - (W_r - W_t)\frac{U + R_b\delta}{L_t} \tag{4.3}$$

The y-direction distance from the tooth root to an arbitrary location along the upstream surface of a bent tooth is (see Fig. 18)

$$y = U + (R_b + w/2)sin\delta \tag{4.4}$$

or

$$y = U + (R_b - aR_b\delta + b)sin\delta \tag{4.5}$$

where

$$a = \frac{W_r - W_t}{2L_t} \tag{4.6}$$

and

$$b = \frac{W_r}{2} - Ua \tag{4.7}$$

Realizing that

$$y_{max} = H - c_{ab} \tag{4.8}$$

Equations (4.1), (4.5) and (4.8) can be solved by iteration to obtain the arc radius R_b and arc angle. For all cases in the present study, the bend angle is listed in Table III.

B. Grid and Grid Independence Testing

Figure 19 shows the grid, generated by OpenCFD, around the bent tooth. As one can see, the majority of the grid is filled with Cartesian cells. An extrusion layer, consisting of three sublayers, is created along all the walls. To mitigate the size difference between the wall cells and the other cells, the thickness of the sublayers grows in the outward direction from the wall with an expansion ratio of 1.43. To obtain better resolution of the flow, the grid is refined in both the horizontal and vertical directions around the labyrinth tooth and the clearance.

Grid independence testing was conducted, and the results are shown in Table II. The chosen case has the same boundary conditions as all the other cases studied. Its geometry, except for the tooth bending for which each case is different, is also the same as the other cases. The bending for the grid independence case begins at the point 1.5 mm from the tooth root, i.e. $U = 1.5$mm (see Fig. 18). After bending, the clearance $c_{ab} = 0.762$ mm. All dimensional lengths are non-dimensionalized by the radius of the domain inlet stator surface, and the value used was 0.254 m. In dimensionless form, the unbent length is $U^* = 4.5 \times 10^{-3}$ and the after-damage clearance $c^*_{ab} = 3.0 \times 10^{-3}$.

As seen in Table II, the leakage difference between the highest leakage grid and lowest leakage grid is only about 2%. The intermediate grid with 185×40 cells in the streamwise and transverse directions, respectively, was used for all production computer runs in this study. This is because the intermediate grid has a fairly small number of cells, and the leakage differs only by 0.75% from the next finer grid.

C. Cases Considered

Because a very wide range of turbomachines that have highly varying operating conditions employ labyrinth seals, it is not surprising that a wide range of bent tooth

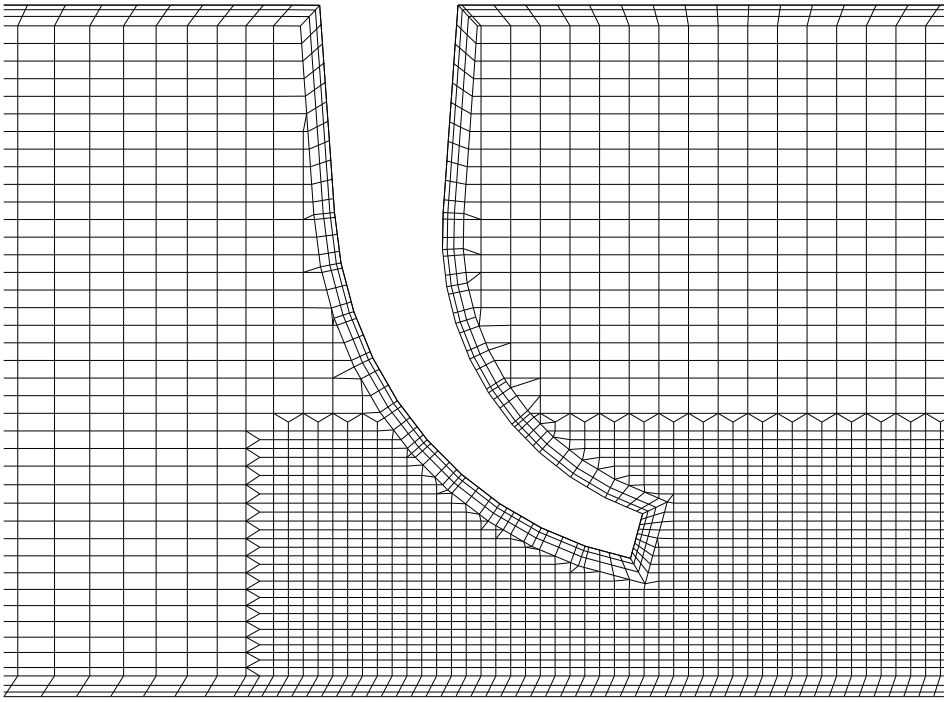

Fig. 19. Grid for the bent tooth showing extrusion layer and embedded refinement.

Table II. Grid independence testing for labyrinth seal tooth damage.

No. of Cells Used		Seal Leakage	$\frac{\dot{m}-\dot{m}_f}{\dot{m}_f}$
Streamwise	Transverse	(kg/s)	
102	22	2.426	2.04%
138	30	2.378	-1.90%
185	40	2.424	0.75%
231	50	2.406	-0.47%
288	62	2.417	-

shapes and after-bend clearances have been found during maintenance operations. After discussions with refurbishment personnel, the tooth bending model discussed above was devised to explore the range of the most likely bent tooth configurations. Tooth bending with tooth tips pointing in the leakage flow direction is considered here because the pressure drop across the seal makes this more likely. Table III defines Case 1 through Case 5L that were assumed to encompass the likely range of moderate tooth bending, although more severe cases have certainly been found from more serious rotor displacement. Gradual rubbing of the seal teeth is not considered here, as this apparently gives "erosion" and/or deformation that is more localized at the tooth tip, as well as sometimes causing rub-grooves in an abradable land when present.

All bent tooth, i.e. $\beta > 0$, cases in Table III have a geometry that results from the bending model above using a pre-bend tooth radial clearance of $c^*_{pb} = 1.0 \times 10^{-3}$.Table III shows that the seals considered operate at a tooth radial clearance c^*, which for

bent tooth cases is called the after-bend c^*_{ab} and for unbent tooth cases is called the pre-bend c^*_{pb}. Cases 2S through 2L, along with Case 1, in Table III are the unbent tooth cases that serve for comparison, and thus have $U^* = L^*_t$ (see Fig. 18). Cases 2S, 2M and 2L have radial clearances $c^* = 2.0 \times 10^{-3}$, 3.0×10^{-3} and 4.0×10^{-3}, respectively, and similarly for Cases 3S through 5L. As we can see from the bending model, for a given U^* the bending arc radius and angle are determined by the pre-bend and after-bend clearances. Since all bent cases have a unique set of pre- and after-bend clearance, they all posess a unique set of bending radius and angle, which expresses the degree of bending in some sense. Further, all of the cases considered are for a three-tooth, straight-through labyrinth with teeth on the stator surface. Figure 20 shows a schematic computational domain for the bending damage investigation. The rotor spins at 1047.2 rad/s (10,000 rpm). Also, the tooth pitch $L^*_p = 0.012$, the tooth height $L^*_t = 0.014$, $R^*_{sh} = 1.0$. Both the domain inlet and outlet have pressure boundary conditions, specifically $P_{t,u} = 1.379 \times 10^6$ Pa (200 psi) and $P_{s,d} = 1.149 \times 10^6$ Pa (166.6 psi). The inlet temperature is 394 ^{o}K (250 ^{o}F) and the entering turbulence is specified with an intensity of 0.1 and a length scale of 1 mm. The direction and magnitude of the inlet velocity were not specified, and thus determined by the flow solution. The downstream pressure was specified as the mean pressure across the outlet. On the two meridional surfaces, cyclic (also termed periodic) boundary conditions were used to account for the circumferential flow repetition.

D. Results

Figure 21 and Table III allow numerous comparisons of bent and unbent teeth for fixed operating conditions, tooth pitch, number of teeth, tooth height, tooth thickness

Table III. Geometry and leakage of the cases studied for tooth bending damage.

Case	c^*	β	U^*	$\dot{m}$	Re
	(10^{-3})	(degrees)	(10^{-3})	(kg/sec)	(10^5)
1	1.0	0.0	14.0	0.51	0.55
2S	2.0	0.0	14.0	1.20	1.31
2M	3.0	0.0	14.0	2.05	2.23
2L	4.0	0.0	14.0	2.87	3.13
3S	2.0	76.27	8.5	1.35	1.47
3M	3.0	107.58	8.5	2.37	2.58
3L	4.0	174.43	8.5	3.28	3.58
4S	2.0	55.39	4.5	1.25	1.37
4M	3.0	72.74	4.5	2.17	2.36
4L	4.0	91.03	4.5	3.15	3.43
5S	2.0	44.20	0.0	1.21	1.32
5M	3.0	60.17	0.0	2.09	2.28
5L	4.0	72.83	0.0	3.08	3.36

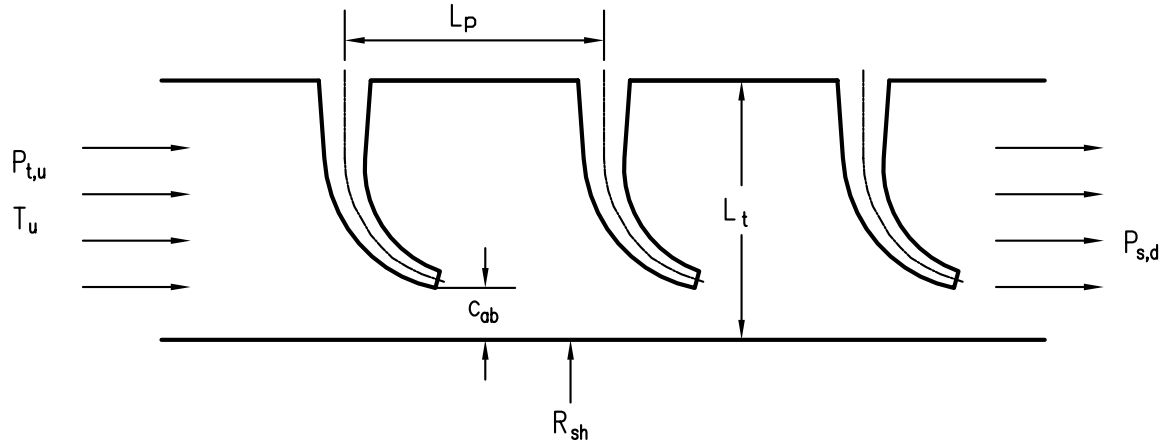

Fig. 20. Schematic computational domain for studying bending damage of a labyrinth seal.

and seal radius. The conventional design that is utilized as the baseline case (Case 1 at operating clearance $c^* = 1.0 \times 10^{-3}$) has unbent (i.e. non-damaged) teeth that have the same pre-bend radial clearance ($c^*_{pb} = 1.0 \times 10^{-3}$) as all of the bent-tooth cases. All cases in Table III other than Case 1 have an operating radial clearance that is greater than the conventional design pre-rub clearance because they have tooth bending or a larger pre-rub clearance to avoid tooth bending. The baseline case is shown in Table III to have a leakage Reynolds number Re = 0.55×10^5. The bent tooth cases considered were divided into three categories of the unbent length U^*. For example, the three bent-teeth cases in the Case 3 category have $U^* = 8.5 \times 10^{-3}$ (see Fig. 18) and have three after-bend radial clearances c^*_{ab} of 2.0×10^{-3}, 3.0×10^{-3} and 4.0×10^{-3} that are denoted in Table III as Cases 3S, 3M and 3L. Further, each of these radial clearances has a distinct bending angle β.

Figure 21 shows the leakage of all the bent cases, as well as the baseline. The leakage ratio on the vertical axis is nondimensionalized by the leakage of the baseline m_o. Observe in Fig. 21 that a substantial tooth bending with $c^*_{ab} = 4.0 \times 10^{-3}$

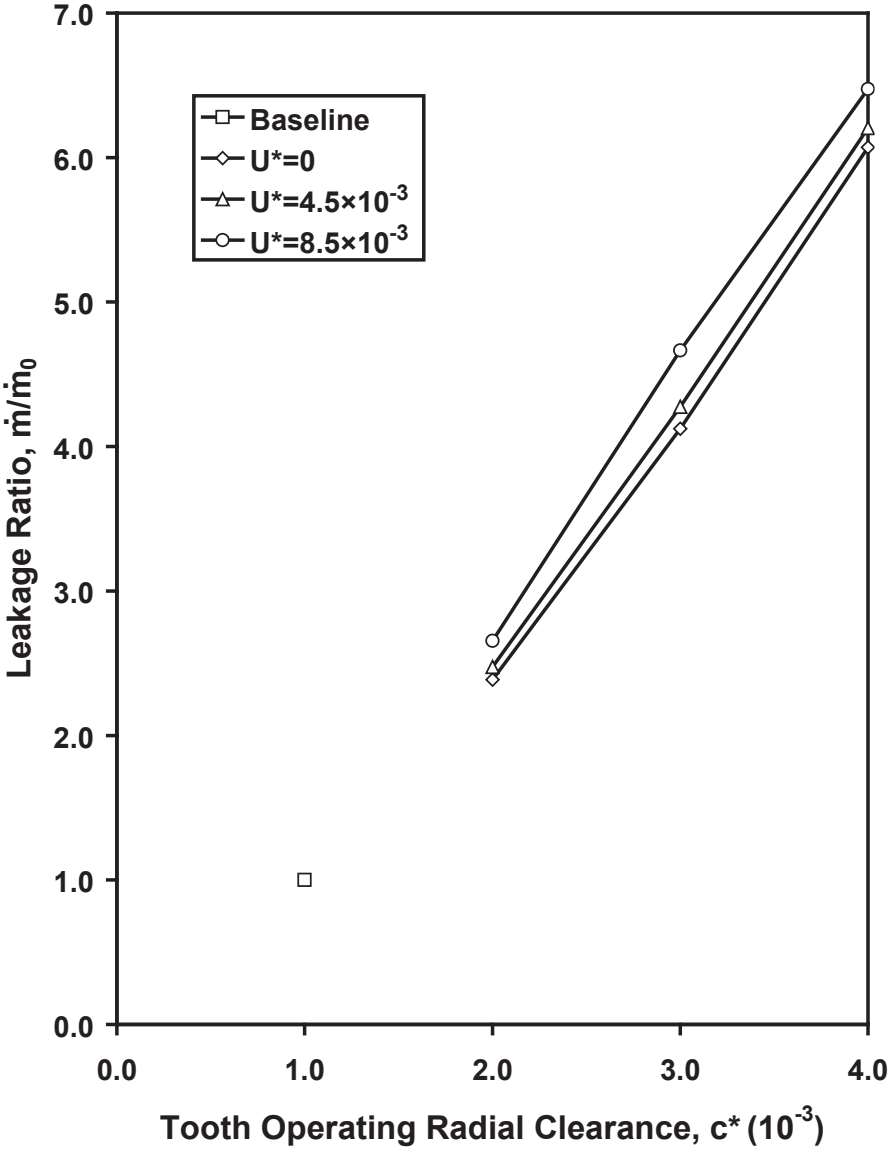

Fig. 21. Leakage variation with operating tooth radial clearance for baseline and bent teeth.

and $U^* = 8.5 \times 10^{-3}$ (Case 3L) gives a leakage increase from the baseline (Case 1) of 543%, which could give a major turbomachine performance concern. Further, a tooth bending of $U^* = 4.5 \times 10^{-3}$ with $c^*_{ab} = 4.0 \times 10^{-3}$ (Case 4L) and $U^* = 0$ with $c^*_{ab} = 4.0 \times 10^{-3}$ (Case 5L) give leakage increases of 518% and 504%, respectively. Apart from tooth bending damage, a labyrinth tooth can also be gradually eroded, resulting in unbent teeth with an increased clearance. One may gain insight concerning this by comparing, at a fixed radial clearance, the three bent-teeth cases with the corresponding gradually eroded-teeth cases. Figure 22 gives the leakage of the unbent, gradually eroded teeth. The solid symbols represent the cases 2S, 2M and 2L listed in Table III. Comparison of the cases in Figs. 21 and 22 shows that the bent cases give more leakage than the gradually eroded teeth. Specifically, for a fixed clearance of 4.0×10^{-3}, bent-teeth Cases 3L, 4L and 5L give a leakage increase over the corresponding gradually eroded Case 2L of 14%, 10% and 7%, respectively. Based on the leakage comparison for the same clearance, an alternative for the designer is to use a larger pre-bend clearance in an attempt to avoid this substantial tooth bending.

In situations where a more slight tooth bending occurs, as for $c^*_{ab} = 2.0 \times 10^{-3}$ with $U^* = 8.5 \times 10^{-3}$ (Case 3S), $c^*_{ab} = 2.0 \times 10^{-3}$ with $U^* = 4.5 \times 10^{-3}$ (Case 4S) and $c^*_{ab} = 2.0 \times 10^{-3}$ with $U^* = 0$ (Case 5S), leakage increases were found over the baseline (Case 1) of 165%, 145% and 137%, respectively.

For further insight into the effect of bending on the flow field, velocity vector plots for the lowest and the highest leakage cases, i.e. Cases 1 and 3L, may be compared in Figs. 23 and 24 (many vectors deleted for figure clarity). In addition to the larger clearance of Case 3L in Fig. 24, one observes the presence of a streamlined nozzle-shaped tooth bending. This is expected to reduce the amount of turbulent friction as found for flow through an ideal nozzle. More evidence of this is found upon comparing the turbulence kinetic energy contours in Figs. 25 and 26 for Cases

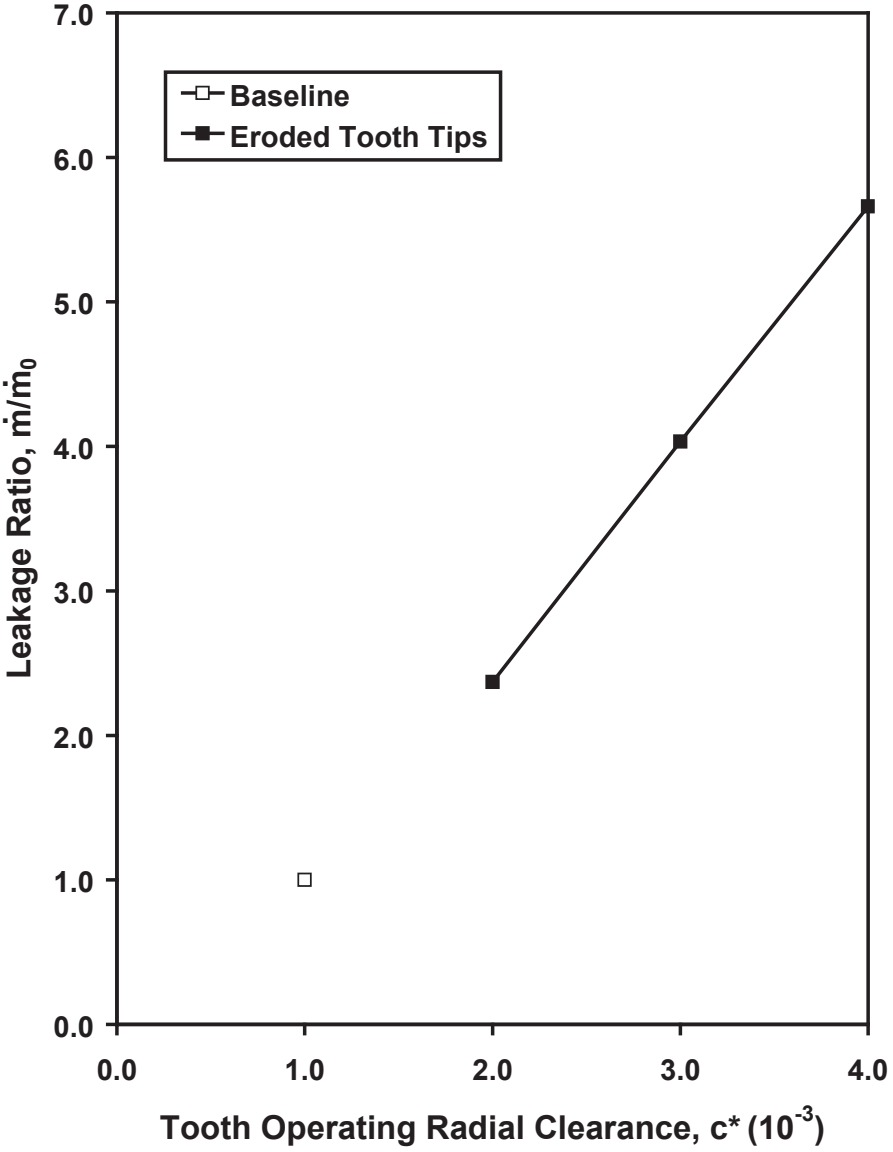

Fig. 22. Leakage variation with operating tooth radial clearance for baseline and gradually eroded teeth.

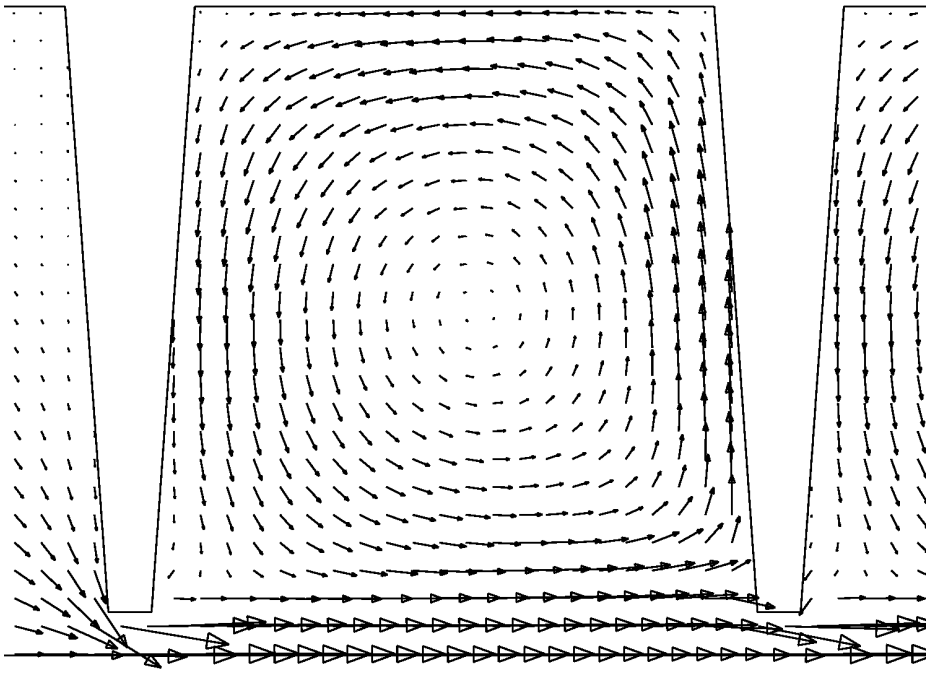

Fig. 23. Flow pattern with gradually eroded teeth for Case 1 ($c^* = c^*_{pb} = 1.0 \times 10^{-3}$).

1 and 3L, respectively. The turbulence kinetic energy is non-dimensionalized by the product of the gas constant R and the upstream inlet temperature T_u. That is,

$$TE^* = \frac{TE}{RT_u}. \tag{4.9}$$

Notice in Fig. 26 that the highest visible value of turbulence kinetic energy is about 0.022, whereas in Fig. 25 it is only about 0.010. The low-friction shape of Case 3L in Fig. 26 leaks much more than the high-friction shape in Fig. 25 due to the over whelmingly large effect of the larger leakage flow area, and consequently the reduced flow-resisting shear stress in Fig. 26. Because of the much larger flow for Case 3L in Fig. 26, there is a higher value of turbulence energy than for Case 1 in Fig. 25.

To gain an enhanced understanding of the effect of the bent tooth shape on the flow field, he may examine a set of cases which share a particular operating clearance.

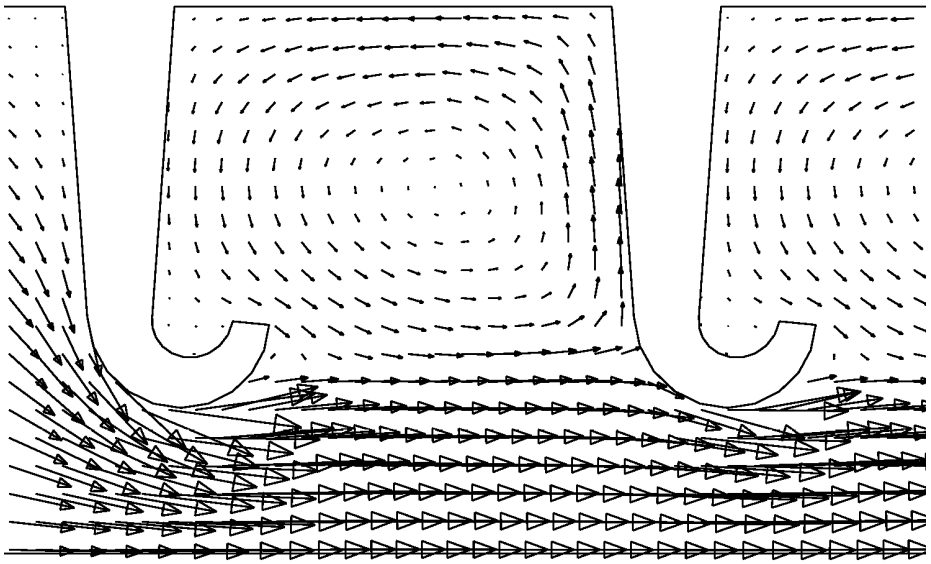

Fig. 24. Flow pattern with bent teeth for Case 3L ($c^* = c^*_{ab} = 4.0 \times 10^{-3}$, $\beta = 174.43^o$, $U^* = 8.5 \times 10^{-3}$).

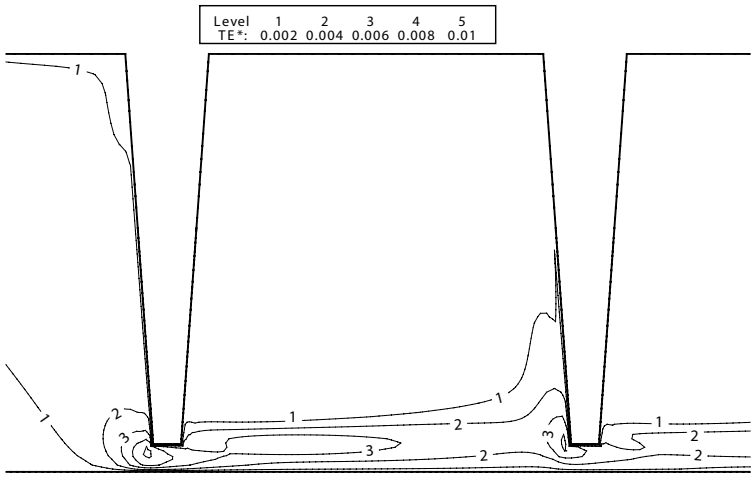

Fig. 25. Turbulence kinetic energy contours with unbent teeth for Case 1 ($c^* = c^*_{pb} = 1.0 \times 10^{-3}$).

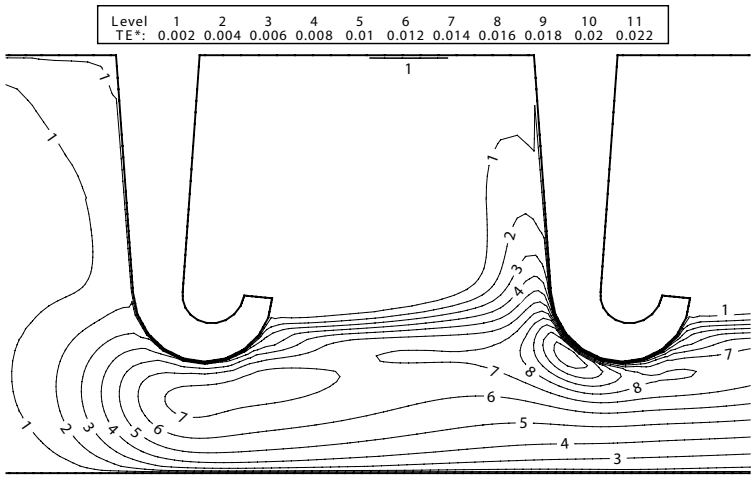

Fig. 26. Turbulence kinetic energy with bent teeth for Case 3L ($c^* = c^*_{ab} = 4.0 \times 10^{-3}$, $\beta = 174.43^o$, $U^* = 8.5 \times 10^{-3}$).

Here we choose the set of cases with the clearance of 4.0×10^{-3}, namely 5L, 3L and 2L. Case 4L, which also has the clearance of 4.0×10^{-3}, is omitted due to its similarity to Case 3L. Of the three chosen cases, Cases 5L and 3L have a dimensionless unbent length of 0 and 8.5×10^{-3}, respectively. Case 2L is unbent and serves for comparison only. Velocity vector plots for Cases 5L, 3L and 2L are shown in Figs. 27, 24 and 28, respectively. For the unbent tooth, the leakage jet passes across the sharp edge of each tooth (see Fig. 28). In contrast, for the bent tooth cases the jet flows along the curved surface of the tooth tips (see Figs. 24 and 27).

The effects of tooth shape among these cases is reflected in the contour plots of turbulence kinetic energy, as shown in Figs. 29, 26 and 30. Observe that the turbulence kinetic energy magnitude and distribution are affected by the tooth shape. That is, Case 3L, which has the sharply curved teeth tips, gives a high level of turbulence kinetic energy and a distribution that does not penetrate much into the labyrinth cavity, whereas the undamaged case in Fig. 30 has significantly more turbulence penetration at a higher energy level. This substantial difference of turbulence energy

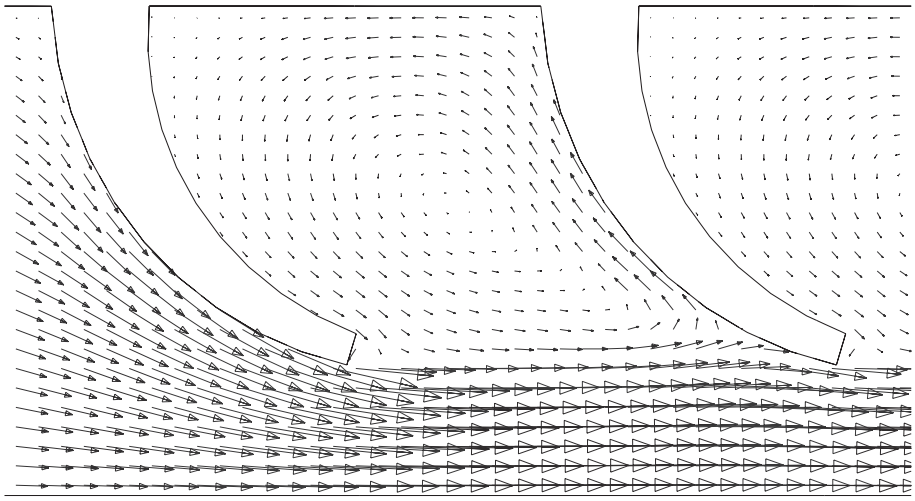

Fig. 27. Vector plots with bent teeth for Case 5L ($c^* = c^*_{ab} = 4.0 \times 10^{-3}$, $\beta = 72.83^o$, $U^* = 0.0$).

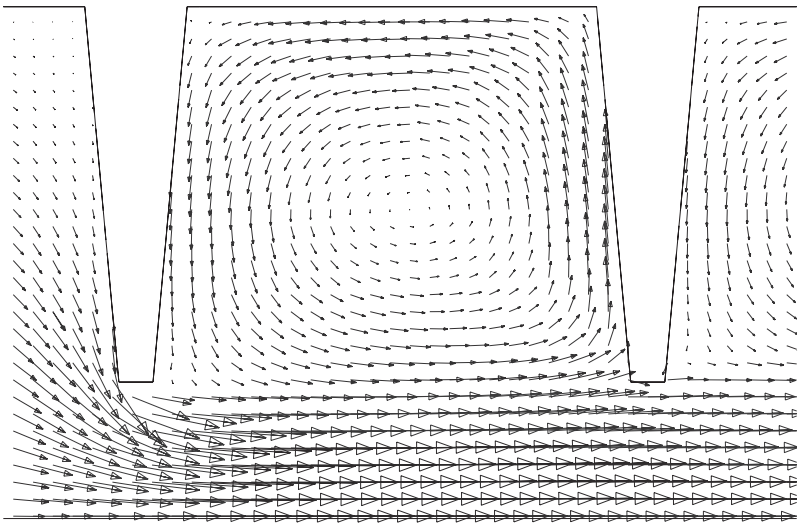

Fig. 28. Flow pattern with unbent teeth for Case 2L ($c^* = c^*_{pb} = 4.0 \times 10^{-3}$).

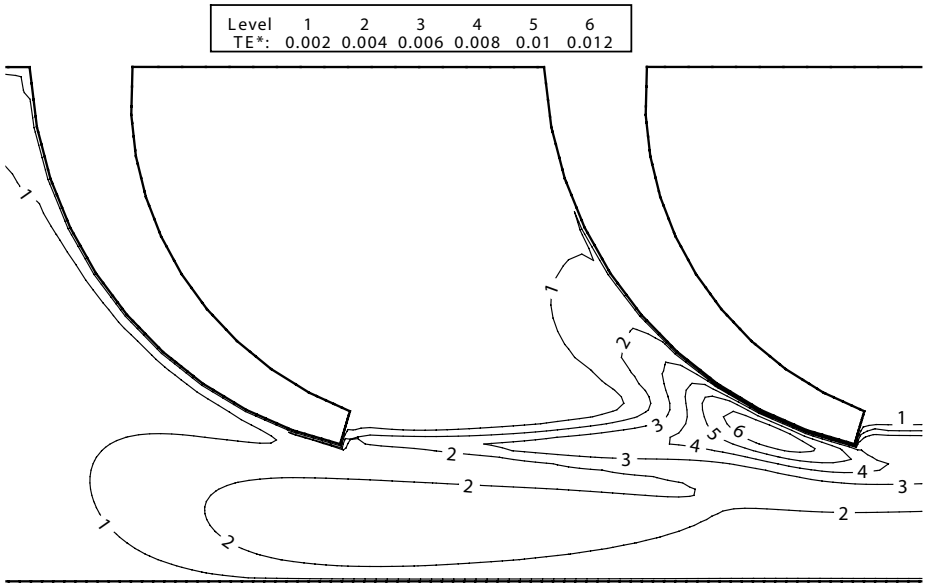

Fig. 29. Turbulence kinetic energy with bent teeth for Case 5L ($c^* = c^*_{ab} = 4.0 \times 10^{-3}$, $\beta = 72.83^o$, $U^* = 0$).

spreading is attributed to tooth, curvature in the presence of a labyrinth velocity field, as it is well known that curvature affects turbulence friction.

Further, each bent-tooth shape has a slightly different leakage. Comparing the bent-tooth cases that have an operating clearance of 4.0×10^{-3} in Fig. 21, one sees that Case 3L (U=8.5×10^{-3}), whose vector plots are shown in Fig. 24, gives a slightly higher leakage, while Cases 5L and 4L give leakages that are lower and quite close. Inspection of these bent tooth geometries shows that Case 3L has a tooth shape with very sharp curvature while Cases 5L and 4L have a slightly less curvature. In addition, for the cases with an operating clearance of 3.0×10^{-3}, Case 3M (U=8.5×10^{-3}) in Fig. 31 and Fig. 32 leads to a slightly larger leakage, while cases 5M and 4M give leakages that are smaller and essentially equal. Inspection of these $c^* = 3.0 \times 10^{-3}$ damaged tooth geometries also shows that the tooth shape with the sharpest curvature (Case 3M in Fig. 31 and 32) gives the highest leakage, while Cases 5M and 4M have slightly

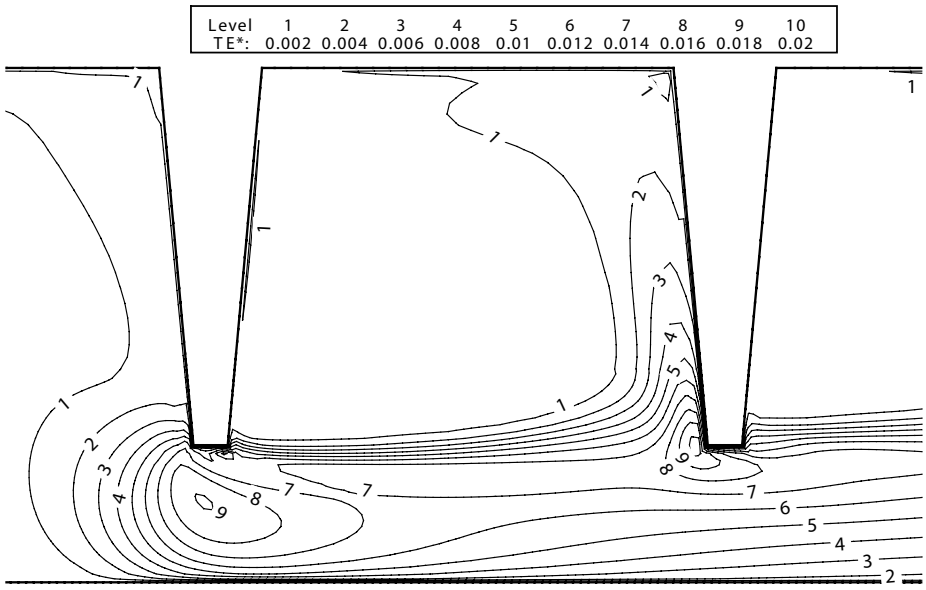

Fig. 30. Turbulence kinetic energy with unbent teeth for Case 2L ($c^* = c^*_{pb} = 4.0 \times 10^{-3}$).

less curvature with slightly lower leakage. For the cases with an operating clearance of 2.0×10^{-3}, the more sharply curved tooth tip again gives the highest leakage.

The effect of the tooth bending angle β, which is coupled with bending radius R_b, is plotted against the leakage in Fig. 33. Figure 33 shows four non-dimensional clearances. For clearance $c^* = 1.0 \times 10^{-3}$, only one unbent case is present. For the other three clearances, bent and unbent cases are present. As shown in Fig. 33, the leakage increases with the increase of bending angle, however the slope of the curves varies for different clearances. For example, the leakage increase with increasing bending angle is slight for clearances $c^* = 2.0 \times 10^{-3}$ and $c^* = 4.0 \times 10^{-3}$, while it is significant for clearance $c^* = 3.0 \times 10^{-3}$.

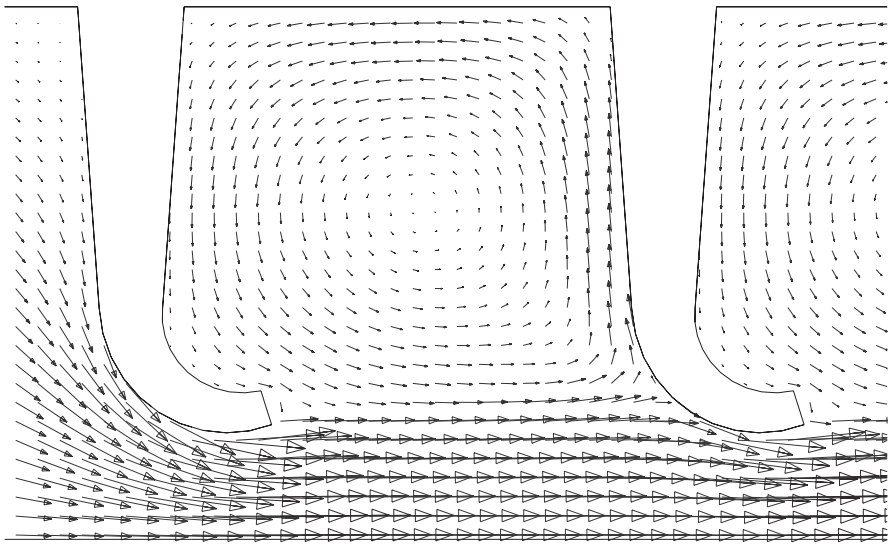

Fig. 31. Flow pattern with bent teeth for Case 3M ($c^* = c^*_{ab} = 3.0 \times 10^{-3}$, $\beta = 107.58^o$, $U^* = 8.5 \times 10^{-3}$).

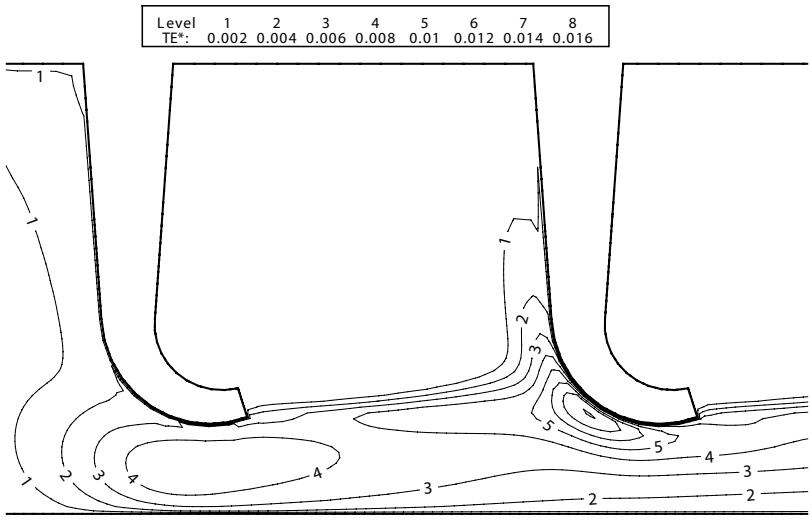

Fig. 32. Turbulence kinetic energy with bent teeth for Case 3M ($c^* = c^*_{ab} = 3.0 \times 10^{-3}$, $\beta = 107.58^o$, $U^* = 8.5 \times 10^{-3}$).

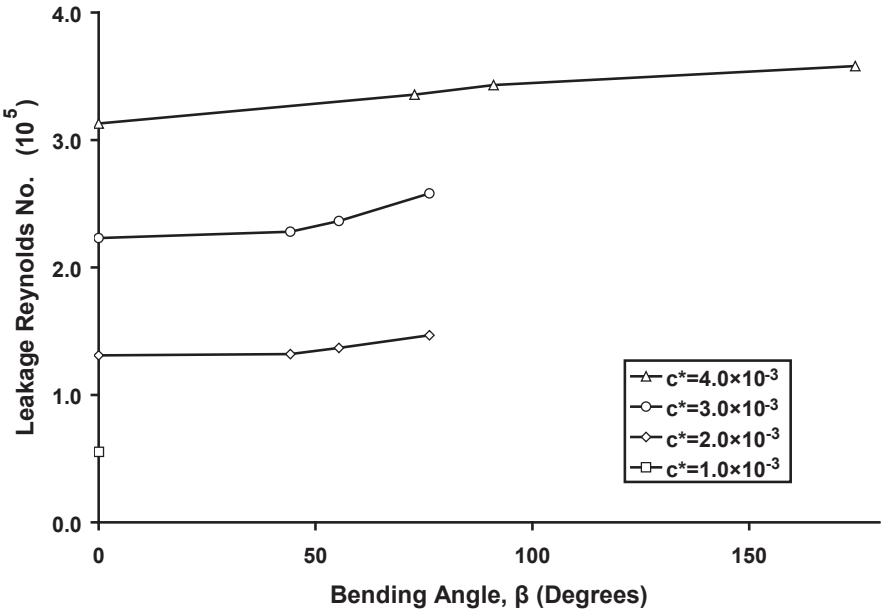

Fig. 33. Effect of tooth bending angle on seal leakage.

E. Summary

A numerical investigation was conducted to determine the effect of permanent tooth bending damage on the leakage of labyrinth seals. Specifically, for the cases considered here the effect of bent teeth can be summarized as follows:

1. Permanent tooth bending damage gives a large increase of operating seal clearance that is the primary cause of a significant leakage increase compared to the undamaged seal. For example, a substantial tooth bending with $c^*_{ab} = 4.0 \times 10^{-3}$ and $U^* = 8.5 \times 10^{-3}$ (Case 3L) gives a leakage increase from the unbent case (Case 1) of 543%, which would probably give a major turbomachine performance concern, depending on the seal application. Further, a tooth bending of $U^* = 4.5 \times 10^{-3}$ with $c^*_{ab} = 4.0 \times 10^{-3}$ (Case 4L) and of $U^* = 0$ with $c^*_{ab} = 4.0 \times 10^{-3}$ (Case 5L) give leakage increases of 518% and 504%, respectively.

2. For a fixed operating clearance, the bent tooth cases give more leakage than the unbent cases. This is attributed to the effect of tooth tip curvature shape on the turbulence energy distribution.

3. The leakage increase caused by tooth bending damage is due largely to the increase of the after-bend clearance, although it is also affected by the tooth tip curvature as well as the bending angle.

CHAPTER V

EFFECT OF MUSHROOM TOOTH TIP DAMAGE ON THE LEAKAGE OF LABYRINTH SEALS

A. Mushrooming Model

Mushroom damage to the labyrinth seal tooth tip can appear in various forms. Researchers from industry have provided several pictures of it. For example, Ghasripoor [23] provided a picture of a mushroomed tooth tip, which shows a flattened and rounded tooth tip with an equal portion of the tooth tip material curled up on each side of the tooth. Also, Ross [22] and Whalen [21] gave a schematic figure showing the mushroomed tooth.

Figure 34 illustrates the geometry used herein to encompass the assumed range of the tooth tip mushroom damage. The thick broken lines represent the labyrinth tooth as originally installed in the turbomachine. The pre-damage clearance c_{pd} is also shown. The thick solid lines give the tooth shape after mushrooming combined with bending. For broad applicability, the curled portion on both sides of the tooth tip has been simplified as a sector of a circle. The circle sectors on both sides have the radius R_m, which is referred to as the "mushroom radius", and they are symmetrically located about the centerline of the labyrinth tooth. The spacing between the centers of the two circle sectors is $2S$. After mushroom damage, the labyrinth seal clearance is increased from the pre-damage clearance c_{pd} to after-damage clearance c_{ad}. For a specific S and c_{ad}, the locations of the two circle sectors are uniquely determined.

In practice, tooth tip mushroom damage can appear on an unbent labyrinth tooth as well as on a bent labyrinth tooth. The present work investigates the mushroom damage on bent as well as unbent teeth. Figure 34 shows mushroom damage on a

bent tooth as well as a bent tooth and an unbent tooth without mushroom damage. One can refer to the "Bending Model" section of the previous chapter to examine the geometrical relationships of the damaged teeth. The mushroom damage combined with bending damage cases studied herein all have a fixed unbent length $U = 1.143$ mm and after-damage clearance $c_{ad} = 0.762$ mm. For the discussion in the following sections, dimensionless parameters will be used. All dimensional lengths will be non-dimensionalized by the radius of the domain inlet stator surface, which approximately equals the shaft radius R_{sh}=0.254 m. After non-dimensionalization, the dimensionless unbent length $U^* = 4.5 \times 10^{-3}$ and the after-damage clearance $c^*_{ad} = 3.0 \times 10^{-3}$.

B. Grid and Grid Independence Testing

The grids were generated by OpenCFD. Figure 35 shows what the grid looks like around the mushroom damaged tooth. Like the grids used for tooth bending in Chapter IV, the majority of the grid is filled with Cartesian cells. An extrusion layer, consisting of three sublayers, is created along all the walls. To mitigate the size difference between the wall cells and the interior cells, the thickness of the sublayers grows in the outward direction from the wall, with an expansion ratio of 1.43. To obtain better resolution of the flow around the labyrinth tooth and the clearance, the grid is refined in both the horizontal and vertical directions.

Since the cases considered for mushroom damage are very similar to that for pure bending damage, from overall computational domain to boundary conditions, the grid indepence testing conducted for tooth bending is also valid for the mushooming study. For more details on the grid independence study, see Chapter IV.

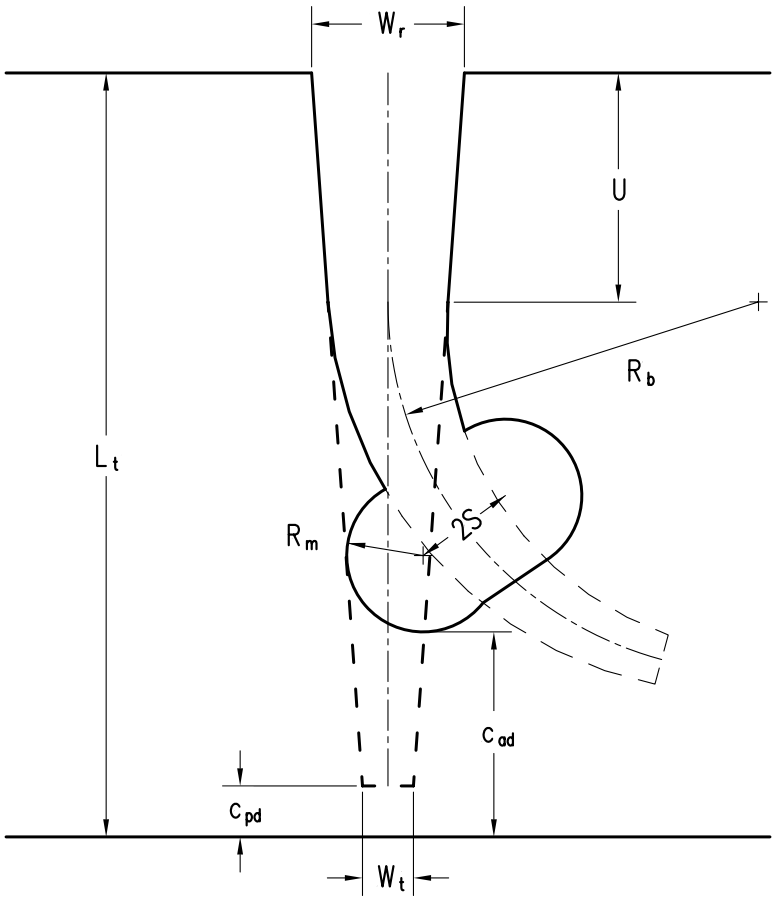

Fig. 34. Tooth geometry before and after tip mushrooming with bending damage as well as pure bending damage.

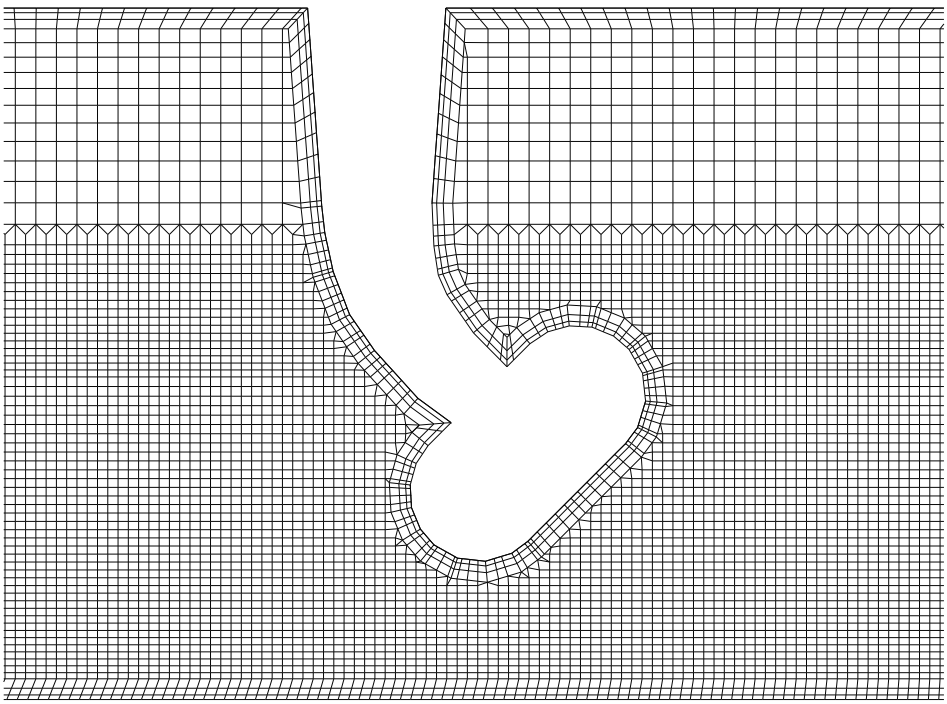

Fig. 35. Grid for the mushroomed tooth with bending showing extrusion layer and refinement.

C. Cases Considered

As mentioned above, mushroomed teeth appear in many forms in practice. For the studies herein, mushroomed teeth with different after-damage clearances c^*_{ad} from 2.0×10^{-3} to 4.0×10^{-3}, are considered. To see the effect of different styles of mushroom damage, cases with different mushroom radii R^*_m and spacing S^* are investigated and compared. The effect of bending damage combined with that of mushroom damage is also discussed. The previous chapter deals solely with bending damage. The present chapter accounts for combined mushroom and bending damage, and investigates how the combination of the two forms of damage affect the leakage.

Table IV lists all the cases studied for mushroom damage. Case 1 and Cases 2S, 2M and 2L, also listed in Table III, are not mushroomed. They are considered here solely for comparison purposes, just as in Chapter IV. To avoid confusion with the Chapter IV cases, the naming of the mushroomed cases begins with 6. Except Case 1, all the cases are named with a number followed by a letter. As in Chapter IV, the letters S, M and L represent small, medium and large after-damage clearances, i.e. 2.0×10^{-3}, 3.0×10^{-3} and 4.0×10^{-3}. The mushroom radius R^*_m and spacing S^* are equal for all mushroomed cases. The two different $R^*_m = S^*$ values considered are 1.0×10^{-3} and 1.5×10^{-3}. Of the mushroomed cases, Cases 6 and 7 are not bent while Cases 8 and 9 are bent (see Fig. 34). The last two columns of Table IV show the leakage mass flow rate and leakage Reynolds number.

As in Chapter IV, all of the cases considered are for a three-tooth, straight-through labyrinth seal with teeth on the stator surface, as found in many centrifugal compressors and pumps. Figure 36 shows a schematic computational domain for the mushroom damage investigation. Both the domain inlet and outlet have pressure boundary conditions, specifically $P_{t,u} = 1.379\times10^6$ Pa (200 psi) and $P_{s,d} = 1.149\times10^6$

Table IV. Geometry and leakage of the cases studied for tooth mushroom damage.

Case	c^*	$R_m^* = S^*$	Bent	$\dot{m}$	Re
	(10^{-3})	(10^{-3})	(Yes/No)	(kg/sec)	(10^5)
1	1.0	-	No	0.51	0.55
2S	2.0	-	No	1.20	1.31
2M	3.0	-	No	2.05	2.23
2L	4.0	-	No	2.87	3.13
6S	2.0	1.0	No	1.55	1.69
6M	3.0	1.0	No	2.35	2.57
6L	4.0	1.0	No	3.31	3.61
7S	2.0	1.5	No	1.56	1.70
7M	3.0	1.5	No	2.45	2.67
7L	4.0	1.5	No	3.41	3.72
8S	2.0	1.0	Yes	1.43	1.56
8M	3.0	1.0	Yes	2.27	2.47
8L	4.0	1.0	Yes	3.17	3.46
9S	2.0	1.5	Yes	1.50	1.64
9M	3.0	1.5	Yes	2.35	2.57
9L	4.0	1.5	Yes	3.26	3.55

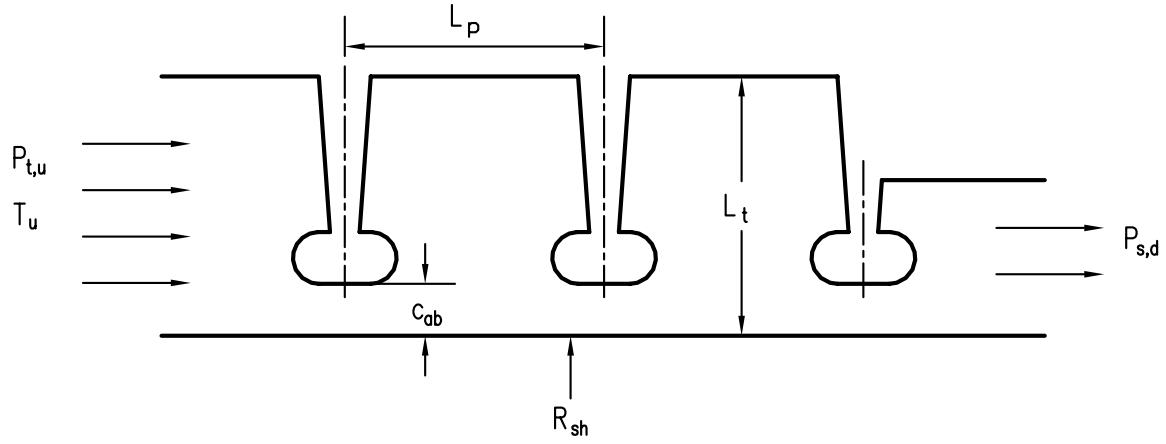

Fig. 36. Schematic computational domain for studying mushroom damage of labyrinth seal.

Pa (166.6 psi). The rotor spins at 1047.2 rad/s (10,000 rpm). The inlet temperature is 394 ^{o}K (250 ^{o}F) and the entering turbulence is specified with an intensity of 0.1 and a length scale of 1 mm. The direction and magnitude of the inlet velocity were not specified, and thus determined by the flow solution. Also, the dimensionless tooth pitch $L_p^* = 0.012$, the dimensionless tooth height $L_t^* = 0.014$, and the dimensionless shaft radius $R_{sh}^* = 1.0$. The downstream pressure was specified as the mean pressure across the outlet. On the two meridional surfaces, cyclic (also termed periodic) boundary conditions were used to account for the circumferential flow repetition.

D. Results

1. Mushroomed Versus Unmushroomed Labyrinths

Table IV gives the leakage of the baseline and damaged cases, while Fig. 37 gives the leakage ratio, nondimensionalized by the leakage of the baseline, of all the cases. In Fig. 37 the baseline (Case 1) is plotted with a hollow square. All of the mushroomed cases are plotted with solid symbols: triangle, square, diamond and circle. Further,

the asterisk symbols (*) represent the pure bending cases for comparison.

Case 1 is the pre-damage, i.e. as initially installed, baseline case that all the damaged cases originate from. In other words, all the damaged labyrinth seals have the same pre-damage clearance (c^*_{pd}=1.0 $\times$ 10^{-3}). As seen in Table IV, Case 1 has a leakage Reynolds number as low as 0.55 $\times 10^5$ with the operating clearance of c^*=1.0 $\times$ 10^{-3}. After the damage occurs, a large increase in leakage is observed, depending mostly on the after-damage clearance c^*_{ad}. For example, when there is severe mushroom damage with $c^*_{ad} = 4.0 \times 10^{-3}$ (Cases 6L, 7L, 8L and 9L), the leakage Reynolds number of the mushroomed cases ranges from 3.46×10^5 to 3.72×10^5, giving an increase of 523% to 570% over the pre-damaged baseline case. When a more mild mushroom damage occurs, as for $c^*_{ad} = 2.0 \times 10^{-3}$, the leakage Reynolds number ranges from 1.56×10^5 to 1.70×10^5, increasing from the baseline by 181% to 207%. Alternately, Fig. 37 provides a more visualized view of the leakage comparison.

To gain further insight into the effect of mushroom damage on the flow field, velocity vector plots for the baseline (Case 1) and the mushroomed case with highest leakage (Case 7L) are compared in Figs. 23 (in Chapter IV) and 38, respectively. Many velocity vectors have been deleted for figure clarity. In Fig. 38, one observes that the upstream portion of the mushroom tooth tip provides a sharply curved flow surface that is locally similar to a flow nozzle. Observe that the leakage flow along this tooth tip shape is much different from that passing across the sharp edges of the pre-damaged teeth in Fig. 23.

Apart from tooth mushroom damage, a labyrinth tooth can also be gradually eroded, resulting in an increased clearance. One may gain insight concerning this by comparing, at a fixed radial clearance, the three bent-teeth cases with the gradually eroded-teeth cases. Figure 22 in Chapter IV gives the leakage of the gradually eroded teeth. The solid symbols represent the cases 2S, 2M and 2L listed in Table III.

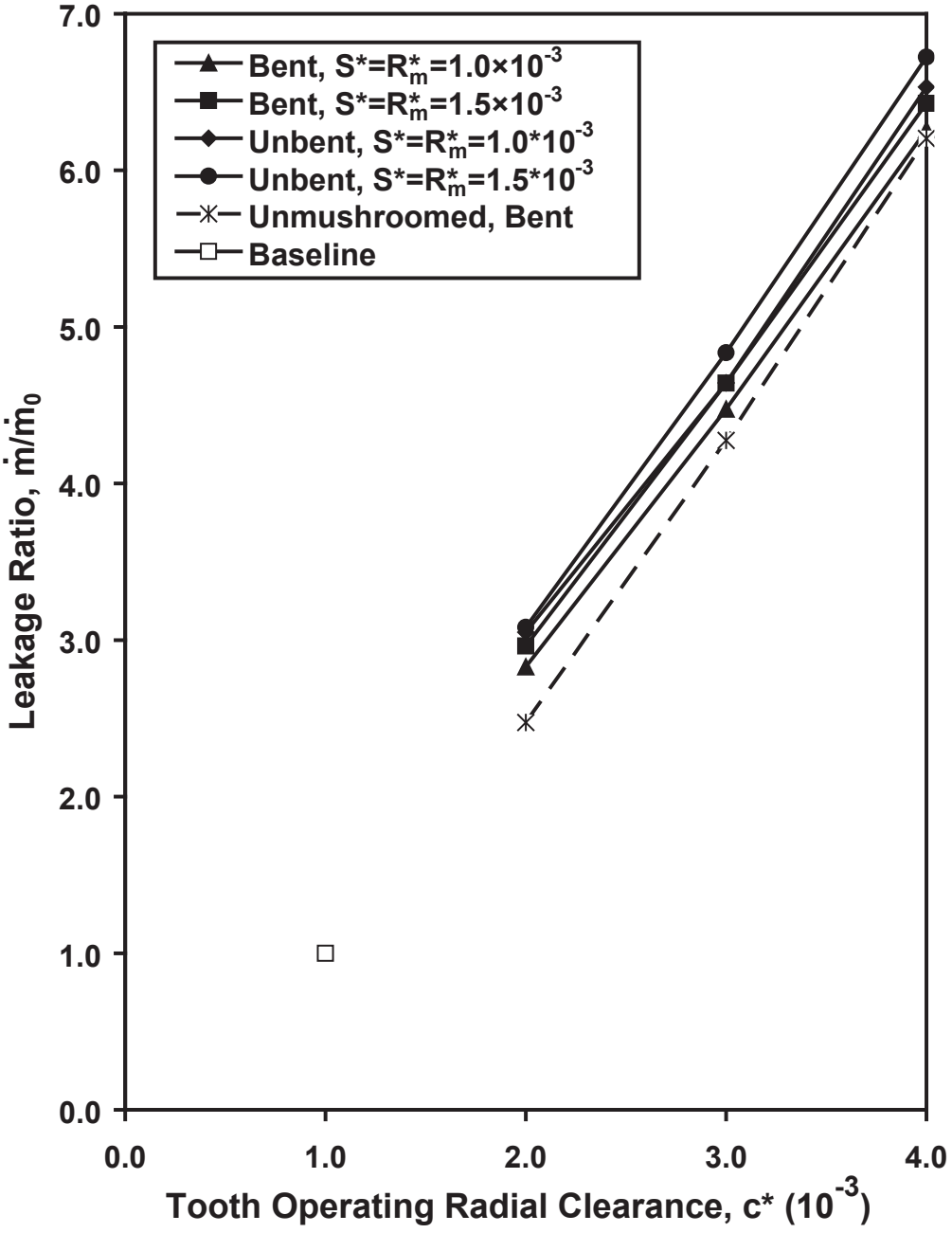

Fig. 37. Leakage variation with mushroomed and unmushroomed tooth radial clearance.

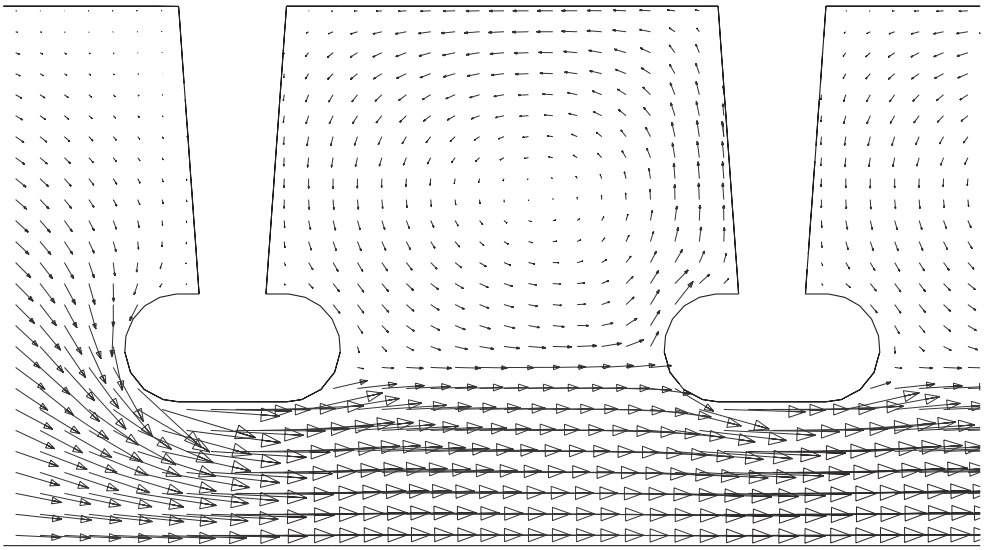

Fig. 38. Flow pattern with mushroomed teeth for Case 7L (unbent, $c^* = c^*_{ad} = 4\times10^{-3}$, $R^*_m = S^* = 1.5 \times 10^{-3}$.

Comparison of the cases in Figs. 37 and 22 shows that all mushroomed labyrinth tooth shapes (solid symbols) give a significantly higher leakage than gradually eroded ones with the same operating clearance. For example, if the labyrinth tooth has an operating clearance $c* = c^*_{ad} = 2.0 \times 10^{-3}$, the mushroomed labyrinth gives a leakage ratio of about 2.84 to 3.09, depending on the radius R^*_m, spacing S^* and the presence of any bending. However an gradually eroded seal with the same operating clearance gives a leakage ratio of 2.38. In other words, the leakage of the mushroomed labyrinth seal is 19% to 30% higher than that of the undamaged or gradually eroded labyrinth with the same clearance. In situations where a more severe mushroom damage occurs, as for $c* = c^*_{ad} = 4.0 \times 10^{-3}$, the mushroomed teeth give a leakage Reynolds number of about 3.46×10^5 to 3.72×10^5, while an gradually eroded seal with the same operating clearance gives a Reynolds number of only 3.13×10^5. That is, the mushroomed labyrinth gives a higher leakage by 11% to 19% compared to an

gradually eroded labyrinth with the same operating clearance.

Maintenance engineers have speculated about any possible benefits of installing replacement labyrinths with a slightly larger clearance when the original labyrinths have damaged teeth. Based on the above comparison, when a maintenance engineer finds mushroom or pure bending tooth damage, one may want to consider a replacement labyrinth with slightly larger clearance to avoid the 10% to 30% leakage increase from the damaged tooth tip shape for a given clearance.

To gain an enhanced understanding of the effect of mushroom tooth damage for a fixed clearance on the flow field, velocity vector plots for an eroded tooth and a mushroomed-but-unbent tooth are compared using Fig. 28 (in Chapter IV) and Fig. 38. As mentioned above, one can see in Fig. 38 that the leakage jet flows along the sharply curved mushroomed tooth tip rather than flowing across the sharp edge of the eroded tooth tips shown in Fig. 28.

For further insight on the effect of mushroom damage, magnified velocity vector plots around the first tooth for an eroded and a mushroomed-and-bent tooth are given in Figs. 39 and 40. One can more clearly see how the leakage jet flows abruptly across the sharp edge of the eroded tooth tip in Fig. 39, while the jet flows along the mushroomed-and-bent tooth tip surface in Fig. 40. The presence of the mushroomed tip also prevents the flow near the tooth from going downward along the tooth. Above the tooth tip in Fig 40, the local velocity along both sides of the tooth is significantly smaller than that of the eroded tooth in Fig. 39. This velocity difference is observed on both the upstream and downstream sides. Also the recirculation flow downstream of the tooth for the mushroomed labyrinth is significantly weakened due to the effect on the flow of the blockage of the mushroom tip. The reduced recirculation downstream of the tooth is apparently related to the turbulence intensity and hence the friction.

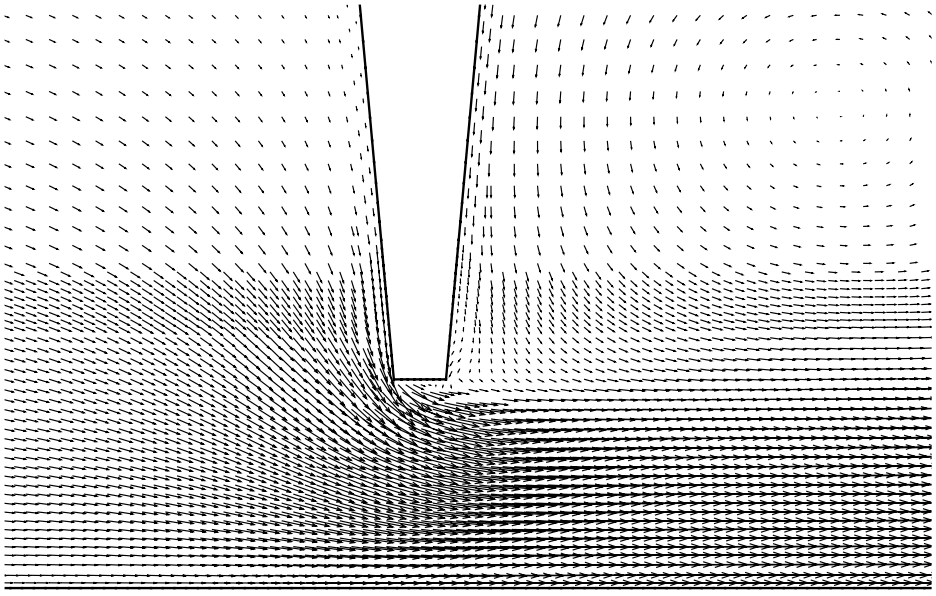

Fig. 39. Flow pattern with the first tooth of gradually eroded labyrinth for Case 2L ($c^* = 4.0 \times 10^{-3}$).

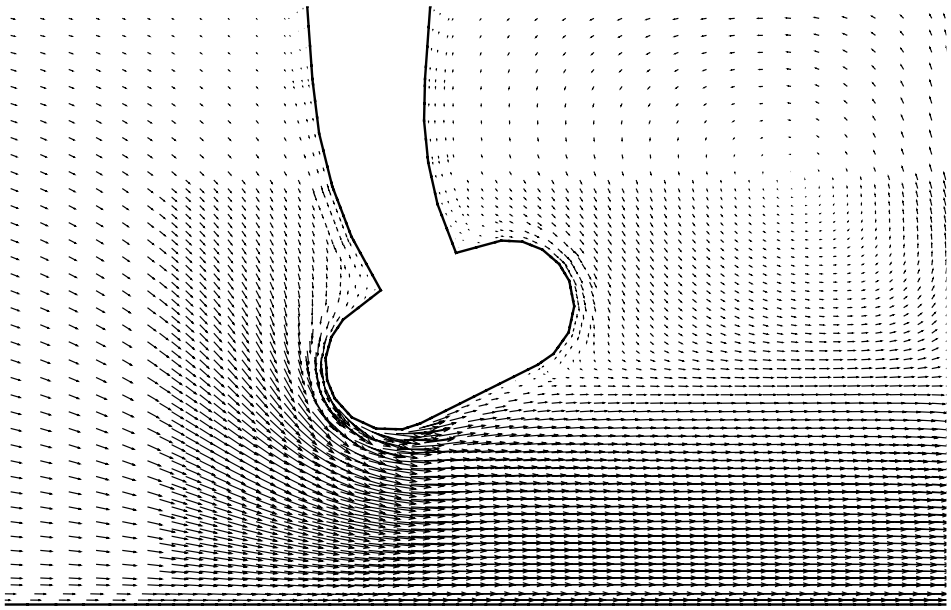

Fig. 40. Flow pattern with the first tooth of mushroomed labyrinth for Case 9L (bent, $c^* = c^*_{ad} = 4.0 \times 10^{-3}$, $R^*_m = S^* = 1.5 \times 10^{-3}$).

As mentioned above, all the mushroomed teeth with bending share a fixed unbent length $U^* = 4.5 \times 10^{-3}$. Comparison can be made between the mushroomed and bent seals, pure-bending seals and pure-mushrooming seals. The bent-only seals are discussed in more detail in the previous chapter; the leakage of those chosen for comparison here is plotted in Fig. 37. One can see from Fig. 37 that the seals with mushrooming and bending give an appreciably higher leakage than the bent-only seals for any after-damage clearance and any mushroom radius.

Specifically, the bent-only seals have $U^* = 4.5 \times 10^{-3}$ and give leakage ratios of 2.49, 4.29 and 6.24 for the after-damage clearances of 2.0×10^{-3}, 3.0×10^{-3} and 4.0×10^{-3}, respectively. For the mushroomed and bent seals with small $R_m^* = 1.0 \times 10^{-3}$, the leakage ratios are 2.84, 4.49 and 6.29, respectively, for the above three after-damage clearances. Observe that these mushroomed and bent seals give a leakage increase over bent-only seals of 14.0%, 4.6% and 0.8%, respectively. For the mushroomed and bent seals with large $R_m^* = 1.5 \times 10^{-3}$, the leakage ratios are 2.98, 4.67 and 6.76 at the after-damage clearances of 2.0×10^{-3}, 3.0×10^{-3} and 4.0×10^{-3}, respectively. This mushroomed and bent group gives a leakage increase of 19.7%, 8.9% and 8.5%, respectively, over bent-only seals.

2. Effect of Mushroom Radius

Figure 37 shows that the leakage of the mushroomed seal is slightly affected by the mushroom radius. It was found that the larger mushroom radius gives a larger leakage. This trend between the mushroom radius and the leakage is observed for all after-damage clearances, and applies to bent and unbent seals alike. Specifically, the mushroomed teeth seals without bending for the smaller mushroom radius of $R_m^* = 1.0 \times 10^{-3}$ have leakage ratios of 3.07, 4.67 and 6.56 at the after-damage clearances of 2.0×10^{-3}, 3.0×10^{-3} and 4.0×10^{-3}, respectively. Further, mushroom seals

without bending for the larger radius of $R_m^* = 1.5 \times 10^{-3}$ have leakage ratios of 3.09, 4.85 and 6.76 at the same three after-damage clearances. This group with the larger mushroom radius gives a leakage increase over the smaller mushroom radius group of only 0.6%, 3.9% and 3.0%, respectively.

A similar leakage effect of the mushroom radius is observed for the mushroomed seal with bending. Specifically, for mushroomed labyrinths with bending, the small mushroom radius of $R_m^* = 1.0 \times 10^{-3}$ gives leakage ratios of 2.84, 4.49 and 6.29 at the after-damage clearances of $2.0{\times}10^{-3}$, $3.0{\times}10^{-3}$ and $4.0{\times}10^{-3}$, respectively. Further, the large mushroom radius of $R_m^* = 1.5 \times 10^{-3}$ gives leakage ratios of 2.98, 4.67 and 6.45 at the same three after-damage clearances. The larger mushroom radius for cases with bending gives increases over the small mushroom radius of 5.1%, 4.0% and 2.6% for the above three clearances, respectively.

For an enhanced understanding of the effect of mushroom radius on the flow field, the turbulence kinetic energy contours of two labyrinth seals with the same after-damage clearance, but different mushroom radii are compared. Figure 41 gives the turbulence kinetic energy of Case 6M that has an after-damage clearance of $c_{ad}^* = 3.0 \times 10^{-3}$ and a small mushroom radius of $R_m^* = 1.0 \times 10^{-3}$, while Fig. 42 gives the turbulence kinetic energy of Case 7M which has the same after-damage clearance but a larger mushroom radius of $R_m^* = 1.5 \times 10^{-3}$. Figures 41 and 42 show that the contours around the second tooth are quite similar in pattern. However, the contours around the first tooth, which experiences a larger pressure drop than the others, demonstrates a difference in pattern. The smaller mushroom radius has a very sharp peak in turbulence kinetic energy, as high as 0.014 as shown in Fig. 41. The larger mushroom radius, comparatively, has a gradual peak, the value being about 0.012 as shown in Fig. 42. This comparison shows that the larger mushroom radius generates a lower value and a more gradual distribution of turbulence energy with

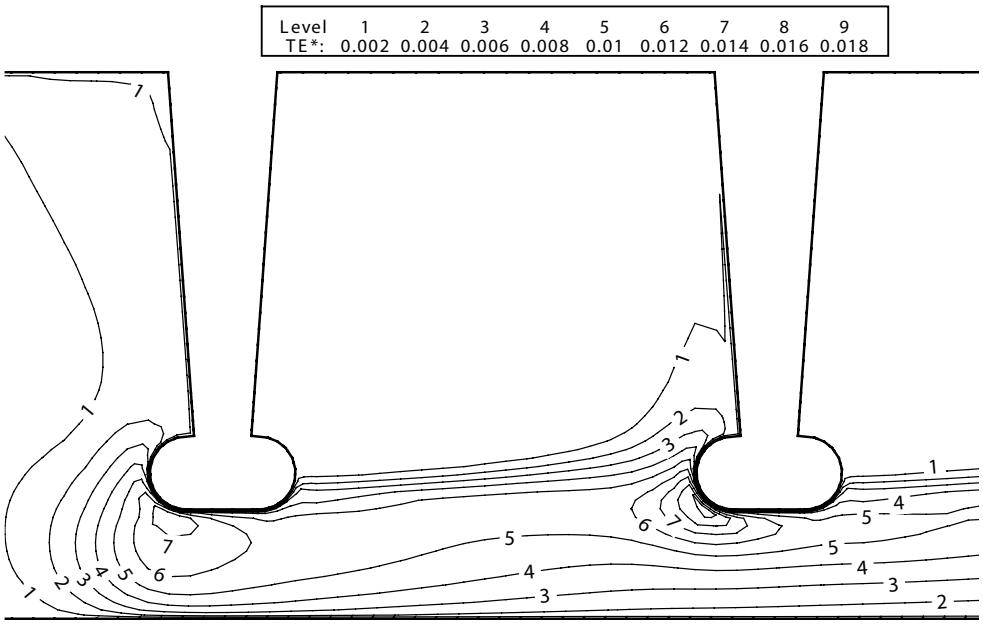

Fig. 41. Turbulence kinetic energy contours with mushroomed teeth for Case 6M (unbent, $c^* = c^*_{ad} = 3.0 \times 10^{-3}$, $R^*_m = S^* = 1.0 \times 10^{-3}$).

lower values near the first tooth, suggesting less turbulence friction, compared to the small mushroom radius. A similar difference in turbulence kinetic energy contours is observed for labyrinth seals at other after-damage clearances, as well as for the mushrooming with bending cases considered.

For further insight on the effect of mushroom radius, vector plots for two mushroomed teeth of different mushroom radii can be compared. Figures 43 and 40 give the vector plots around the first tooth for two mushroomed teeth tips with the mushroom radius R^* of 1.5×10^{-3} and 1.0×10^{-3}, respectively. Though the overall flow pattern looks similar, differences in local velocity vectors exists along the tooth boundaries for the two different mushroom radii. Compared to the small mushroom radius (Fig. 43), the large mushroom radius (Fig. 40) leads to a slightly smaller velocity near the non-mushroomed portion of the tooth. This is especially the case for the velocities

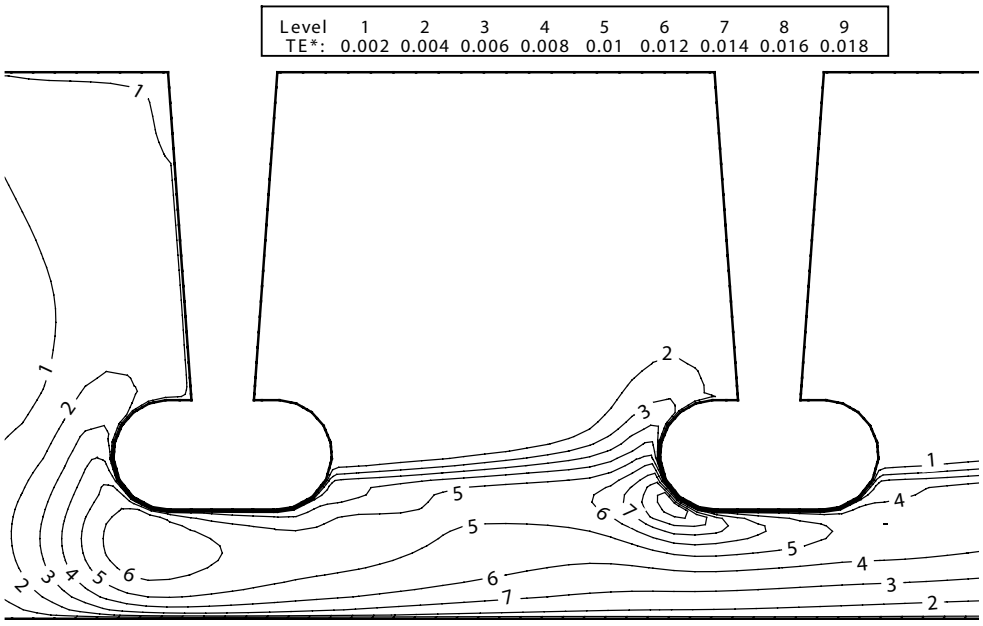

Fig. 42. Turbulence kinetic energy contours with mushroomed teeth for Case 7M (unbent, $c^* = c^*_{ad} = 3.0 \times 10^{-3}$, $R^*_m = S^* = 1.5 \times 10^{-3}$).

at the 90-degree corner formed by the tooth and the mushroomed tip. One also observes that, compared to the small mushroom radius (Fig. 43), the large mushroom radius (Fig. 40) provides a longer and more gradual tooth tip surface curvature which apparently helps to reduce the flow friction.

In chapter IV it was found that when bending radius R_b of non-mushroomed teeth increased, the leakage decreased. It was found in this chapter that when mushroom radius R_m of non-bent tooth increased, the leakage increased. After examining large number of figures at a fixed operating clearance, it was apparent that the different effects of these two radius quantities is as follows. The effect of R_b is that larger R_b allows leakage throughflow to give higher velocity, and hence higher friction, near the upstream surface of the tooth than for smaller values of R_b. (This is especially true for first tooth.) As a result there is lower leakage for larger R_b. The effect of R_m is

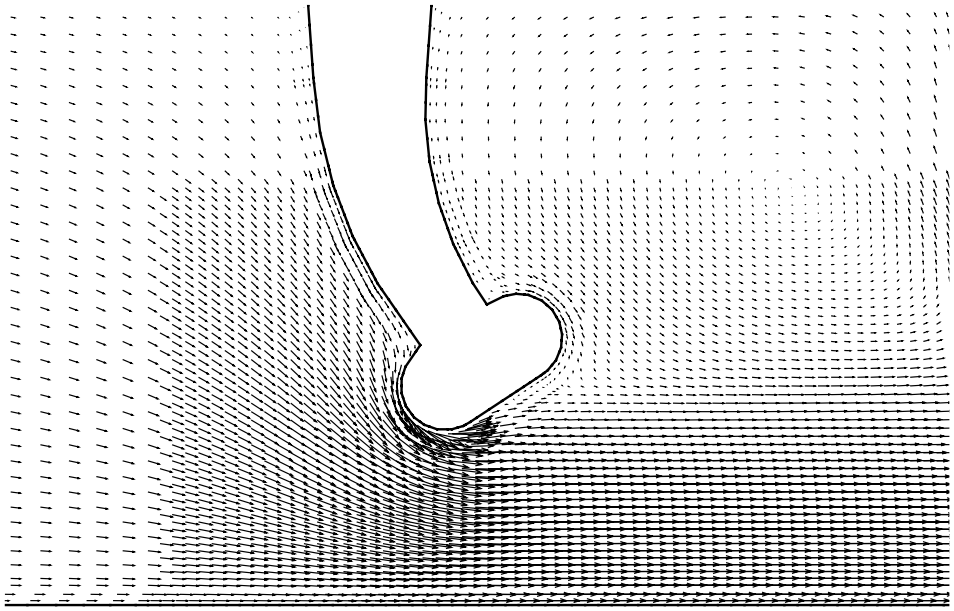

Fig. 43. Flow pattern with the first tooth of mushroomed labyrinth for Case 8L (bent, $c^* = c^*_{ad} = 4.0 \times 10^{-3}$, $R^*_m = S^* = 1.0 \times 10^{-3}$).

much different. That is, larger R_m produces a flow approaching mushroomed tooth tip in a flow pattern that has more gradual turning around the mushroom tip. The more gradual change of direction of flow around mushroom tip at larger R_m is farther away from low-leakage flow pattern of sudden direction change at the sharp-edge (i.e. non-damaged and non-bent) tooth tip of same operating clearance.

3. Effect of Bending on Mushroomed Teeth

Figure 37 shows that the bending of the mushroomed labyrinth seal also affects the leakage. For a mushroomed seal with a fixed after-damage clearance and mushroom radius, the presence of bending gives a lower leakage. Specifically, for the small mushroom radius of $R^*_m = 1.0\times10^{-3}$, the unbent labyrinths have leakage ratios of 3.07, 4.67 and 6.56 at the after-damage clearances of 2.0×10^{-3}, 3.0×10^{-3} and 4.0×10^{-3}, respectively. The mushroomed and bent seals have leakage ratios of 2.84, 4.49 and

6.29 at the same three after-damage clearances. Thus tooth bending gives a leakage decrease of 7.7%, 3.9% and 4.2%, respectively. A similar leakage difference due to bending is observed for the seals with the larger mushroom radius of $R_m^* = 1.5 \times 10^{-3}$. Specifically, for labyrinths with $R_m^* = 1.5 \times 10^{-3}$ the unbent labyrinths have leakage ratios of 3.09, 4.85 and 6.76 at the after-damage clearances of 2.0×10^{-3}, 3.0×10^{-3} and 4.0×10^{-3}, respectively. Seals with bending have leakage ratios of 2.98, 4.67 and 6.45 at the same three after-damage clearances, giving a decrease from unbent labyrinths of 3.5%, 3.7% and 4.6%, respectively.

For further insight, turbulence kinetic energy contours for Cases 7L and 9L, both of which have an after-damage clearance $c_{ad}^* = 4.0 \times 10^{-3}$ and mushroom radius $R_m^* = 1.5 \times 10^{-3}$, are shown in Figs. 44 and 45. The unbent seal has a peak of dimensionless turbulence kinetic energy under the first tooth of about 0.014 in Fig. 44, while the bent seal has a peak of 0.018 in Fig. 45, i.e. 29% higher than the unbent cases, at the same location. Further inspection of the turbulence kinetic energy contours in Figs. 44 and 45 indicates that turbulence kinetic energy under both teeth is generally higher for the bent seal.

In short, for mushroomed teeth, the presence of tooth bending decreases the leakage. However, for labyrinth teeth without mushroom damage as discussed in Chapter IV, the tooth bending increases the leakage. That is, the tooth bending has opposite effect on the leakage for labyrinth teeth with and without mushroom. This difference in the effect of tooth bending can only be explained by the presence of the mushroomed tooth tip. The mushroomed tooth tip affects the flow field, and the effect of mushroomed tooth tip is always superposed on the effect of tooth bending for the mushroomed teeth. In other words, for the tooth with mushroom damage, the effect of bending is not seperate and always mixed with the effect of mushroom. But for the tooth without mushroom damage, the effect of bending is isolated, Note

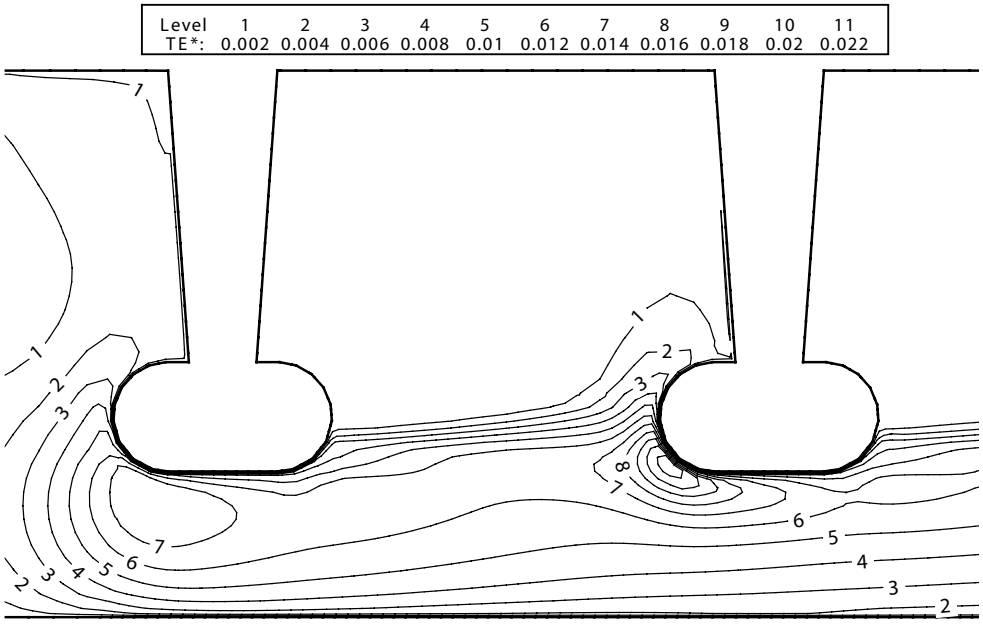

Fig. 44. Turbulence kinetic energy contours with mushroomed teeth for Case 7L (unbent, $c^* = c^*_{ad} = 4.0 \times 10^{-3}$, $R^*_m = S^* = 1.5 \times 10^{-3}$).

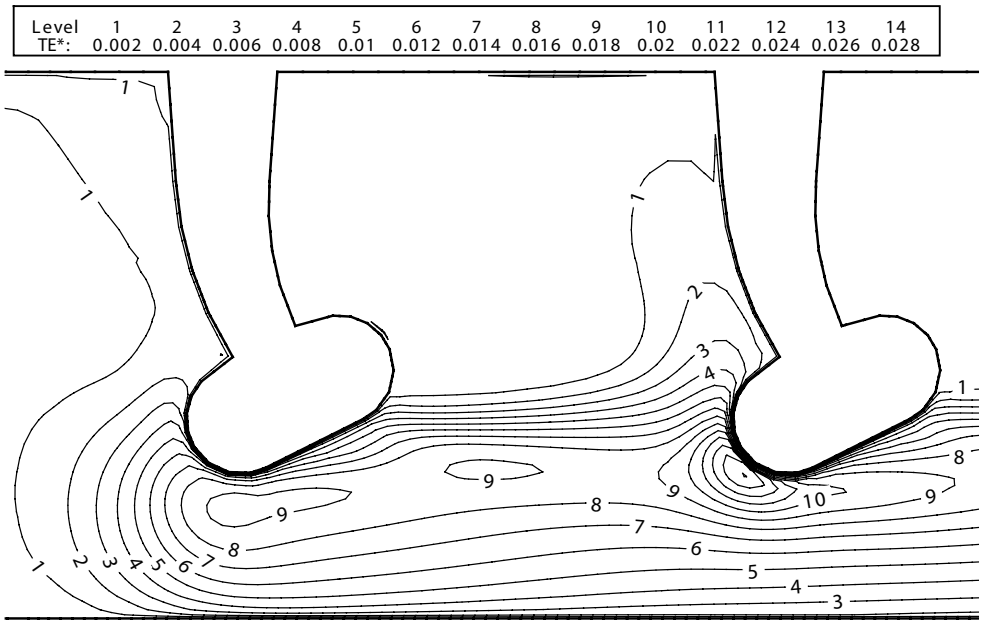

Fig. 45. Turbulence kinetic energy contours with mushroomed teeth for Case 9L (unbent, $c^* = c^*_{ad} = 4.0 \times 10^{-3}$, $R^*_m = S^* = 1.5 \times 10^{-3}$).

for both the teeth with or without mushroom damage,

E. Summary

The present study numerically investigates the effect of mushroom damage on the leakage of labyrinth seals. The computation is conducted on a three-tooth straight-through labyrinth seal, with air as the fluid. The finite-volume based commercial code STAR-CD is used to solve the RANS equations. The high-Reynolds $k-\epsilon$ model and the standard wall function is used to model the flow field.

For the cases considered here the specific findings are summarized as follows:

1. A labyrinth seal gives much higher leakage after the mushroom damage occurs, for unbent as well as bent teeth. The leakage increase ranges from 181% to 570%, depending mostly on the after-damage clearance.

2. A mushroomed labyrinth seal also gives significantly higher leakage than an undamaged seal operating at the same clearance. This is attributed to the fact that the mushroomed tooth tip has a sharp curved surface that affects the turbulence kinetic energy. For a fixed operating clearance, the mushroomed seal gives a leakage higher than the undamaged seal by 11%-30%, depending on the specific clearance and the shape of the mushroom tooth tip.

3. For any fixed after-damage clearance c_{ad}, a larger mushroom radius always gives a higher leakage, regardless of the presence of tooth bending. For seals with a fixed after-damage clearance, the mushroomed seal with mushroom radius $R_m = 1.5 \times 10^{-3}$ gives a leakage higher than that of $R_m = 1.0 \times 10^{-3}$ by 0.6% to 5.1%.

4. The leakage increase caused by mushroom damage is influenced by the presence

of tooth bending. For any fixed after-damage clearance c_{ad}, a mushroomed seal with tooth bending always gives a lower leakage compared to a mushroomed tooth without bending, regardless of the mushroom radius. For a fixed after-damage clearance, the mushroomed seal with bending gives a leakage lower than that of the mushroomed seal without bending by 3.5% to 7.7%, depending on the specific after-damage clearance c_{ad} and mushroom radius R_m.

CHAPTER VI

EFFECT OF LABYRINTH SEAL RUB-GROOVE AXIAL POSITION AND WALL ANGLE ON GAS TURBINE INGRESS HEATING

A. Problem Definition

The industrial gas turbine under present study has a disc radius that is extremely large, compared to that of aircraft engines. The stator-rotor wheelspace, also termed front cavity or forward cavity in the literature, in the present study includes three labyrinth seals: a single-tooth seal at both the outer and inner regions with a dimensionless radial clearance of 2.930×10^{-3} and 2.686×10^{-3} respectively, and a three-tooth seal in the middle with a tight pre-rub dimensionless clearance of 4.88×10^{-4}. A sector of the wheelspace showing the outer two labyrinth seals is shown in the schematic computational domain in Fig. 2. A meridional view of the upper wheelspace, which more clearly shows the outer seal and a downstream tooth of the middle seal, is also available in Fig. 46.

The circumferentially and axially averaged pressure in the mainstream platform axial gap P_{msg}, is fairly constant. The mainstream circumferential pressure asymmetry ΔP studied herein is about 15 percent of the mainstream pressure. For comparison purposes, a few cases with a pressure asymmetry of 10 percent are also studied.

In the lower part of the wheelspace is the coolant/purge feed slot, with a cross section roughly approximated as a square (see Fig. 2). At about the same radial position on the rotor are the coolant receiver holes, simplified as a circumferentially continuous slot. The slot has the same flow area as the total area of the discrete coolant reveiver holes. This simplification will not appreciably affect the flow in the middle and outer cavities, which are far away and isolated by the three-tooth seal

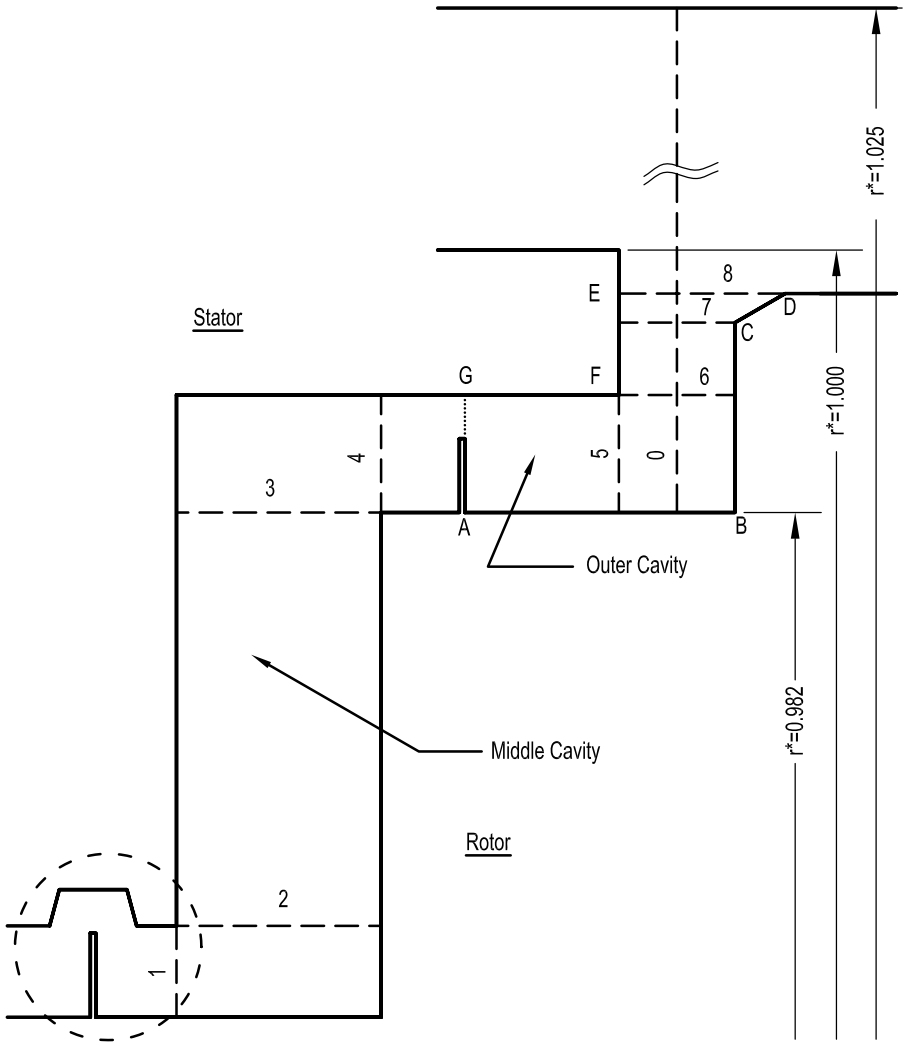

Fig. 46. The meridional view of the mid- and outer- cavities in the wheelspace showing reference planes 0 through 8.

from the receiver holes. At the bottom of the computational domain, there is a one-tooth labyrinth seal, labeled as the inner labyrinth outlet in Fig. 2, which discharges a small portion of the feed slot flow. The feed slot, the receiver holes and the inner outlet are all at the same dimensionless temperature.

In accordance with the tight clearance of the three-tooth labyrinth seal in the middle wheelspace cavity, the surface opposite to the labyrinth tooth is abradable. When the engine undergoes transients such as starting up or shutting down, the labyrinth teeth will unavoidably rub into the opposite surface and form grooves on it. The groove formation is influenced by the stator and rotor operating conditions, the differential thermal expansion rate of the stator and rotor in the axial and radial directions, rotordynamics and the assembly tolerance stack-ups, etc. This situation is complicated, making it very difficult to accurately predict the exact location and geometry of the rub-grooves during the design phase of an engine. To gain an enhanced understanding of the influence of rub-groove axial location and geometry, rub-grooves with two different wall angles and at four different axial locations are simulated. The shape and location of labyrinth seal rub-grooves simulated in the present study is illustrated in Fig. 47, which gives a magnified view of the right-hand tooth and rub-groove in Fig. 2 and as circled in Fig. 46. The four different axial positions 1, 2 3 and 4 are shown in Fig. 47. Non-dimensionalizing d by the stator disc radius gives d^* of 5.80 $\times 10^{-3}$, 4.88 $\times 10^{-3}$, 4.19 $\times 10^{-3}$ and 2.69 $\times 10^{-3}$ for axial positions 1 to 4, respectively. Apart from its axial position, the rub-groove also varies in wall angle. Two different angles are studied in the present work, specifically 15^o and 45^o. The wall angles α are measured from a vertical line defined in Fig. 47. The solid lines in Fig. 47 show the angle of 15^o, while the broken ones show 45^o.

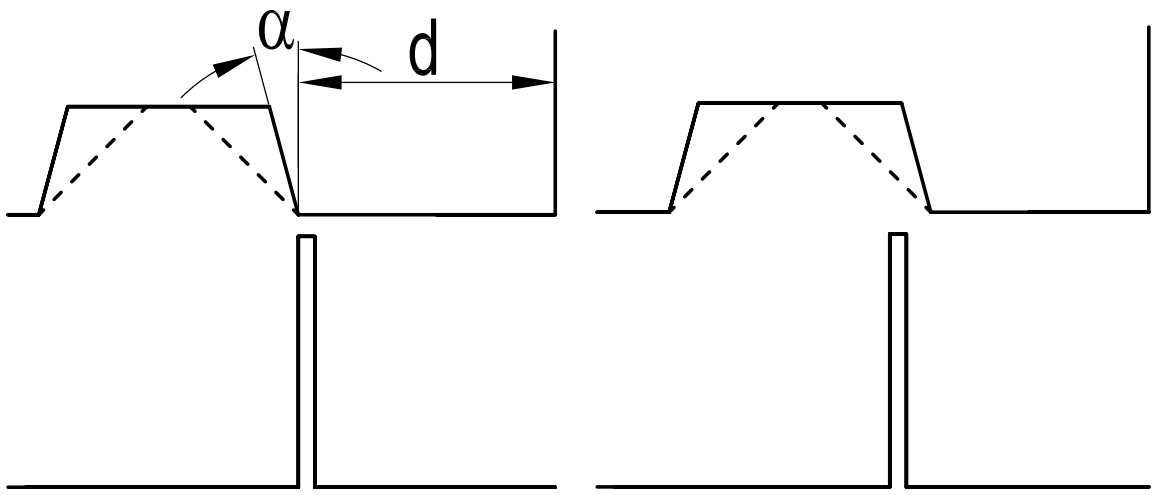

(a) Axial position 1, $d^* = 5.8 \times 10^{-3}$

(b) Axial position 2, $d^* = 4.9 \times 10^{-3}$

(c) Axial position 3, $d^* = 4.2 \times 10^{-3}$

(d) Axial position 4, $d^* = 2.7 \times 10^{-3}$

Fig. 47. The four axial positions of the right-hand rub-groove in Fig. 2 relative to the fixed labyrinth tooth position.

B. CFD Modeling

This investigation focuses on wheelspace cavity heating due to mainstream heat ingress. The simulated flow is steady-state, which avoids the computationally expensive and less important transient effects. The computational domain is chosen to be only a sector of, rather than the whole circumference of the wheelspace, which has 30 vanes in total. The circumferential coverage of the sector is 12^o, corresponding to the interval between two adjacent upstream stator vanes. To account for the circumferential repetition of the flow, cyclic boundary conditions are specified on the two section surfaces. The mainstream annulus in the computational domain starts axially from the trailing edge of the upstream nozzle guide vanes. The vanes themselves are not included in the domain, since the focus of the present investigation is the three-tooth labyrinth effect in the wheelspace region rather than the mainstream region. The nozzle guide vane effects by the flow are approximated as the potential perturbation, expressed by Eqs. 6.1 through 6.3.

$$v_r = 0 \tag{6.1}$$

$$v_\theta = \bar{v}_\theta - \frac{0.5\Delta p}{\rho(\bar{v}_\theta^2 + \bar{v}_z^2)^{\frac{1}{2}}} sin(N\theta + A)e^{-\frac{z_0 N}{r}} \tag{6.2}$$

$$v_z = \bar{v}_z - \frac{0.5\Delta p}{\rho(\bar{v}_\theta^2 + \bar{v}_z^2)^{\frac{1}{2}}} cos(N\theta + A)e^{-\frac{z_0 N}{r}} \tag{6.3}$$

This approximation was first proposed by Chew, et al [30], and later shown by Hills, et al [65] to perform reasonably well when compared to experiments and full three dimensional CFD solutions. The boundary conditions for the mainstream domain inlet are of the fixed mass type. The flow angle is specified as part of the

boundary conditions, while the magnitude and density of the flow will be determined by the flow solution. For the mainstream and two other inlets to be discussed, the entering turbulence is specified with an intensity of 0.1 a length scale of of 1 mm. The downstream rotating blades are also excluded from the domain. Their effects on the mainstream ingress and egress were found to be small by many researchers [37], [65], [42]. This would especially be the case for an extremely large gas turbine such as the present one, whose rotating blades reside at a relatively large distance downstream from the platform gap. A fixed pressure is specified as the mean value for the annulus downstream. The high velocity of the mainstream flow causes a thin mainstream boundary layer along the platform making the mainstream velocity profile radially fairly uniform away from the platform wall. Due to the much higher axial and circumferential velocities in the mainstream compared to that in the outer wheelspace cavity, only the radially inner portion of mainstream flow interacts with that from the wheelspace cavity. Thus only the inner half of the mainstream, from the platform to the middle of the mainstream, is included in the computation domain. Slip wall boundary conditions were therefore used on the outer boundary located at middle of the mainstream; the one-seventh power law is implemented on the platform for the mainstream inlet velocity boundary condition profile with the boundary layer thickness specified as 0.1 mm.

For the feed slot, the receiver holes and the inner labyrinth domain outlet, the desired static pressure boundary condition was attempted but gave no convergence. So alternatively, the fixed mass is specified for all three of these boundaries. However, only the mass flow rate of the receiver holes and inner labyrinth seal were known a priori, i.e. the mass flow rate for the feed slot is not known a priori. Based on the SiemensWestinghouse coolant system network flow model, the upstream pressure P_u, temperature T_u and downstream pressure P_d for the three-tooth labyrinth seal

are fairly constant, changing only by 2.6%, 0.0% and 0.37% within the range of working leakage conditions. Based on the values of fairly constant P_u, T_u and T_d, a two-dimensional flow model for the three-tooth labyrinth seals was used. The leakage through the three-tooth labyrinth was thus obtained, and subsequently used to determine the flow rate for the feed slot in the three-dimensional model.

C. Grid and Grid Independence Testing

In order to get improved grid resolution around the labyrinth teeth tips, which are very important in determining the leakage of the egress flow, a much denser grid is used at those regions. The density of the grid is controlled by stretching the grid. To obtain a better resolution for the middle cavity and outer cavity, the grid is refined in the circumferential direction in these two regions.

Figure 48 shows a meridional view of the grid around the three-tooth labyrinth seal. One can see the body-fitted hexahedra along the walls, with a varying thickness to meet the requirement for y^+. Another feature worth notice is the smooth transition between adjacent cells. On a $r - \theta$ plane of the entire domain, the volume ratio of the adjacent cells is controlled to be under 1.5, except for the triangular fillers along the walls. This criterion forbids any embedded refinement, whose size ratio is at least 2. This stringent grid quality requirement is necessitated by the challenging convergence difficulty. Numerous trial-and-error tests in the present study show that abrupt cell size variation easily leads to solution divergence. Even with this smooth grid variation implemented, convergence was still challenging. In order to converge to a solution on the finer grids, we firstly used a very small relaxation factor, such as 0.05, for the pressure. Iteration convergence is not as sensitive to the relaxation factors for the velocities, temperature, etc. as they are for the pressure. Therefore the

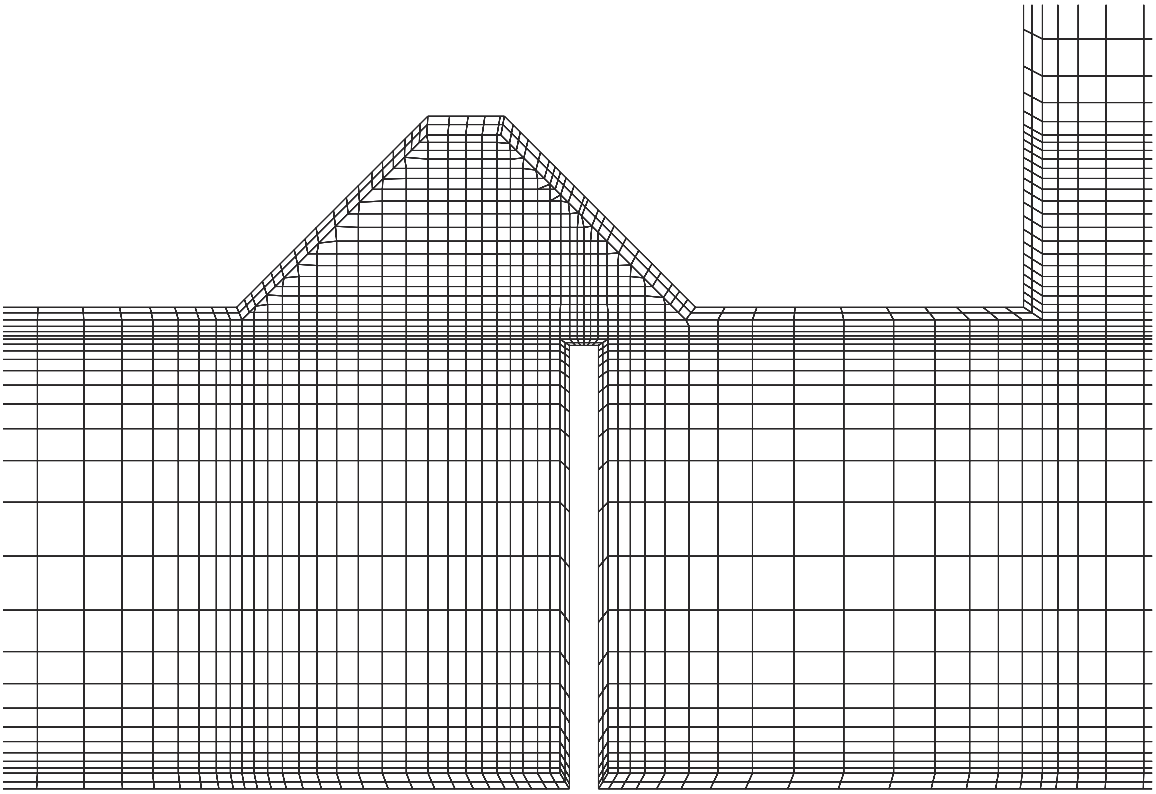

Fig. 48. Meridional view of the grid around the downstream tooth of the middle labyrinth seal in the wheelspace.

simulations herein specified 0.5 for the relaxation factors for velocities, temperature, etc. After all the normalized convergence residual errors reduced to a certain level, say 2.0×10^{-5}, a larger relaxation factor of 0.1 for the pressure was then used to accelerate the convergence. Once the convergence residuals decrease to certain values, the relaxation factors for all the variables are then increased to the default values. For example, the pressure at that stage had a relaxation factor of 0.3 and velocities of 0.7. This step was necessary to facilitate convergence. Many researchers encountered similar convergence difficulty in calculating wheelspace flow. To avoid this problem, they were usually forced to switch to simpler boundary conditions.

A grid independence test was conducted to obtain proper grids for the numerical

simulations in the present study. Except for the clearance and feed slot mass flow, which vary among specific cases, the computational domain and boundary conditions of the tested case are the same as that of production cases. The case considered has a pre-rub clearance c^* of 10 $\times 10^{-4}$. For grid independence evaluation purposes, the minimum and maximum temperatures of both the middle and outer cavities in the wheelspace are recorded. Then the relative difference between two consecutive grids is calculated. The relative difference is defined as the temperature difference between two consecutive grids divided by the temperature of the finer grid. The resulting grid independence assesment is shown in Table V. As one can see, three grids are shown with the number of cells ranging from 186,335 to 728,700. The intermediate grid is very close to the next finer grid in temperature, with a maximum difference of 0.77 percent and a minimum of -0.13 percent. Considering its accuracy and also the moderate number of cells, the intermediate grid was used for all production runs.

D. Results

1. Bulk Temperature

To gain overall insight into the temperature distribution, the dimensionless bulk temperature on various planes is plotted in Fig. 49 for rub-groove axial positions 1-4 and for rub-groove wall angles of 45^o and 15^o. The eight planes are radial or axial planes as shown in Fig. 46. The bulk temperature on the eight planes is obtained by taking the volume average of the temperature of the cells within these planes, both circumferentially and radially or axially. To obtain the dimensionless form shown on the vertical axis in Fig. 49, the bulk temperatures are then non-dimensionalized by

$$T^* = \frac{T - T_{fs}}{T_{ms} - T_{fs}}, \tag{6.4}$$

Table V. Grid independence testing for rim-cavity ingress heating.

No. of Cells		186,335	389,853	728,700
Outer Cavity	T^*_{min}	922.42	967.65	960.21
	$\frac{T^*_{min} - T^{*,f}_{min}}{T^{*,f}_{min}}$	-4.67%	0.77%	-
	T^*_{max}	1396.70	1404.24	1406.11
	$\frac{T^*_{max} - T^{*,f}_{max}}{T^{*,f}_{max}}$	-0.54%	-0.13%	-
Middle Cavity	T^*_{min}	742.21	745.67	743.94
	$\frac{T^*_{min} - T^{*,f}_{min}}{T^{*,f}_{min}}$	-0.46%	0.23%	-
	T^*_{max}	1122.55	1172.20	1168.48
	$\frac{T^*_{max} - T^{*,f}_{max}}{T^{*,f}_{max}}$	-4.24%	0.32%	-

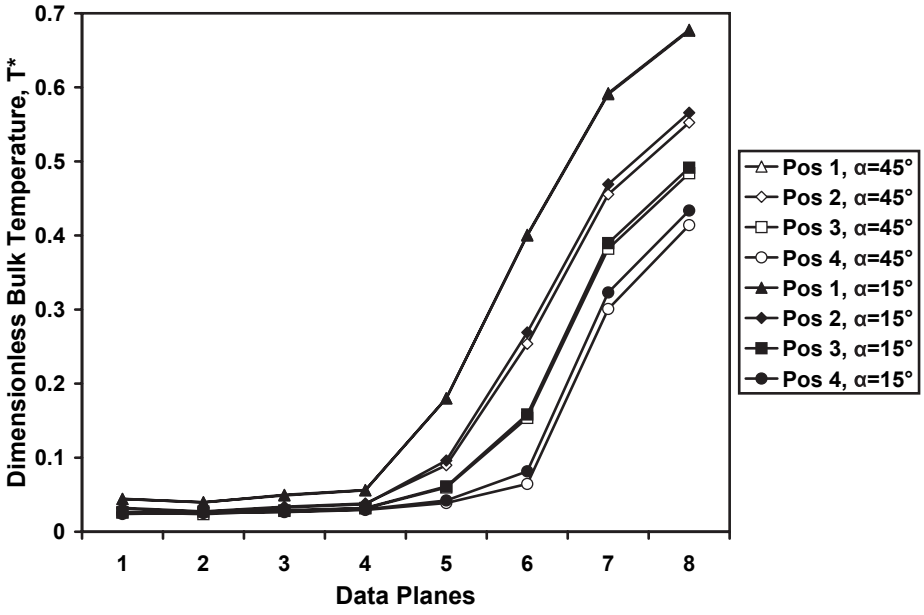

Fig. 49. Dimensionless bulk temperature averaged over $r-\theta$ or $\theta-z$ data planes as shown in Fig. 46 for rub-groove axial positions 1-4 and for rub-groove wall angles 45^o and 15^o.

where T_{fs} is the temperature specified at the feed slot and T_{ms} is that at the mainstream inlet. In the present study, the dimensionless feed slot temperature T^*_{fs} is 0 and the dimensionless mainstream temperature T^*_{ms} is 1.0.

As seen in Fig. 49, all cases of rub-groove axial position and wall angle remain fairly constant in temperature at planes 1 through 4, while increasing steadily as an observer approaches the mainstream for outer planes 5 through 8. One can also see that all cases are very close in temperature for middle cavity planes 1 through 4, while for outer cavity planes 5 through 8 the temperature varies. This temperature variation is obviously caused by the difference in seal configuration, specifically the rub-groove axial position and wall angle, of the three-tooth labyrinth seal. This finding is quite interesting when one considers that the outer cavity is far away from the three-tooth labyrinth seal studied. The three-tooth and the outer single-tooth

labyrinths are utilized to: (a) resist hot gas ingress from the mainstream and (b) keep the purge-coolant flow rate within acceptable limits. The uncertainty of the actual rub-groove axial position and wall angle at steady state give uncertainty of the seal effective clearance (Fig. 47) and thus uncertainty of purge-coolant leakage. It was found that the presence of the outer labyrinth seal, with purge-coolant passing through it, prevents most of the ingested heating from the mainstream from entering the middle cavity. This makes the temperature in the middle cavity very close to that of the purge-coolant flow regardless of rub-groove axial position and wall angle.

To further illustrate the effects of rub-groove tooth position and wall angle, the dimensionless bulk temperature on planes 5 through 8 is plotted against rub-groove axial position in Fig. 50.

It is shown that for both rub-groove wall angles $\alpha = 15^o$ and $\alpha = 45^o$ the bulk temperature for data planes 5 through 8 decreases for rub-groove axial positions nearer the rotor (see Figs. 2 and 46). The highest temperature was found when the rub-grooves are at position 1, and the lowest at position 4. The dimensionless temperature at position 1 is higher than that at position 4 by 0.14, 0.32, 0.27 and 0.24 for wall angle $\alpha = 15^o$ at positions 5, 6, 7 and 8, respectively, and by 0.14, 0.34, 0.29 and 0.26 for $\alpha = 45^o$. Also the rub-groove wall angle plays a role in the temperature distribution. At planes 6, 7 and 8, the temperature for $\alpha = 15^o$ is shown to be about 0.01 - 0.02 higher than that for $\alpha = 45^o$ at positions 2, 3 and 4. Since the variation in rub-groove axial position and wall angle changes the minimum distance after-rub clearance, one sees how the bulk temperature is determined by the after-rub clearance.

Figure 51 shows the after-rub clearance for all the cases. One can see by examining Figs. 50 and 51 jointly, the relationship between the minimum distance after-rub clearance, seal leakage and wheelspace bulk temperature. For a fixed wall angle of

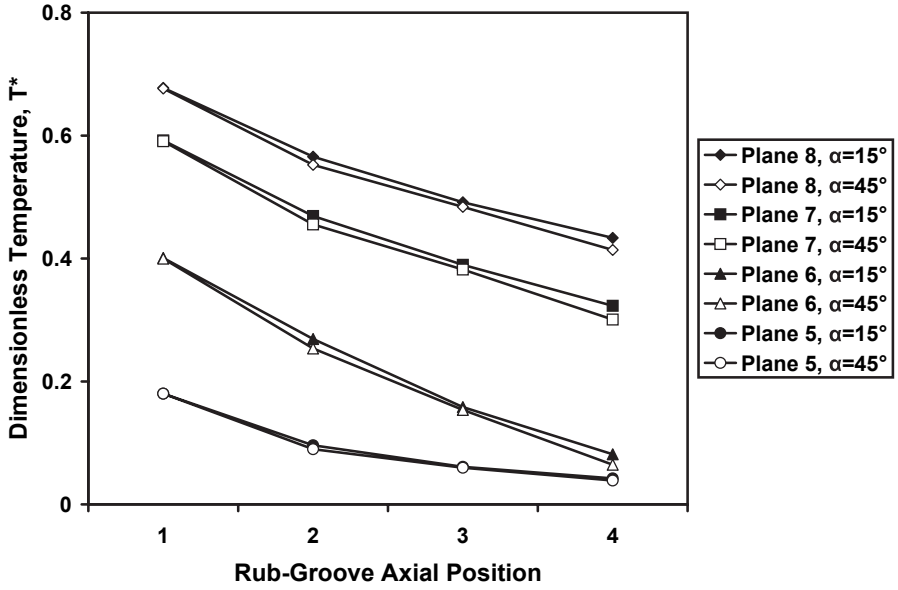

Fig. 50. Dimensionless bulk temperature averaged over various data planes for rub–grooves with different axial positions and wall angles.

either $\alpha = 15^o$ or $\alpha = 45^o$, the bulk temperature is inversely proportional to the after-rub clearance. For example, the rub-groove at position 1 has the minimum after-rub clearance as shown in Fig. 51 and the highest bulk temperature as shown in Fig. 50. For a fixed axial position, however, the larger clearance for $\alpha = 15^o$ leads to a slightly higher bulk temperature. For example, at axial positions 2, 3 and 4, the wall angle $\alpha = 15^o$ has a larger after-rub clearance than that of $\alpha = 45^o$ (see Fig. 47), but the temperature of the former angle is higher than that of the latter (see Fig. 50). This difference is attributed to different purging and cooling effects from the influence of α on the secondary flow trajectory. To gain an enhanced understanding on how the rub-groove axial position and wall angle affect the temperature in the wheelspace, one needs to review the interaction between the mainstream annulus flow and the purge-coolant secondary flow.

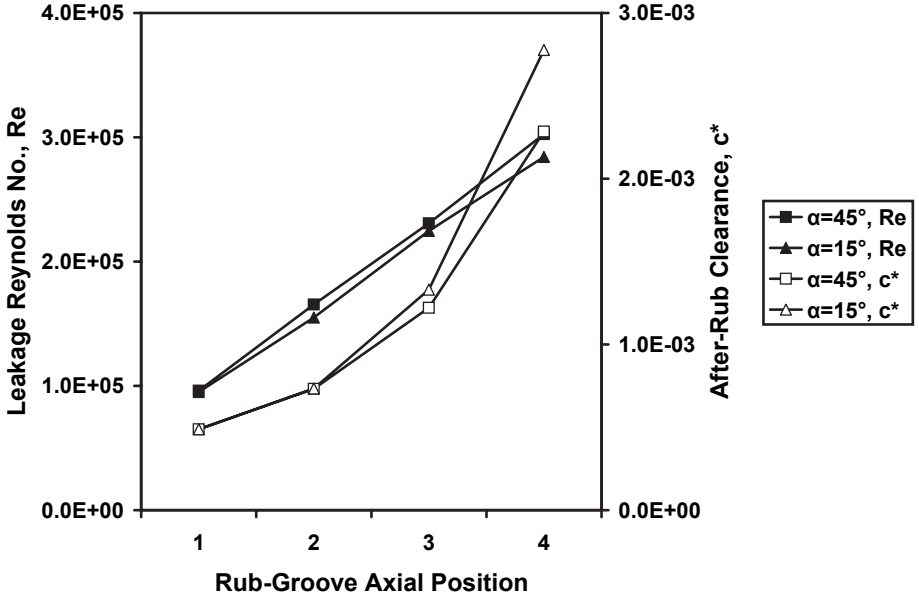

Fig. 51. Leakage Reynolds number vs. dimensionless after-rub minimum clearance for various axial positions and wall angles.

The mainstream annulus flow tends to raise the temperature in the wheelspace primary through hot gas ingress, as well as turbulent thermal diffusion from the mainstream to the outer cavity. This gas ingress is due largely to mainstream pressure variation and disk pumping. Compared to hot gas ingress, turbulent thermal diffusion is relatively weak. The purge-coolant flow is intended to lower the wheelspace temperature by suppressing the hot gas ingress and by mixing with the hot ingress to cool the wheelspace fluid. As a result, the temperature in the wheelspace is determined by the counteraction between the mainstream ingress and the purge-coolant flow. So the differential bulk temperature in Fig. 50 is ultimately influenced by the leakage of the three-tooth labyrinth seal. Comparison of Figs. 50 and Fig. 51 shows the close relationship between secondary flow leakage and the bulk temperature.

Figure 51 gives, apart from the dimensionless after-rub clearance, the seal leakage Reynolds number for rub-grooves of any axial position and wall angle. The leakage

Reynolds number in Fig. 51 is defined as

$$Re = \frac{2\dot{m}}{\pi \mu D} \tag{6.5}$$

where $\dot{m}$ is the leakage through the middle labyrinth seal, and D is the seal diameter. Comparison of Figs. 50 and Fig. 51 reveals that a higher temperature, for all rub-groove positions and wall angles, always corresponds to a lower leakage. For example, the labyrinth seal at axial position 1 with wall angle of 15^o gives the highest bulk temperature in Fig. 50 and the lowest leakage as shown in Fig. 51. The relationship between the leakage and the bulk temperature demonstrates that a stronger leakage of purge-coolant flow generally gives a lower temperature in the wheelspace. The more leakage the purge-coolant flow has, the more effective it is in suppressing the hot gas ingress and turbulent thermal diffusion from the mainstream.

2. Flow Pattern

Xu, et al. [19] studied the effect of rub-groove wall angle and tooth axial position on the leakage. The dimensions and boundary conditions they used, conversely, are typically for aircraft engines. It was found that the leakage jet flow downstream of the clearance can have different flow patterns. Specifically, the jet may exit the clearance horizontally, vertically or with a certain sloping angle, depending on the combination of the wall angle and the tooth axial position. For the very large industrial engine under present study, a significant flow pattern variation is also found. The purge-coolant flow exits the middle labyrinth to enter the middle cavity over the third tooth with a varying angle. For example, the jet flow over the third tooth is horizontal when rub-groove is at axial position 1 (Fig. 52 (a)), while the jet is directed at about 45 degrees from horizontal when it is at position 4(Fig. 52 (b)). The flow

patterns shown in Fig. 52 have the rub-groove angle of $\alpha = 15^o$. However for both $\alpha = 15^o$ and $\alpha = 45^o$ the flow pattern is quite similar when the rub-groove is at the same axial position. For the situation considered here, the variation in jet flow angle, accompanied significant geometry and leakage rate changes which substantially affected only the outer cavity. This is due to the fact that the temperature in the middle cavity is quite uniform and close to that of the jet flow.

The vectors in both Fig. 52 (a) and Fig. 52 (b) are drawn to the same scale. As one can see, the magnitude of the vectors varies drastically from position 1 to 4. The vectors for position 4 are two or three times as large as that of position 1 in most places, corresponding to a much larger purge-coolant flow rate for position 4.

3. Circumferential Temperature Variation

By averaging temperature on a data plane, as done in Fig. 49 and Fig. 50, one gets an overall picture of the temperature distribution in the wheelspace. But the averaging cancels out the temperature variation on the data plane. To elucidate the circumferential temperature asymmetry, the temperature was averaged radially on plane 5 and axially on planes 6 and 8, as shown in Figure 53. The temperature on plane 7 is very similar to that on plane 8, and hence it is not shown. On planes 1 through 4, the temperature is found to be fairly uniform circumferentially, so they are not included.

On plane 8 at the outer edge of the platform gap all rub-groove axial positions demonstrate a strong circumferential variation of temperature. On plane 6 at the inner edge of the platform gap the temperature variation for rub-grooves at axial positions 1 and 2 are still quite strong, but for rub-groove position 4 the circumferential temperature is fairly uniform. On plane 5 all cases have approached circumferential uniformity in temperature, except for the two rub-groove shapes at axial position 1.

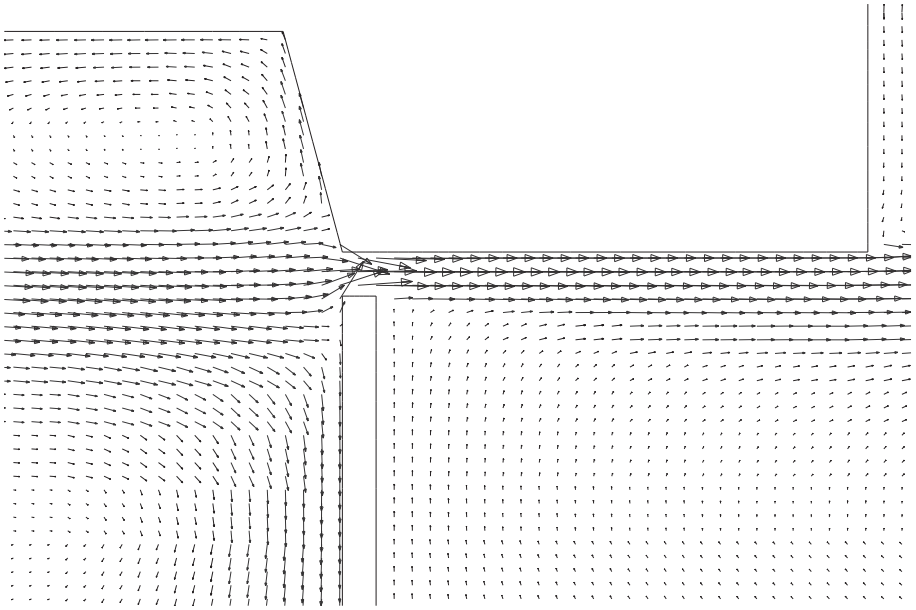

(a) Position 1, $\alpha = 15^o$

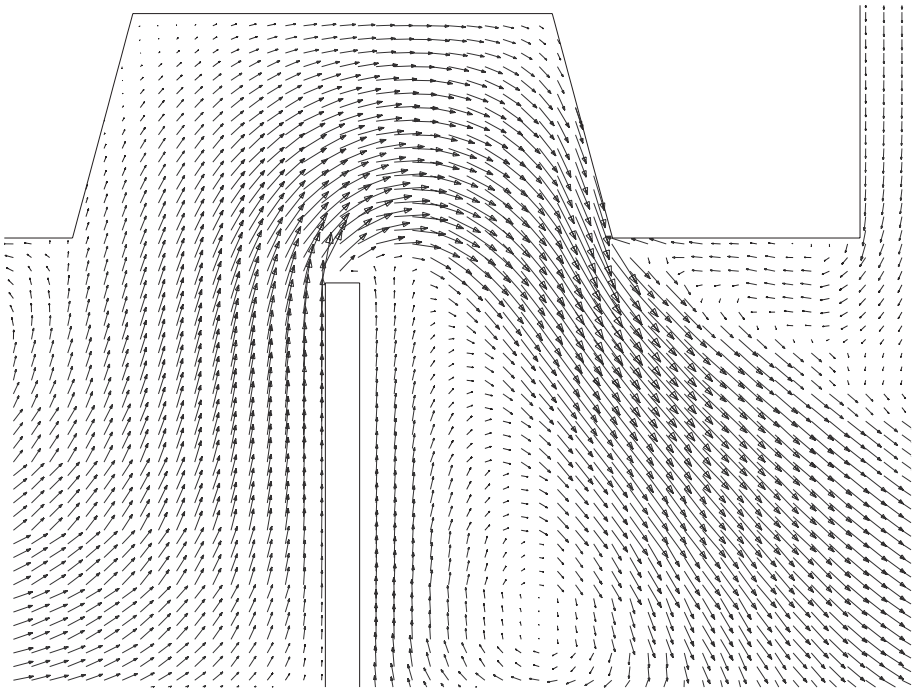

(b) Position 4, $\alpha = 15^o$

Fig. 52. Flow pattern around the downstream tooth of the middle labyrinth seal, varying depending on the rub-groove wall angle and axial position.

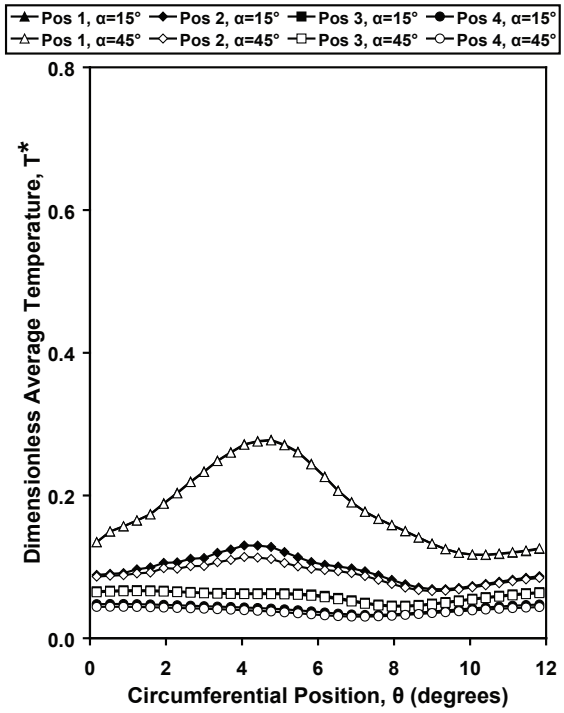

(a) Plane 5, radially averaged

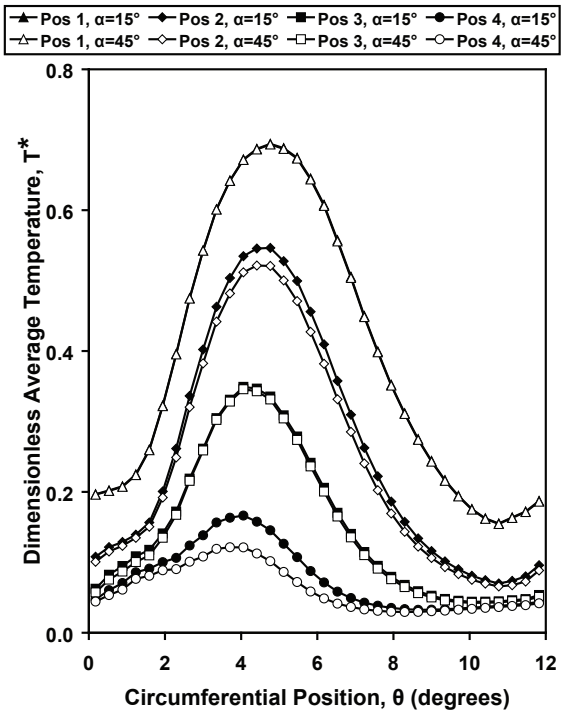

(b) Plane 6, axially averaged

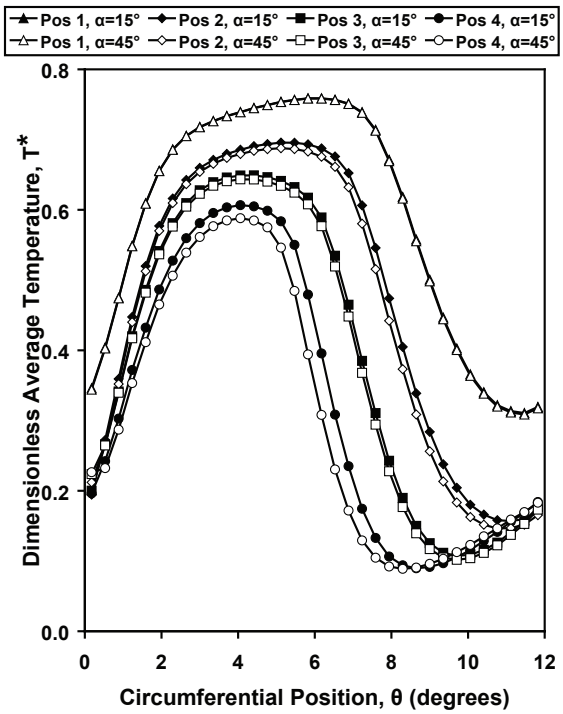

(c) Plane 8, axially averaged

Fig. 53. Circumferential variation of average temperature on various planes as labeled in Fig. 46.

In general, the temperature variation is two-fold: the magnitude of the peak and the valley, and the shape and location of the peak and the valley. For example, for rub-groove axial position 1 on plane 8 with wall angles of $\alpha = 15^o$ and $\alpha = 45^o$, the peak temperature has a value of as high as 0.76, and the valley has 0.3. Further, the peak temperature is quite flat for both wall angles, with the valley occuring at 11.1^o. The rub-groove at axial position 4 with wall angle of $\alpha = 45^o$, has a non-flat peak temperature of 0.59 and a valley of 0.09. In addition, the valley occurs at $\theta = 9^o$. Interestingly, all the rub-groove axial positions and wall angles, except those at position 1, are very close in temperature in the ranges of $\theta = 0.0^o - 1.0^o$ and $\theta = 10.5^o - 12.0^o$. A similar overall temperature variation can be seen on plane 6, however, the variation is much more intense there. For example, the rub-groove at position 1 has a temperature peak and valley of 0.70 and 0.16, respectively. The rub-groove at position 4 with wall angle $\alpha = 45^o$ has a peak and valley as low as 0.12 and 0.02. That is, even the temperature peak of the latter is lower than the valley of the former. In other words, the plane 6 temperature is the most sensitive to rub-groove axial position and wall angle. This large circumferential variation in temperature will cause the materials used to manufacture the stator parts to vary circumferentially in metallurgical property. When rub-groove positions such as position 1 occur, a significant decrease in material strength occurs, especially in the portion where the temperature reaches the peak.

This temperature circumferential asymmetry is known to be caused by the main-stream pressure asymmetry that gives the asymmetrical ingress into the outer cavity. As was mentioned earlier, the pressure asymmetry is due to the locally high pressure wake of the upstream nozzle guide vanes. To demonstrate how the rub-groove wall angle and axial position affect the pressure asymmetry in the wheelspace, Fig. 54 shows the pressure contours for the two rub-grooves with wall angle $\alpha = 45^o$, one at

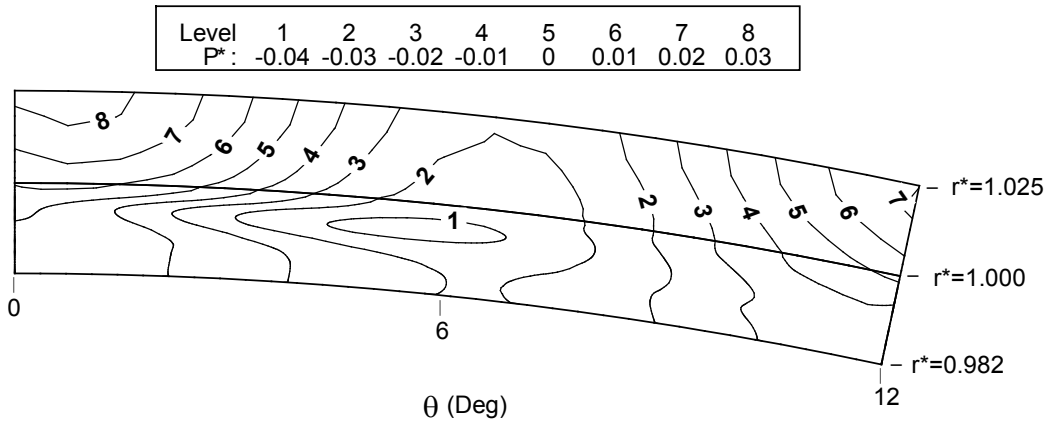

(a) Axial position 1

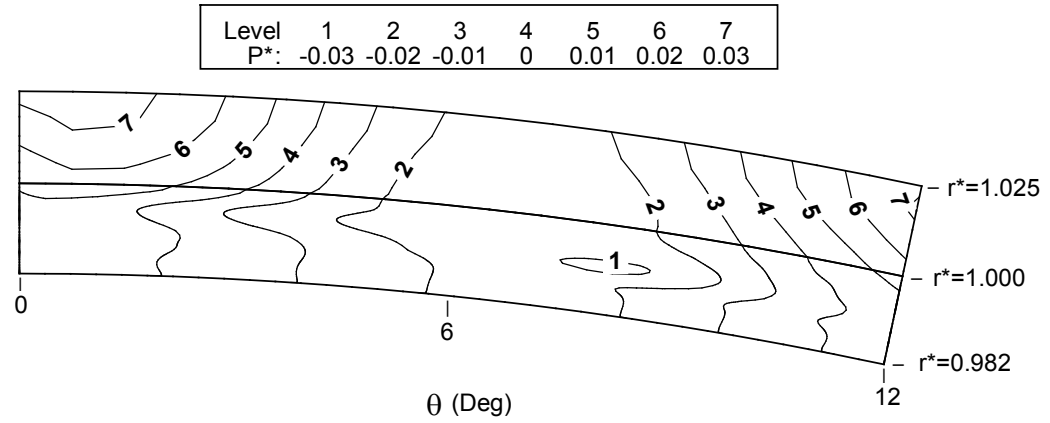

(b) Axial position 4

Fig. 54. Pressure contours on a $r - \theta$ plane labeled as 0 in Fig. 46 for rub–groove positions 1 and 4 with wall angle $\alpha = 45^o$.

axial poison 1 and the other at axial position 4. The contours are taken from the plane labeled as 0 in Fig. 46. The pressure in Fig. 54 is non-dimensionalized by the mainstream outlet pressure. The intermediate horizontal-like line in Figs. 54 (a) and (b) represents the radially outer surface of the NGV platform. In both figures a pressure peak appears at $\theta = 1^o$, and a valley roughly at $\theta = 6^o$ corresponding to the high-pressure and low velocity wakes behind the NGVs located at $\theta = 0^o$ and $\theta = 12^o$. For rub-groove position 4, the pressure valley shifts to the right compared to that at position 1. While the pressure peak for the two rub-groove positions is very close in magnitude, the pressure valley for position 1 is slightly lower than that for position 4.

Corresponding to Fig. 54, Fig. 55 gives the velocity vector distributions. As one can see, for both rub-groove axial positions 1 and 4, the circumferential velocity is much larger than the radial velocity. In the mainstream annulus (above the intermediate horizontal-like line), the radial velocity is close to zero, and the velocity distributions are quite similar. Inside the outer rim-cavity (below the intermediate horizonatal-like line), the velocity magnitude for rub-groove axial position 1 is generally larger than that for rub-groove axial position 4, irrespective of the radial and circumferential positions. One can also see that for rub-groove axial position 1, there is a fairly large circumferential velocity peak at the radially middle plane of the rim-cavity approximately from $\theta = 2^o$ to $\theta = 8^o$. But for rub-groove axial position 4, a similar circumferential velocity peak of much smaller magnitude occurs between $\theta = 3^o$ and $\theta = 7^o$.

While the velocity distributions shown in 55 show moderate difference on $r - \theta$ plane for rub-groove positions 1 and 4 with wall angle of $\alpha = 45^o$, the velocity vector plots in Figs. 56 and 57 illustrate more significant differences in $r - z$ plane for these flows. The vector plots are taken for circumferential planes of $\theta = 1^o$ and $\theta = 6^o$.

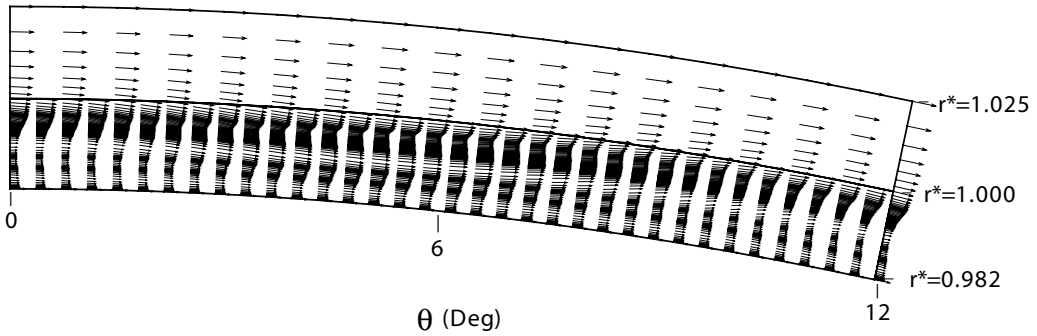

(a) Axial position 1

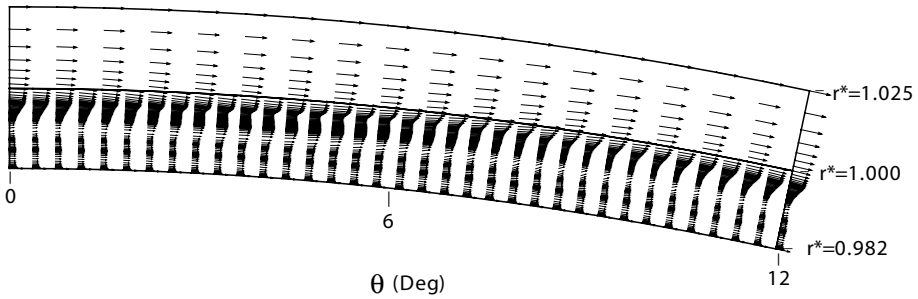

(b) Axial position 4

Fig. 55. Velocity vectors on a $r-\theta$ plane labeled as 0 in Fig. 46 for rub-groove positions 1 and 4 with wall angle $\alpha = 45^o$.

The circumferential planes $\theta = 1^o$ and $\theta = 6^o$ contain the pressure peak and valley, respectively, seen for this rub-groove situation in Fig. 54 that result from the high-pressure NGV wake regions at $\theta = 0^o$ and $\theta = 12^o$. Notice that at $\theta = 1^o$ positions 1 and 4 have appreciable hot gas ingress due to the locally high mainstream pressure. Notice further that, because the rub-groove at axial position 1 gives a small purge-coolant flow, outer cavity hot gas passes through the single-tooth labyrinth toward the middle cavity at $\theta = 1^o$ (Fig. 56(a)). However, the higher purge-coolant for rub-groove axial position 4 causes no outer cavity gas to exit the outer cavity on the $\theta = 1^o$ plane. This explains why rub-groove axial position 1 has a higer T^* on the $\theta = 1^o$ plane in Fig. 53(c) than do the other axial positions. For position 1 there is also a very strong vortex at the outer rim of the wheelspace. For position 4, there is also a vortex at the outer rim of the wheelspace, but it is much weaker and smaller due to the purge effect of the outer cavity.

Comparison of the flow patterns on the plane $\theta = 6^o$ in Fig. 57 also shows significant differences between rub-grooves at axial positions 1 and 4. This is because the mainstream axial and circumferential velocities near the platform are highest near $\theta = 6^o$ because of the low velocity wake behind the NGVs near $\theta = 0^o$ and $\theta = 12^o$. On this plane the rub-groove at position 1 has a very strong vortex at the outer rim of the wheelspace due to the locally high mainstream velocity. While the vortex draws some hot gas from the mainstream into the outer cavity, there is a substantial amount of coolant blowing through the outer labyrinth seal into the mainstream. The rub-groove at position 4 in Fig. 57(b) on the $\theta = 6^o$ plane has no vortex at the outer rim of the wheelspace. The flow field shows a very strong purge-coolant flow through the outer labyrinth seal, strongly expelling the hot gas and preventing the existence of a vortex. The comparison above shows that the middle labyrinth seal with rub-groove at position 4 and wall angle $\alpha = 45^o$ is much more effective in suppressing

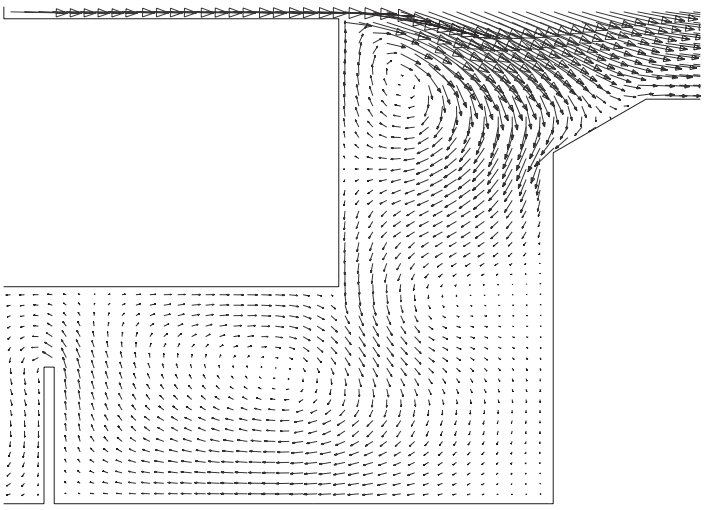

(a) Axial position 1, $\theta = 1^o$

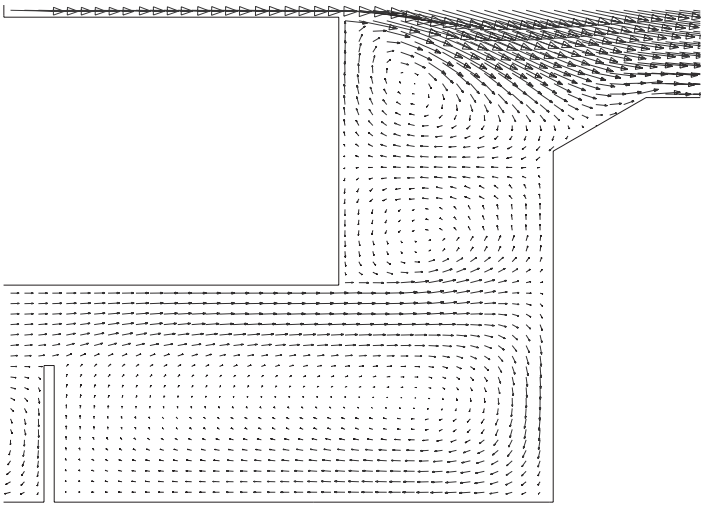

(b) Axial position 4, $\theta = 1^o$

Fig. 56. Velocity vector plots on r-z coordinate planes for rub-grooves at axial positions 1 and 4 with wall angle $\alpha = 45^o$ and $\theta = 1^o$.

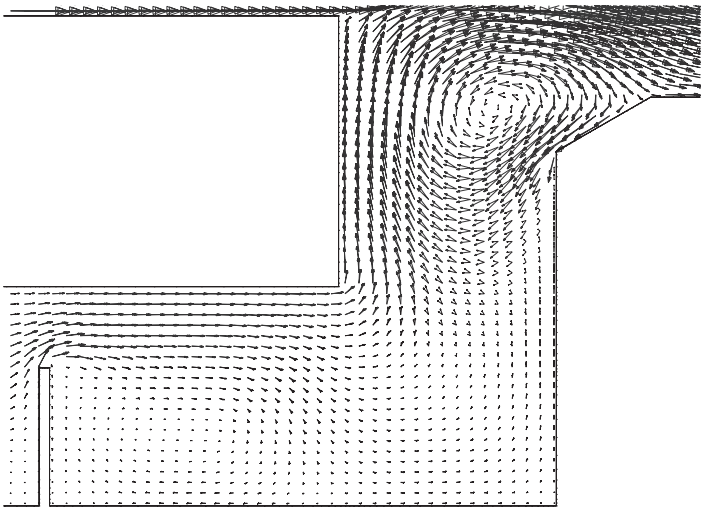

(a) Axial position 1, $\theta = 6^o$

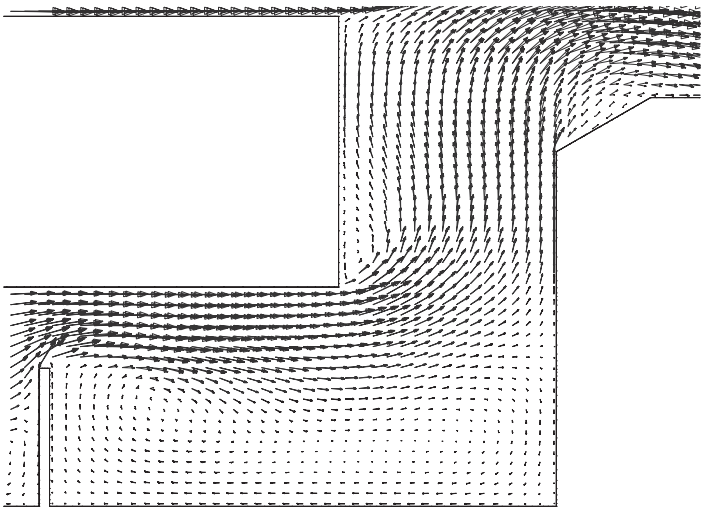

(b) Axial Position 4, $\theta = 6^o$

Fig. 57. Velocity vector plots on r-z coordinate planes for rub-grooves at axial positions 1 and 4 with wall angle $\alpha = 45^o$ and $\theta = 6^o$.

the hot gas ingress than that at position 1 with the same wall angle. However, more purge-coolant flow must be sacrificed to accomplish this.

It is interesting that the circumferential pressure appears to be "out of phase" with the temperature field. Specifically, at circumferential position about $\theta = 1^0$, there is a pressure peak (ref Fig. 54), which drives the hot gas into the outer cavity (ref. Fig. 56). Consequently there should be a temperature peak at this circumferential position. However, the temperature distribution in Fig. 53 shows that for all cases the temperature peak occurs at $\theta = 3^0 - 6^0$, rather than at $\theta = 1^0$. Similarly, at about $\theta = 6^0$ there is a pressure valley (Fig. 54) together with the strongest gas egress, but it is not until about $\theta = 8^0 - 11^o$ that the temperature reaches its valley (ref. Fig. 57). As one can see, there appears to be a considerable phase lag between temperature and pressure. This paradox, however, is caused by the strong circumferential velocity. For example, at $\theta = 1^0$ the pressure peak starts to push the hot gas from the mainstream into the outer cavity, but when the hot gas finally reaches the radially inner boundary of the outer cavity its circumferential position is about $\theta = 4^0$ or more. A similar circumferential convection occurs for the expunging purge-coolant flow.

4. Axial and Radial Temperature Variation

While the bulk fluid temperature and its variations are of great interest to turbine engineers, the temperature on the wheelspace walls is often the greatest interest. The temperature for rub groove axial positions 1-4 and wall angle of $\alpha = 15^o$ are plotted in Fig. 58 for the case of the outer single-tooth labyrinth having the tooth-on-rotor (TOR) and the tooth-on-stator (TOS) style. The data planes chosen to be plotted are planes 5, 6 and 8. The horizontal axis in Fig. 58(a) represents the relative radial position from the rotor to the stator, while the horizontal axes in Fig. 58(b)-(c)

represent the relative axial position from the stator to the rotor. The temperature is circumferentially averaged based on cell volumes. Because the configuration (TOR vs. TOS) of the outer labyrinth seal significantly influences the wall temperature of the outer cavity, both configurations are included in Fig. 58. The cases that have been plotted in Figs. 49 through 57 were the TOR configuration shown in Fig. 46.

As one can see in Fig. 58, for both tooth on the rotor and tooth on the stator the circumferentially averaged temperature varies significantly with rub-groove axial position on both the stator and the rotor walls at all planes in Fig. 58. The fluid temperature variation with rub-groove axial position is especially large near the rotor compared to the stator on planes 6 and 8. For example, the dimensionless fluid temperature in Fig. 58 decreases about 0.41 near the rotor wall for rub-groove axial positions 1 to 4, while only about 0.18 near the stator. On plane 5 the temperature variation due to rub-groove axial position is comparable near the rotor and near the stator.

While comparable in terms of fluid wall temperature variation, placing the tooth on the rotor or on the stator makes a significant temperature difference. Specifically, locating the tooth on the rotor gives a higher temperature near the rotor wall than near the stator wall for all the rub-groove positions. The temperature near the rotor wall is especially higher on planes 6 and 8 for rub-groove positions 1 through 3. For example with the rub-grooves at position 1, the dimensionless temperature near the rotor is 0.28 higher than that near the stator on plane 6, and 0.24 higher on plane 8.

To prevent overheating, the turbine disc temperature should be kept below a certain limit of temperature, depending on the specific materials used. However, for the sake of efficiency, i.e. minimum purge-coolant flow being sacrificed, the temperature is usually as high as the material can safely tolerate. Thus it is desirable that both the stator and the rotor are close in temperature. Further, the centrifugal force

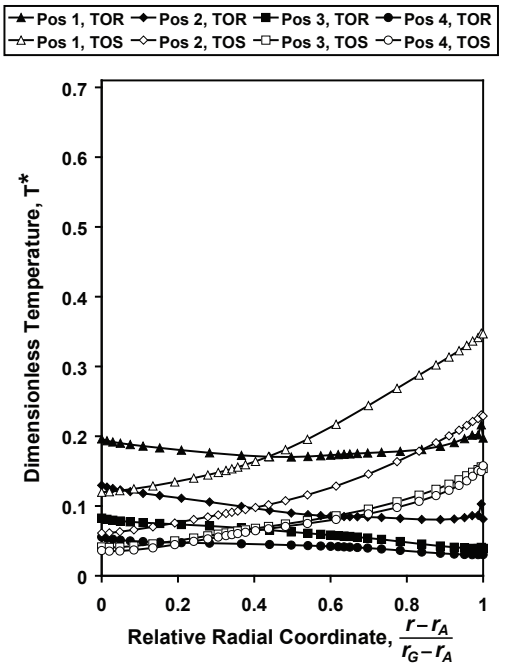

(a) Plane 5, Radial variation

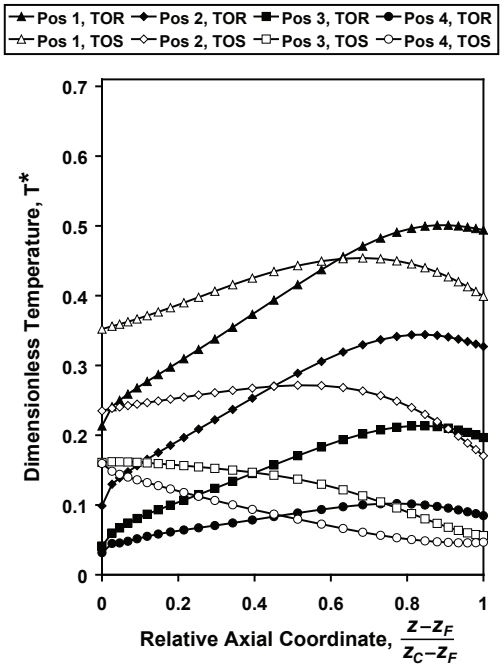

(b) Plane 6, Axial variation

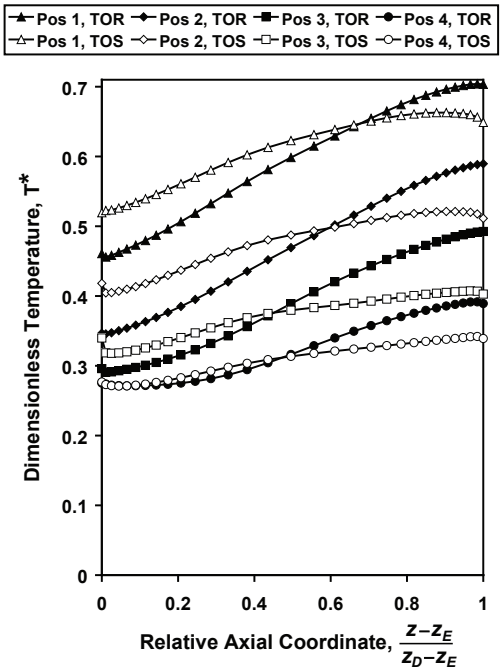

(c) Plane 8, Axial variation

Fig. 58. Radial or axial temperature variation on various planes as marked in Fig. 46.

of the the rotor causes it to require more thermal reliability than the stator, especially regarding attachments to the rotor. This is especially the case for the outer portion of the wheelspace, such as locations on planes 6 and 8 where the temperature approaches the extremity the material can endure.

To mitigate the higher temperature on the rotor for the TOR design, it is preferred to use the TOS design. TOS brings down the temperature on the rotor, making it closer to that on the stator as shown in Figs. 58(b) and 58(c). For example, compared to TOR, TOS reduces the dimensionless rotor temperature by 0.09 for position 3 on plane 8 while it reduces it by 0.25 for the same position on plane 6. In other words, for a rotor material with a certain temperature limit, the temperature can be raised by 0.09 with rub-grooves at position 3, if the TOS design is used in place of the TOR design.

E. Summary

The present work numerically investigates the effect of rub-groove axial position and wall angle of the three-tooth labyrinth seal on wheelspace heating due to hot gas ingress. It was found that while the effect of rub-groove wall angle on ingress heating is mild, the effect of rub-groove axial position is substantial. The influence of rub-groove axial position on wheelspace heating is examined by analyzing the interesting variations of the circumferential temperature distribution, axial temperature distribution, pressure field, etc.

The three-tooth labyrinth seal studied herein is located slightly inward of the middle cavity of the turbine wheelspace, which is divided into inner, middle and outer cavities. Two different rub-groove wall angles, $\alpha = 15^o$ and $\alpha = 45^o$, are studied along with rub-groove axial positions 1 through 4 with d^* of 5.8×10^{-3}, 4.9×10^{-3} 4.2×10^{-3}

and 2.7×10^{-3}, respectively. For the cases considered here, the effects of labyrinth seal rub-groove axial position and wall angle are summarized as follows:

1. Both the rub-groove wall angle and axial position have an effect on the flow pattern, temperature and pressure field of the outer wheelspace cavity, only a slight effect on the middle cavity. Specifically, for the outer cavity, the flow, temperature and pressure fields are substantially affected by the rub-groove axial position and mildly effected by the rub-groove wall angle, depending on the rub-groove axial position.

2. The bulk temperature in the outer cavity decreases with increasing rub-groove axial position number, i.e. decreasing d^*, for a fixed rub-groove wall angle. Specifically, from rub-groove axial position 1 to 4, the dimensionless bulk temperature decreases by 0.14, 0.34, 0.29 and 0.26 for wall angle $\alpha = 45^o$ on planes 5, 6, 7 and 8 respectively, and by 0.14, 0.32, 0.27 and 0.24 with $\alpha = 15^o$. Of the two rub-groove wall angles, the wall angle of $\alpha = 15^o$ gives a slightly higher bulk temperature than does $\alpha = 45^o$ for rub-groove positions 2, 3 and 4 on planes 6, 7 and 8, while both angles give almost the same temperature for position 1. For example, the wall angle $\alpha = 15^o$ gives a slightly higher temperature than that of $\alpha = 45^o$ by about 0.02 for rub-groove axial position 4 on planes 6, 7 and 8, while almost the same on plane 5.

3. The bulk temperature is ultimately determined by the purge-coolant flow entering through the middle labyrinth seal to the wheelspace. Because the pressure drop across the labyrinth seal is fixed, purge-coolant flow rate is determined by the rub-groove wall angle and axial position. The more purge-coolant flow allowed by a particular rub-groove wall angle and axial position, the lower the bulk temperature in the outer wheelspace cavity.

4. The rub-groove axial position (and somewhat the wall angle) significantly alter the circumferential temperature distribution in the outer cavity. The magnitude as well as the shape of the circumferential temperature distribution is affected. On plane 8 for example, the dimensionless bulk temperature decreases by about 0.15 from rub-groove positions 1 to 4 at most of the circumferential data planes with the temperature valley shifting from about 8.5^o to 11.5^o. On plane 6, the circumferential peak of dimensionless temperature for position 1 is about 7 times that of position 4, with the former being about 0.7 and the latter 0.1.

5. The rub-groove axial position also affects the axial temperature distribution on planes 6 through 8. It generally shows a higher temperature and more temperature variation with rub-groove position near the stator than near the rotor. The variation is also substantially influenced by whether the outer single-tooth labyrinth is tooth-on-rotor (TOR) or tooth-on-stator (TOS). Compared to TOR, TOS tends to reduce the higher temperature near the rotor and to increase that near the stator, thus giving a more uniform axial distribution for data planes 6 through 8 for example.

CHAPTER VII

GRID GENERATOR DEVELOPMENT

A. Features of OpenCFD Grid

Figure 59 gives two samples of two-dimensional grids produced by OpenCFD. As one can see, the grids have a number of features that are well suited for the flow involving a labyrinth seal.

1. Cartesian Cells Dominated

As is well known, Cartesian grids are the grids of choice due to their exceeding performance in accuracy and convergence. This is especially true for flow involving labyrinth seals where abrupt pressure and velocity changes occur across the labyrinth teeth. To handle these abrupt changes, the grid around the tooth needs to have very good quality. Otherwise, the convergence and accuracy of the solution will be jeopardized. But purely Cartesian grids are hard to generate for a realistically complicated geometry. Either the algorithm is hard to maintain robust or the grid is easily twisted due to small local geometrical disturbances from the domain. So OpenCFD is aimed toward generating hybrid grids, with the majority of cells being Cartesian or quadrilateral as shown in Fig. 59.

2. Small Details Preserved

For the labyrinth seal type of flow, regions surrounding the labyrinth teeth are very important and require a high-quality grid to accurately resolve the flow. And the size of the tooth tip and clearance which are vital to the flow are usually very small, i.e. typically 1/10 to 1/100 of that of the whole domain. To simulate a worn labyrinth

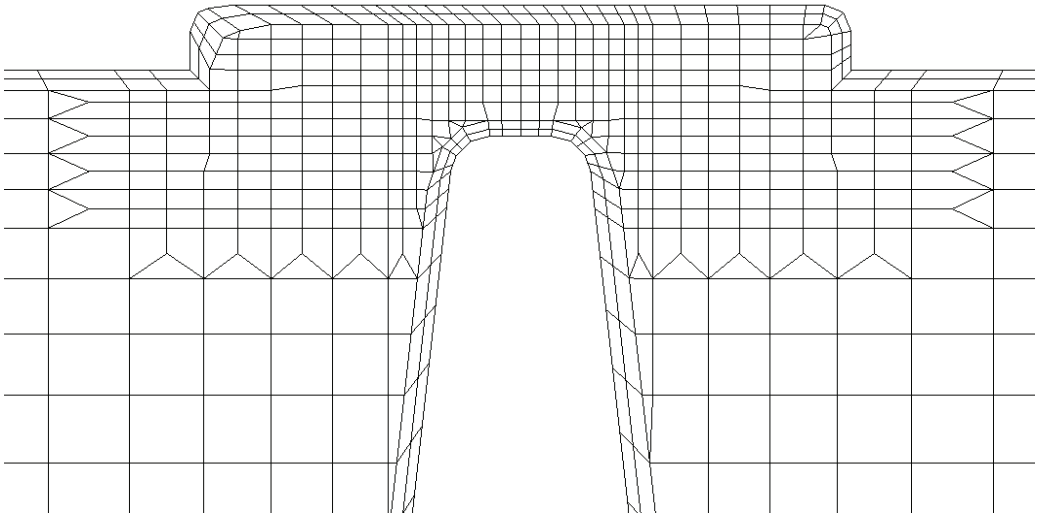

(a) Grid showing geometry preservation and varying extrusion layer thickness

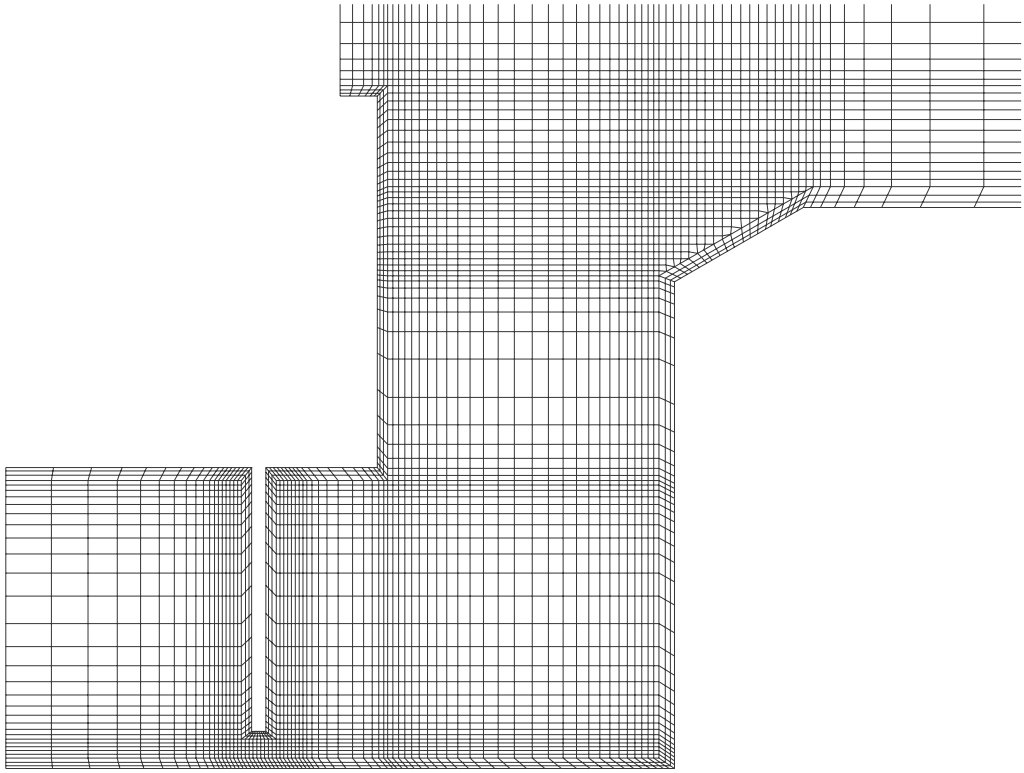

(b) Rim Cavity

Fig. 59. Sample two-dimensional grids generated by OpenCFD.

tooth, even smaller details are involved at the tooth tip, with lengths as small as 1/100 to 1/1000 of the whole domain. These small details impose great challenges to many grid generators which tend to smooth them out or produce ill-shaped cells in those regions.

OpenCFD utilizes cell cutting and cell removal to cut out the grid from a background grid. This strategy enables OpenCFD to preserve all the small details of the geometry. Figure 59 (a) shows a grid for a labyrinth seal with a worn tooth near the rub-groove. One can see that the roundness of the worn tooth tip and the two upper corners of the rub-groove are reasonably captured. More details on the methodology can be found in Section C.

3. Extrusion Layer along the Wall

For turbulent flow, the grid along the walls usually has special requirements in order to resolve the abrupt near-wall variation there correctly. In the present research, the high-Re $k-\epsilon$ model is used in regions away from the walls and the wall function used for regions near a wall. To ensure the accuracy of the wall function, y^+ for the near-wall cells must lie in a reasonable range, such as from 12 to 200 or preferably from 12 to 150. This requires that the cells on the wall have a reasonable thickness in the direction perpendicular to the wall. For labyrinth seal types of flow, the flow field along the wall varies significantly along the wall, and it may sometimes require a varying thickness for the wall cells. Furthermore, coefficients such as the wall shear stress and heat transfer coefficient, can involve two or more layers of cells near the wall. To accurately predict these coefficients, well shaped and properly layered cells are required along the wall.

With the above considerations OpenCFD generates one or more layers of quadrilateral cells along the wall, as shown in Fig. 59. Figure 59 (a) shows a magnified view

of the grid around the tooth tip. As one can see, the cells along the walls are reasonably well structured and properly layered. In some literature, these layers of cells are referred to as extrusion layers, with each layer being named a sublayer. OpenCFD allows the user to specify the number of layers and the thickness of each sublayer. If needed, the thickness of each sublayer can be varying along the wall, as is the case for both Fig. 59 (a) and (b). A careful examination reveals that the extrusion layer becomes thicker while approaching the top of the tooth. And it also becomes thinner when it goes from the left corner to the right corner of the rub-groove. One may also notice that the outer sublayer is thinner than the inner one. This practice is often used to minimize the volume (three-dimensional) or area (two-dimensional) differences between neighboring cells. Regarding y^+, the thickness of the nearest sublayer to the wall is usually very thin compared to the size of the bulk cells. So other sublayers, growing thicker in the direction away from the wall, are created as a buffer. This helps diminish the volume or area difference between neighboring cells.

4. Semi Three-Dimensional

To simulate the full circumference of the labyrinth seal, a three-dimensional domain is needed. OpenCFD can generate a three-dimensional grid by revolving a two-dimensional grid which is firstly generated. For cases where radial eccentricity occurs between the rotor and stator, simple revolution, which leads to a concentric grid, is not adequate. To this end, OpenCFD allows the user to control through the input script the path of each vertex in the two-dimensional grid to be revolved. Figure 60 shows 90-degree coverage of such a three-dimensional grid. The starting two-dimensional grid, hidden at the bottom, is like the one shown in Figure 59 (a) which has no stretching. To get a grid with eccentricity, the revolving path of each vertex is controlled. Consequently, the grid stretches along the revolving path other than the

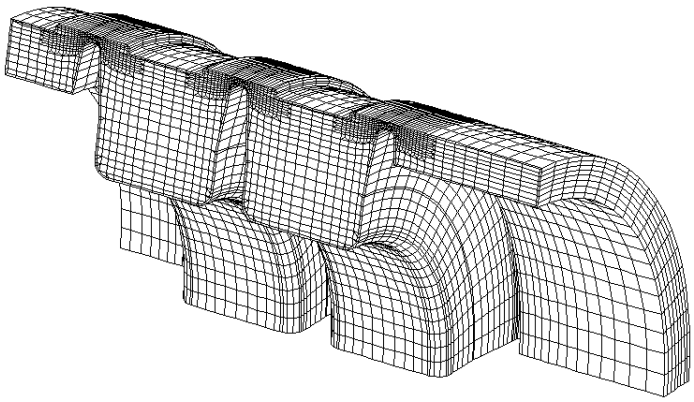

Fig. 60. A 90-degree coverage of a three-dimensional grid with a large aspect-ratio.

starting plane. As one can see in Fig. 60 the grid in the ending plane, visible at the top, is significantly stretched. A magnified view of the ending plane is shown in Fig. 61.

5. Embedding Refinement

To increase local density, embedding refinement is often applied to the grid. It has the advantage of refining only the location where necessary. Figure 59 (a) shows the embedding refinement on the regions surrounding the teeth. One may note, between the refined cells and the surrounding cells, triangular cells are used along the boundary of the refinement regions. This is to eliminate hanging vertices that would be generated otherwise. Hanging vertices are disfavored in terms of compatability which is of high priority to this grid generator. Since cells with hanging vertices invole extra work to calculate the flux to and from the neighboring cells, each CFD code, has its own way to handle them. There is no general treatment of hanging vertices shared by different CFD codes. To maximumize the compatibility and also to eliminate the extra work due to hanging vertices, hanging vertices are eliminated from the grid generator OpenCFD. Without hanging vertices the OpenCFD grid provides users the

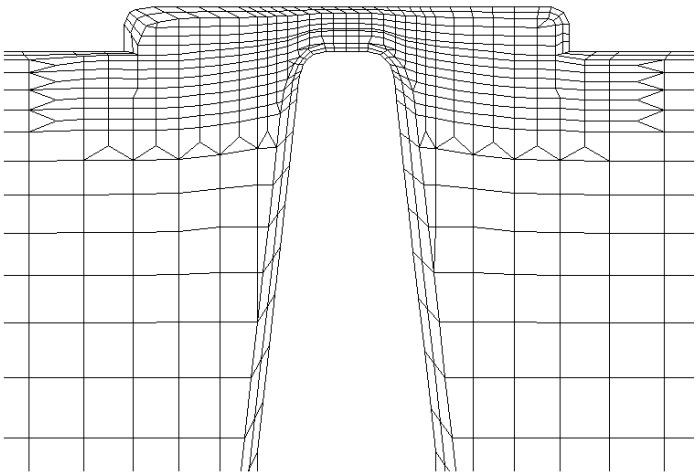

Fig. 61. A magnified view of the grid around a tooth tip showing grid stretching.

flexibility of working with different CFD codes, for example Fluent, STAR-CD and CFX.

6. Grid Density Control

Apart from the embedding refinement, OpenCFD also has control over the global grid distribution. As shown in Fig. 59 (b), the grid density increases from the left side to the labyrinth tooth center, and then experiences several decreasings and increasings from the tooth center to the right. Figure 59 (b) also shows that the grid becomes coarser and coarser as one traverses away from the boundaries. For a two-dimensional grid, the global distribution is controlled through the background grid.

For a fully three-dimensional domain, the rotor radius is often about 1000 times as large as the clearance. If the same grid density is used in all the three directions, there will be too many cells. For labyrinth seals considered in the present study, the flow in the circumferential direction is fairly uniform allowing a much coarser circumferential grid density, thus saving a great quantity cells. The cells of such grids

will have a huge aspect ratio and would be hard for other grid generators to generate.

B. OpenCFD Capabilities

Considering the nature of the geometry and flow involved in the current research, the following capabilities are implemented for the grid generator OpenCFD.

1. CAD Integrated

OpenCFD reads the geometry from a CAD file in DXF (Data eXchange Format) format. DXF is a standard format for a 2D geometry, and it is maintained by Autodesk. Though it is proprietary, it is fully open to the public. Due to the wide use of Autodesk products, DXF became a de facto two-dimensional CAD standard. It is supported by all the mainstream CAD products, such as AutoCAD and SolidWorks, as well as some free CAD codes such as QCAD. For information about how to use these software packages, please refer to the documentation provided with them.

Currently OpenCFD supports two versions of DXF: DXF 2000 and DXF 2004. Other versions may also be compatible with OpenCFD, but no test has been done so far.

2. Automatic and Programmable

To conduct the current labyrinth seal investigation, it is necessary to run a large number of cases which are similar in the computational domain and boundary conditions. To improve grid generation efficiency, OpenCFD automates the whole grid generation process. As a first step, the user writes an input script which specifies what the grid will be like. After that OpenCFD generates a grid accordingly, without any manual intervention. A simple input script can be as short as a few lines, such as the one

shown below.

```
# ---------------------- A Sample Script -----------------------------
# A very preliminary script for OpenCFD to generate a 2D grid
# For more info, please refer to the doc or visit http://opencfd.sf.net
# All Rights Reserved!  Jinming Xu jxu@opencfd.org
import geom                      #import module
geom.get("rub.dxf")              #read geometry
geom.shrink([6])                 #shrink geometry with certain thickness

import grid                      #import module
refnZone = [(2,2), (260,300), (420,300), (420,400), (260,400)]
grid.refine([refnZone])
grid.cart(30,25)                 #create Cartesian grid
grid.addExtrLayer(2,0.8)         #add extrusion layer
grid.save("adv2d.cgns")           #save grid
```

Since for each investigation in the present research, the cases involved are very similar in geometry and boundary conditions, the same script can be used for every grid generation with few adjustments. In this way, the grid can be produced quickly.

3. Generating CGNS Compliant Grid

To ensure compatibility with other CFD packages, OpenCFD outputs its grids in CGNS format. CGNS denotes CFD General Notation System. As its name suggests, it is intended to serve as a general CFD format for all CFD software. It was first proposed by AIAA and is very likely to be an ISO standard in the years to come. More details are available on its official website at http://www.cgns.org. Writing grids in

CGNS format enables OpenCFD to communicate to all the popular CFD packages, such as STAR-CD, Fluent, CFX, ICEM-CFD, ABAQUS and ANSYS. For details on how to import and export grids in CGNS format, please refer to the documentation available with those software packages.

C. Grid Generation Procedure

OpenCFD is implemented in C++, with Python as the scripting language. It is also object-oriented and cross platform, being able to run on Windows and most UNIX variants. The methodology that OpenCFD employs to generate a grid is mainly based on the idea of vertex moving, cell cutting and cell removal. Figure 62 gives the data flow chart for OpenCFD from the standpoint of a user. As the first step, the user needs to draw the geometry for the CFD domain with a CAD software package, such as SolidWorks, AutoCAD or QCAD. Then the user needs to write an input script in Python to instruct OpenCFD on what kind of grid is to be generated. When the script is ready, the user can run OpenCFD. Seconds or minutes later, a grid will be generated in CGNS format. And now the user can import the grid into any of the mainstream commercial CFD and/or FEA software, such as STAR-CD, Fluent, CFX, ICEM-CFD, ABAQUS and ANSYS. From the standpoint of a developer, however, the process of generating a grid can be divided into several steps as follows.

1. Geometry Shrinking

If the extrusion layer is specified along the wall, which is the case in the present research, OpenCFD firstly shrinks the domain to reserve space for extrusion layer. After shrinking, the domain of course becomes smaller. The shrinked domain is the one that will actually be used to generate the preliminary grid. Figure 63 shows

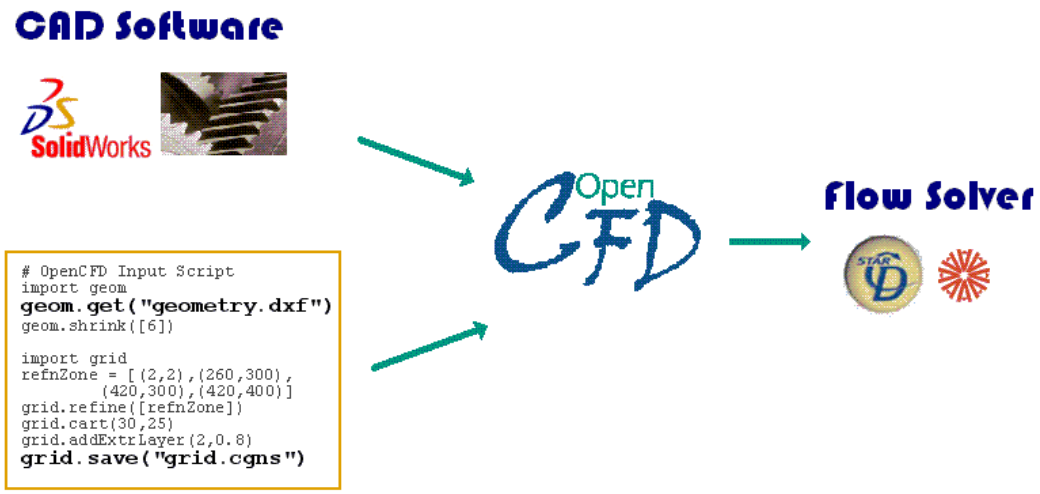

Fig. 62. Data flow chart for OpenCFD.

what the domain is like before and after the shrinking. The dotted lines show the original geometry, while the solid thick lines show the shrunk geometry. The space between the original and the shrunk domain forms a narrow closed band, where the extrusion layer is to be generated. The thickness of the band, also of the extrusion layer, is specified by the user. As one can see from Fig. 63, the shrinking is similar to scaling, but not the same. Scaling only affects the size, with the geometry preserved. But shrinking changes the size as well as the geometry. The width of the band can also vary, if needed. The user can control the width of the band through OpenCFD commands. A careful examination of Fig. 63 will show that the geometry of the shrunk domain is no longer the same as the original one.

2. Background Grid Generation

As the second step, OpenCFD generates a background grid, which covers the whole two-dimensional domain as illustrated in Fig. 64. The thick lines show the geometry of the CFD domain; while the thin ones show the background grid. If grid stretching

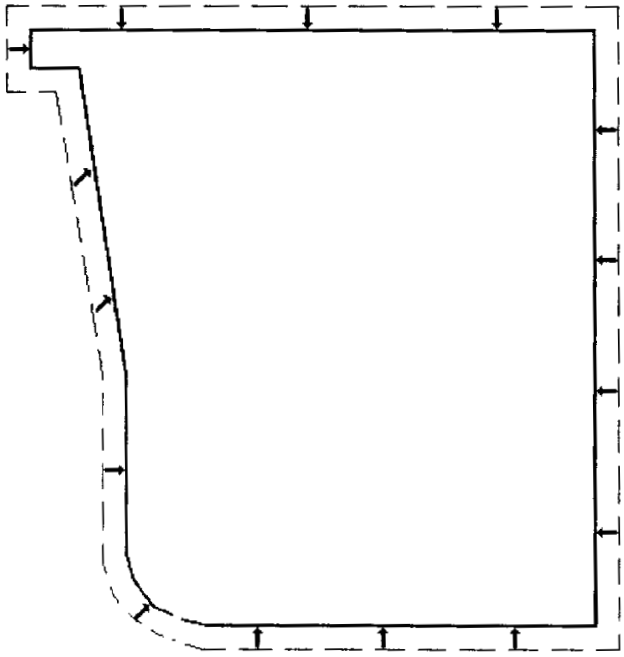

Fig. 63. Step 1: Shrinking the domain to prepare for the extrusion layer.

or embedding refinement is specified, it is applied to the initial background grid. Figure 64 shows an initial background grid without any grid control. It is structured, Cartesian and the bulk cells all have the same size. With stretching and embedding refinement applied, triangular and quadrilateral cells will be generated in the grid and the cells may no longer be uniform in size. More details on grid control will be discussed later.

3. Vertex Tuning

After the background grid is created, it is necessary to tune up the constituting vertices. Specifically, the tuning involves:

1. Moving vertices lying near the borders of the domain onto the borders.

2. Moving vertices lying near the domain corners to those corners. Vertex tuning

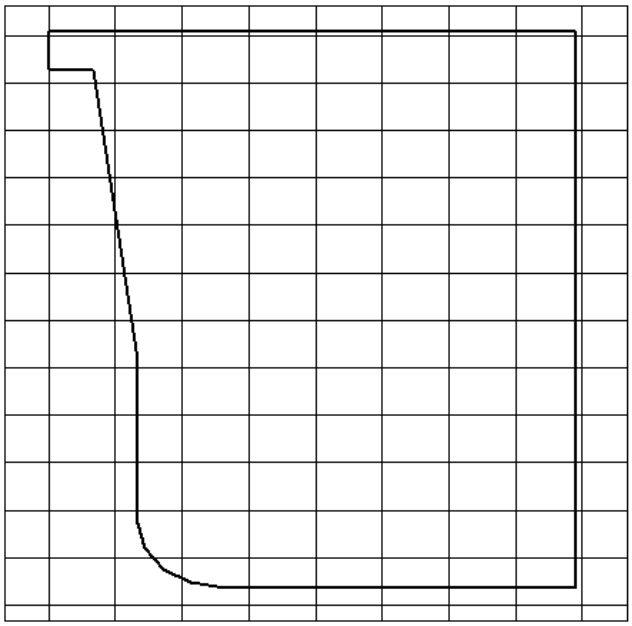

Fig. 64. Step 2: A background grid generated to cover the whole domain.

eliminates along the boundaries the small size cells that would be created otherwise. This is done to enhance the grid quality. A corresponding background grid with vertices tuned-up is shown in Fig. 65. As one may notice, only the vertices inside and on the boundary lines of the domain are actually moved. This is due to the fact that vertices outside the domain do not affect the final grid very much and thus are left unchanged.

4. Cell Cutting and Cell Removal

After the vertices have been tuned up, OpenCFD "cuts out" the grid from the background grid, based on the geometry of the CFD domain. After this step, a preliminary grid will be generated, as shown in Fig. 66.

This step consists of several separate actions:

1. Removing all cells outside of the domain

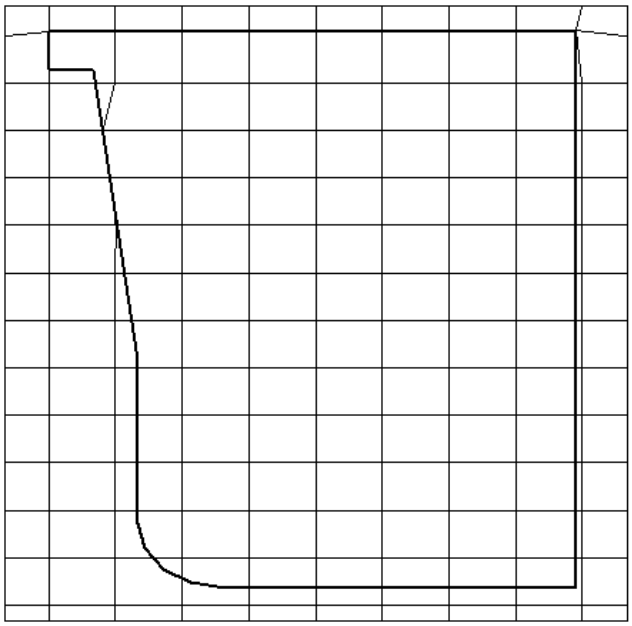

Fig. 65. Step 3: Background grid with vertices tuned.

2. Cutting out all cells lying across the domain boundaries. OpenCFD firstly figures out which portion of the cell is inside the domain and which portion outside, then erasing the portion outside the domain along the domain boundary lines and forming a new cell. After cell cutting, cells with five or more boundaries are possibly to be generated along the domain boundary.

3. Subdividing the cut-out cells generated in step 2 into quadrilateral or triangular cells if necessary. For the cells generated in step 2 whose geometry is neither quadrilateral nor triangular and whose boundary lines have hanging vertices, subdivision is needed. For the cells with hanging vertices along the boundary lines, subdivision will split the cells from the hanging vertices. Subdivision splits the cells recursively into either quadrilateral or triangular cells, to ensure the grid has no hanging vertices and no cells with other shapes. Since many CFD codes do not accept a grid with hanging vertices nor with cells other than

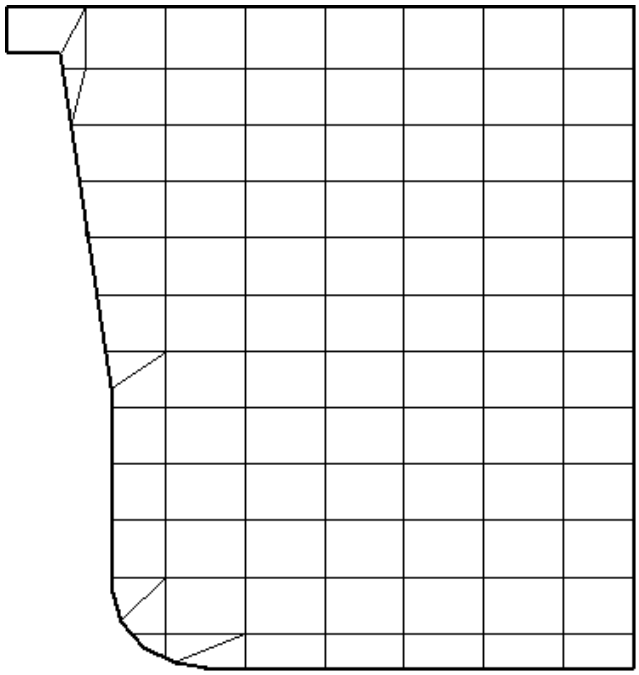

Fig. 66. Step 4: Preliminary grid created after cell cutting and cell removal.

triangular and quadrilateral, this step enhances the grid compatibility. Figure 66 shows the subdivision taken on five cells along the left boundaries.

5. Extrusion Layer Creation

The extrusion layer is created after the preliminary grid is available. As mentioned in the first step, the domain is shrinked to leave a space band around the geometry. This step is to fill that band with one or more layers of structured quadrilateral cells, termed the extrusion layer. After this step, the grid covers the entire original domain. Figure 67 illustrates how the grid looks after an extrusion layer is created. The extrusion layer in Fig. 67 has two layers of quadrilateral cells, the thickness of the outer sublayer being about 60 percent of the inner sublayer.

To create an extrusion layer, OpenCFD firstly figures out which vertices are on

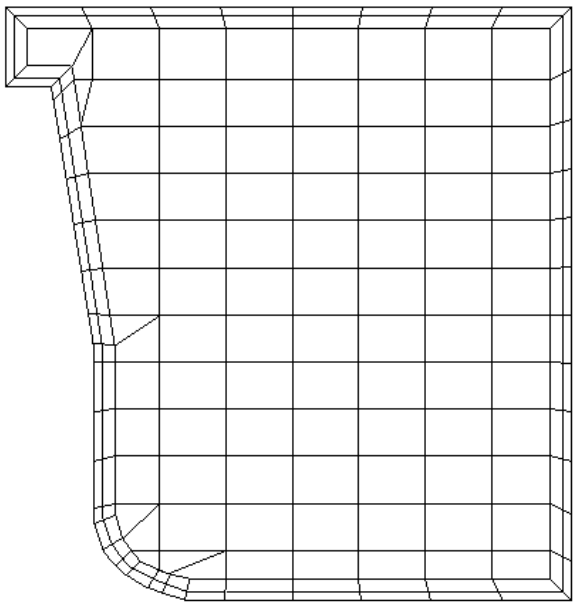

Fig. 67. Step 5: An extrusion layer added to the preliminary grid.

the boundaries by traversing all of them. Then it generates the vertices for each sublayer by copying the boundary vertices with a certain offset, which is calculated from the specifications for the extrusion layer written in the input script.

6. Cell Rearrangement along the Domain Boundaries

Now we have a grid that covers the entire domain. But some cells along the boundaries may have poor quality. To improve the quality, OpenCFD goes through those cells, deleting, merging and recreating some of them. In Fig. 67, there are two small cells on the upper left corner of the preliminary grid. Due to their small size, it decreases the grid quality somewhat. OpenCFD can rearrange these two cells. After rearrangement, the grid turns into that shown in Fig. 68. As one can see, those two cells are deleted and replaced with two much larger cells. Also the final grid is more uniform in cell size.

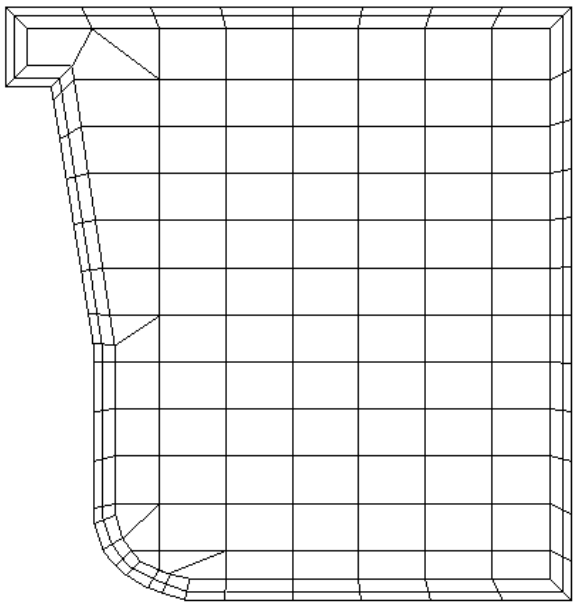

Fig. 68. Step 6: Final grid after rearranging some cells on the border of the domain.

D. Related Documents

To know more about OpenCFD, one can visit its official site at http://www.opencfd.org. As a whole set of documentation, the following documents are also available:

- OpenCFD User Guide
- OpenCFD Installation Guide
- OpenCFD Build Guide
- OpenCFD Commands
- OpenCFD Reference Manual

These documents are provided in both the PDF and HTML formats, downloadable from the official website. For more information about them, please visit the official website at http://www.opencfd.org.

CHAPTER VIII

SUMMARY, CONCLUSIONS AND RECOMMENDATIONS

Labyrinth seals are by far the most widely used sealing device in the turbomachine. Most labyrinth seals are designed with a very small clearance. However, a labyrinth clearance that is too tight can easily lead to rubbing and rotordynamic impacting of the rotating surface against the opposite surface. If the tooth is made from soft material, damage will occur on the labyrinth seal in various forms, such as bending and "mushrooming". On the other hand, if the surface opposite the labyrinth teeth is abradable, a rub-groove will form on the opposite surface.

This work numerically investigated the effect of damage and wear of the labyrinth seal on the turbomachinery flow and temperature field. Specifically, this work investigated: (1) the effect of rub-groove downstream wall angle on the leakage, (2) the effect of tooth bending damage on the leakage, (3) the effect of tooth "mushroom" damage on the leakage, and (4) the effect of rub-groove axial position and wall angle on the gas turbine ingress heating. To facilitate the grid generation for the above research, an unstructured grid generator was also developed.

The following sections summarize the findings and conclusions from the above investigation that was described in the previous chapters.

A. Effect of Rub-Groove Downstream Wall Angle on Leakage of Labyrinth Seals

The effect of groove downstream wall angle for a stepped labyrinth seal on compressible flow leakage was numerically investigated. The rub-groove under investigation had a fixed axial length and radial depth. The computation was conducted on a three-tooth, stepped labyrinth seal with air as the fluid.

Specific findings are summarized as follows:

1. The rub-groove wall angle α significantly affects the flow leakage, varying with tooth axial position and seal pre-rub clearance. This is due largely to the after-rub (minimum) clearance resulting from the rub-groove wall angle and the tooth tip axial and radial position. However, the after-rub (minimum) clearance does not solely determine the leakage. For cases with equal after-rub clearance, leakage variations were definitely observed.

2. The rub-groove wall angle α also affects the flow pattern. For fixed tooth axial position and fixed pre-rub clearance, the flow pattern typically changes fairly gradually with α. However, for certain cases of tooth axial position and pre-rub clearance, the flow pattern changes sharply from $\alpha = 0^o$ to $\alpha = 45^o$.

B. Effect of Tooth Bending Damage on Leakage of Labyrinth Seals

The effect of pure permanent tooth bending damage on the leakage of labyrinth seals, was numerically investigated. The computation was conducted on a three-tooth, straight-through labyrinth seal with air as the fluid.

Based on the cases considered, specific findings are summarized as follows:

1. Permanent tooth bending damage gives a significant leakage increase over the undamaged teeth. The leakage increase caused by tooth bending damage is due largely to the increase of the after-bend clearance, although it is also affected by the bending angle and the overall curvature of the bent teeth.

2. For a fixed operating clearance, the bent tooth cases give more leakage than the unbent cases. This is apparently due to the effect of tooth bending shape on the turbulence energy distribution.

C. Effect of Tooth Tip Mushroom Damage on Leakage of Labyrinth Seals

The effect of mushrooming damage on the leakage of labyrinth seal was numerically investigated. The computation was conducted on a three-tooth, straight-through labyrinth seal with air as the fluid.

Based on the cases considered, the specific findings are summarized as follows:

1. The mushrooming damage significantly increases the leakage of the labyrinth seal compared to that of the pre-damage seal. The leakage increase is due largely to the increase of after-damage clearance.

2. A mushroomed labyrinth seal also gives significantly higher leakage than that of an undamaged seal operating at the same clearance. This is attributed to the fact that the mushroomed tooth tip has a sharply curved surface that affects the turbulence kinetic energy.

3. For any fixed after-damage clearance c_{ad}, a larger mushroom radius always gives a higher leakage for the bent and unbent teeth alike.

4. The leakage increase caused by mushroom damage is influenced by the presence of tooth bending. For any fixed after-damage clearance c_{ad}, a mushroomed tooth with bending always gives a lower leakage compared to a mushroomed tooth without bending, regardless of the mushroom radius.

D. Effect of Rub-Groove Axial Position and Wall Angle on Gas Turbine Ingress Heating

The effect of rub-groove axial position and wall angle of a three-tooth labyrinth seal on the gas turbine wheelspace heating due to hot gas ingress was numerically investigated. The three-tooth labyrinth seal studied herein is located slightly inward of the

middle cavity of the turbine wheelspace, which is divided into inner, middle and outer cavities. Two different rub-groove wall angles, $\alpha = 15^o$ and $\alpha = 45^o$, are studied along with rub-groove axial positions 1 through 4 with d^* of 5.8×10^{-3}, 4.9×10^{-3} 4.2×10^{-3} and 2.7×10^{-3}, respectively.

For the cases considered here, the effects of labyrinth seal rub-groove axial position and wall angle are summarized as follows:

1. Both the rub-groove wall angle and axial position have an effect on the flow pattern, temperature and pressure field of the outer wheelspace cavity. Further, they have only a slight effect on the middle cavity. Specifically, for the outer cavity, the ingress, temperature and flow fields are substantially affected by the rub-groove axial position and mildly effected by the rub-groove wall angle, depending on the rub-groove axial position.

2. The bulk temperature in the outer cavity decreases with increasing rub-groove axial position number, i.e. decreasing d^*, for a fixed rub-groove wall angle. For the two rub-groove wall angles, the wall angle of $\alpha = 15^o$ gives a slightly higher bulk temperature than does $\alpha = 45^o$ with rub-grooves at positions 2, 3 and 4 in the outer cavity, while both angles give almost the same temperature at position 1.

3. The bulk temperature is ultimately determined by the purge-coolant flow entering through the middle labyrinth seal to the wheelspace. Because the pressure drop across the labyrinth seal is fixed, the purge-coolant flow rate is determined by the rub-groove wall angle and axial position. The more purge-coolant flow that is allowed by a particular rub-groove wall angle and axial position, the lower the bulk temperature in the outer wheelspace cavity.

4. The rub-groove axial position, and somewhat the wall angle, significantly alters the circumferential temperature distribution in the outer cavity. The magnitude as well as the shape of the circumferential temperature distribution is affected.

5. The rub-groove axial position also affects the axial temperature distribution in the outer cavity. It generally shows a higher temperature and more temperature variation with rub-groove position near the stator than near the rotor. The variation is also substantially influenced by whether the outer single-tooth labyrinth is tooth-on-rotor (TOR) or tooth-on-stator (TOS). Compared to TOR, TOS tends to reduce the higher temperature near the rotor and to increase that near the stator, thus giving a more uniform axial distribution for data planes 6 through 8, for example.

E. Grid Generator Development

To facilitate the grid generation for the aforementioned investigation, an unstructured grid generator was developed. It is capable of generating grids quickly and efficiently for the labyrinth seal. The grid generator is developed in C++, with embedded Python as the scripting language.

The methodology employed by this grid generator can be described as follows: (1) generating a Cartesian background grid based on the two-dimensional geometry, (2) tuning the vertices to avoid sliver or tiny cells that would later be created otherwise, (3) cutting or removing cells around the boundary lines of the geometry, (4) creating an extrusion layer for the wall boundaries.

The generated grid is hybrid, dominated by the Cartesian cells. Quadratic cells for the extrusion layer are created along the wall. Triangular cells are generated: (1) as fillers between the extrusion layer and inner Cartesian cells and (2) to body-fit the

non-wall boundaries. The grid preserves the geometry details for the labyrinth seal reasonably well. To control the grid density, the grid generator utilizes embedded refinement and grid stretching. The grid is saved in CGNS format, and is compatible with most popular commercial CFD codes.

F. Conclusions

It was found that the damage and wear of the labyrinth seal significantly affect the leakage and temperature field, as well as the flow pattern. This leakage increase is due largely to the altered clearance caused by the damage and wear. The leakage generally increases faster than linearly with the after-damage clearance. However, the specific configuration of the damage and wear, as well as the labyrinth seal itself, were also found to be important.

Specifically:

1. For the rub-groove, the downstream wall angle significantly affects the leakage as well as the flow pattern, varying with tooth relative axial position and seal pre-rub clearance.

2. For bending damage, the bending curvature and the percentage of tooth length that is bent were also found to be important to the leakage.

3. For the "mushrooming" damage, the mushroom radius and tooth bending also have an effect on the leakage.

When the labyrinth seal was applied to the turbine wheelspace cavity, it was found that the rub-groove axial position, and somewhat the wall angle, significantly alter the temperature, both its magnitude and its axial and circumferential distributions.

G. Recommendations for Further Work

Based on the gained understanding from the present work and the available literature, recommendations for further work are made in the following subsections.

1. Effect of Labyrinth Seal Damage on Efficiency of Entire Turbine or Compressor

Several forms of labyrinth seal damage are investigated in this thesis. As the results show labyrinth seal operating damage significantly increases the leakage of labyrinth seal, and thus decreases the efficiency of the entire turbine or compressor. To reduce the labyrinth seal damage and hence the efficiency loss, an alternative for the designer is to use a larger initial clearance in an attempt to avoid this substantial tooth damage during operation. But on the other hand, a large initial clearance will give a relatively lower efficiency from the very beginning.

Further work is recommended to investigate, under a variety of typical operating conditions, the probability of various degrees of damage for each form of labyrinth seal damage. Further work is also recommended to study the effect of labyrinth seal damage on the efficiency of the entire turbine or compressor, rather than the efficiency of labyrinth seal only.

2. Mechanism and Process of Labyrinth Seal Damage

When the labyrinth tooth rubs against the opposite surface, it incurs damage either on the labyrinth tooth or on the surface. The eventual form and intensity of labyrinth damage depends on many factors. For example, if intense heating occurs during a fierce rubbing [23], the tooth tip is likely to melt or become mushroomed. Further work is recommended to gain enhanced understanding on the rubbing mechanism and process, in order to better predict and minimize the labyrinth seal damage.

3. Rim-Cavity Ingress Heating with Heat Transfer and Transient Flow

In order to isolate for study the effect of labyrinth seal rub-grooves on ingress heating, the present work investigated the temperature field in the rim-cavity by assuming adiabatic walls. Adiabatic walls have been assumed by almost all researchers in studying the rim-cavity ingress heating. One reason is large uncertainty in estimating Nusselt number distribution and boundary condition around the rim-cavity walls. This is due largely to the complexity of the turbine system. Another reason is that it is extremely hard to measure the heat transfer at the rim-cavity wall, due to the compact size and velocity of the rim-cavity. Experimental work giving complete Nusselt number distributions on rim-cavity is recommended. This will help to better understand heat transfer and temperature distribution inside the rim-cavity. It will also help numerical simulation by allowing more complete CFD validation.

Like nearly all rim-cavity studies, the present work investigates the steady-state flow. Further work is also recommended, both on experimental side and CFD side, to study the transient flow inside the rim-cavity. This further work on the CFD side will help to more accurately predict the rim-cavity flow and temperature filed. The further work on the experimental side will provide more guidance and validation for the numerical simulation.

4. Code Validation

As discussed in Chapter II, CFD predictions are compared with experiments and reasonably good agreement with experiments were found. The parameters chosen to be compared are labyrinth seal leakage and scalar concentration in the wheelspace. Further, an extensive and detailed grid independence study was conducted for each category of this investigation. However, it is desirable to have more detailed ex-

perimental data, so the CFD predictions can be compared with the experiments on the level of local flow field details. Further work on code validation is recommended when detailed experimental data become available for the local distributions of velocity, temperature and turbulence kinetic energy etc, especially along the labyrinth tooth boundaries and in the tooth clearance. Further work is recommended to obtain these experimental data. Specifically, the following work on code validation is recommended:

1. Further work is recommended to compare the CFD prediction with experiments in terms of local velocity and turbulence kinetic energy fields etc, once the detailed information for these parameters are available. The regions of special interest include the boundary around labyrinth tooth, the slot between the labyrinth tooth and its opposite surface. Due to the compactness of labyrinth seal, very little information on the local distributions, especially along the labyrinth tooth boundary, is available. Dimensionless measurements near the tooth surface are possible in an extremely large scale water model, for example.

2. Further work is also recommended to compare the CFD predictions of damaged labyrinth seal to the experimental data of damaged labyrinth seals. For the damaged labyrinth seal, there are no quantitative measurements available so far. Once the detailed measurements for the damaged labyrinth seals are available, more code validation is recommended for the damaged labyrinth seals.

3. For the rim-cavity ingress heating, further code validation is especially recommended for the heat transfer and temperature distribution. Due to the compact size and complexities of the turbine engine, it is extremely hard to measure the heat transfer coefficient along the rim-cavity wall. It is also extremely difficult to measure the temperature under operation, since the temperature is very

high and in many places above or close to the metal melting point. Comparison of temperature and heat transfer coefficient between CFD and experiments is recommended when these experimental data become available.

NOMENCLATURE

A	leakage flow area, m^2
	mean annulus flow angle from axial direction [^{o}]
C_D	discharge coefficient
c^*	labyrinth seal tooth radial clearance non-dimensionalized
	by the radius of the domain (main) inlet stator surface
D	shaft diameter, mm
d^*	axial position of rub-groove non-dimensionalized
	by the radius of the (main) domain inlet stator surface
L_p	tooth pitch, mm
L_t	tooth height, mm
$\dot{m}$	(purge-coolant) leakage rate, kg/s
$\dot{m}_0$	leakage rate of the baseline labyrinth seal, kg/s
$\dot{m}^*$	mass flow rate non-dimensionalized
	by compressor inlet mass flow rate
$\dot{m}^*_{fs}$	feed slot coolant mass flow rate non-dimensionalized
	by compressor inlet mass flow rate
$\dot{m}^*_{il}$	inner labyrinth mass flow rate non-dimensionalized
	by compressor inlet mass flow rate
$\dot{m}^*_{rh}$	receiver hole mass flow rate non-dimensionalized
	by compressor inlet mass flow rate
$\dot{m}^*_{tc}$	total coolant mass flow rate non-dimensionalized
	by compressor inlet mass flow rate
N	number of nozzle guide vanes
h	static enthalpy

k	turbulence kinetic energy
n	number of teeth
P	pressure, Mpa
P_{ref}	reference pressure of mainstream domain exit (see Fig. 2)
P^*	pressure non-dimensionalized as (P-P$_{ref}$)/P$_{ref}$
Δp	peak-to-valley amplitude of the mainstream pressure variation
Re	leakage Reynolds number, $2\dot{m}/(\pi\mu D)$
R	radius, mm
	gas constant, J/(kg·K)
R^*	radius, non-dimensionalized
	by the radius of the (main) domain inlet stator surface
R_b^*	bending radius, non-dimensionalized
	by the radius of the (main) domain inlet stator surface
R_m^*	mushrooming radius, non-dimensionalized
	by the radius of the (main) domain inlet stator surface
r, θ, z	radial, circumferential and axial coordinates
	in cylindrical coordinate system
r^*	radius non-dimensionalized by the radius of
	the (main) domain inlet stator surface
S^*	distance between the tooth centerline to the arc center of
	the curled tooth tip non-dimensionalized by the radius of
	the (main) domain inlet stator surface
s	source term; labyrinth seal step height, mm
T^*	temperature non-dimensionalized by compressor exit
	temperature (wall values are adiabatic wall temperature)

T^*_{max}	maximum temperature non-dimensionalized by compressor exit temperature
TE^*	Turbulent kinetic Energy non-dimensionalized as $TE^* = TE/(RT_u)$
U^*	Unbent length of damaged tooth non-dimensionalized by the radius of the (main) domain inlet stator surface
u	velocity in shaft axis direction, m/s
v	velocity in radial direction, m/s
v_z	axial velocity in potential flow solution
v_θ	circumferential velocity in potential flow solution
W	labyrinth tooth width, mm
z_0	distance from nozzle guide vane trailing edge

Greek Characters

α	groove downstream wall slope angle
β	bend angle
δ	polar coordinate in bending coordinate system, rad
κ	Von Karman constant onstant
π	pressure ratio ($P_{t,u}/P_{s,d}$)
ρ	density, kg/m^3
ϵ	turbulence kinetic energy dissipation rate
λ	thermal conductivity
ω	shaft rotating speed, rad/s
τ	shear stress
μ	dynamic viscosity, Pa·s

Subscripts

0	baseline
ab	after-bend
ad	after-damage
ar	after-rub
b	bending
d	downstream
eff	effective
f	finer grid
h	static enthalpy
i	inner, momentum
m	mass, mushrooming
o	outer
p	pitch
pb	pre-bend
pd	pre-damage
pr	pre-rub
r	root, radial
s	static
sh	shaft
T	turbulence
t	total, tip
u	upstream
w	wall
z	axial

θ	circumferential

Abbreviations

CFD	Computational Fluid Dynamics
NGV	Nozzle Guide Vane
RANS	Reynolds Averaged Navier-Stokes
TE	Turbulent kinetic Energy
TOR	Tooth On Rotor
TOS	Tooth On Stator

REFERENCES

[1] H. M. Martin, "Labyrinth packings," *J. Engineering*, vol. 85, pp. 33–36, 1908.

[2] A. Egli, "The leakage of steam through labyrinth seals," *Trans. ASME*, vol. 57, pp. 115–122, 1935.

[3] W. J. Kearton and T. H. Keh, "Leakage of air through labyrinth glands of the staggered type," in *Proc. Inst. Mech. Eng.*, 1952, vol. 166, pp. 180–188.

[4] V. Schramm, K. Willenborg, S. Kim, and S. Wittig, "Influence of a honeycomb-facing on the flow through a stepped labyrinth seal," *ASME J. Eng. Gas Turbines Power*, vol. 124, pp. 140–146, 2002.

[5] S. Wittig, L. Dorr, and S. Kim, "Scaling effects on leakage losses in labyrinth seals," *ASME J. Eng. Power*, vol. 105, pp. 305–309, 1983.

[6] R. C. Bill and L. T. Shiembob, "Friction and wear of sintered fiber-metal abradable seal materials," NASA, Tech. Rep., NASA TM X73650, June 1977.

[7] J. A. Demko, G. L. Morrison, and D. L. Rhode, "Effect of shaft rotation on the incompressible flow in a labyrinth seal," *J. Propulsion*, vol. 6, pp. 171–176, 1990.

[8] P. A. E. Steward and K. A. Brasnett, "The contribution of x-ray to gas turbine air sealing technology," in *Proc. AGARD Conf.*, Amsterdam, The Netherlands, 1978, vol. 237, pp. 10.1–10.13.

[9] H. L. Stocker, D. M. Cox, and G. F. Holle, "Aerodynamic performance of conventional and advanced design labyrinth seals with solid-smooth, abradable and honeycomb lands," Detroit Diesel Allison, Division of GMC, Indianapolis, Indiana, Tech. Rep., NASA-CR-135307, 1977.

[10] H. Zimmerman, A. Kammerer, and K. H. Wolff, "Performance of worn labyrinth seals," in *Proc. of ASME Turbo Expo 1994*, The Hague, The Netherlands, June 1994, ASME Paper 94-GT-131.

[11] Z. Yu and D. W. Childs, "Experimental rotordynamic coefficient and static characteristic results for a labyrinth rotor running against a grooved stator with l/d = 0.466 cr/c = 0.0036, mechanical engineering department," Turbomachinery Laboratories, Texas A&M University, College Station, Texas, 1995.

[12] D. L. Rhode and B. F. Allen, "Visualization and measurements of rub-groove leakage effects on straight-through labyrinth seals," in *Proc. of ASME Turbo Expo 1998*, Stockholm, Sweden, June 1998.

[13] D. L. Rhode and B. F. Allen, "Measurement and visualization of leakage effects of rounded teeth tips and rub-grooves on stepped labyrinths," *ASME Journal Of Engineering For Gas Turbines and Power*, vol. 123, pp. 604–611, 2001.

[14] J. Denecke, V. Schramm, S. Kim, and S. Wittig, "Influence of rub-grooves on labyrinth seal leakage," *Journal of Turbomachinery*, vol. 125, pp. 387–393, 2003.

[15] D. L. Rhode and R. G. Adams, "Computed effects of rub-groove size on stepped labyrinth seal performance," *STLE Tribology Transactions*, vol. 44, pp. 523–532, 2001.

[16] D. L. Rhode and R. G. Adams, "Rub-groove width and depth effects on flow predictions for straight-through labyrinth seals," *ASME Journal of Tribology*, vol. 126, pp. 781–787, 2004.

[17] R. E. Chupp, F. Chasripoor, and G. D. Moore, "Applying abradable seals to industrial gas turbines," AIAA paper 2002-3795, June 2002.

[18] P. Dowson, , M. S. Walker, and A. P. Watson, "Development of abradable and rub tolerant seal materials for application in centerifugal compressors and steam turbines," in *Proc. of the 33rd Turbo Symposium*, Houston, Texas, Sept. 2004.

[19] J. Xu, M. S. Ambrosia, and D. L. Rhode, "Effect of rub-groove wall angle on the leakage of abradable stepped labyrinth seals," *Tribology Transactions*, vol. 48, pp. 443–449, 2005.

[20] J. K. Whalen and J. R. Dugas, "Upgrading centrifugal compressors with polymer seals in an ethylene plant – a case history," in *Proc. of the 29th Turbo Symposium*, Houston, Texas, Sept. 2000.

[21] J. K. Whalen, E. Alvarez, and L. P. Palliser, "Thermoplastic labyrinth seals for centrifugal compressors," in *Proc. of the 33rd Turbo Symposium*, Houston, Texas, Sept. 2004.

[22] S. L. Ross and R. F. Beckinger, "Compressor seal selection and justification," in *Proc. of the 32nd Turbo Symposium*, Houston, Texas, Sept. 2003.

[23] F. Ghasripoor, N. A. Turnquist, and M. Kowalczyk, "Wear prediction of strip seals through conductance," in *Proc. of ASME Turbo Expo 2004*, Vienna, Austria, June 2004.

[24] F. J. Bayley and J. M. Owen, "The fluid dynamics of a shrouded disk system with a radial outflow of coolant," *ASME Journal of Engineering for Power*, vol. 92, pp. 335–341, 1970.

[25] Chew, J. W., Dadkhan, S., and A. B. Turner, "Rim sealing of rotor-stator wheelspaces in the absence of external flow," in *Proc. of ASME Turbo Expo 1991*, Orlando, Florida, June 1991.

[26] V. I. Khilnani, L. C. Tsai, and S. H. Bhavnani, "Mainstream ingress suppression in gas turbine disk cavities," *Journal of Turbomachinery*, vol. 116, pp. 339–346, 1994.

[27] N. Kobayashi, M Matsumoto, and M. Shizuya, "Conservation form of the navier-stokes equations in general nonsteady coordinates," *AIAA Journal*, vol. 106, pp. 136–141, 1984.

[28] U. P. Phadke and J. M. Owen, "Aerodynamic aspects of the rim sealing of gas turbine rotor-stator systems, parts 1.3," *Int. J. Heat Fluid Flow*, vol. 9, pp. 98–117, 1988.

[29] K. Hamabe and K. Ishida, "Rim seal experiments and analysis of a rotor-stator system with nonaxisymmetric main flow," in *Proc. of ASME Turbo Expo 1992*, Cologne, Germany, July 1992.

[30] J. W. Chew, T. Green, and A. B. Turner, "Rim sealing of rotor-stator wheelspaces in the presence of external flow," in *Proc. of ASME Turbo Expo 1994*, Vienna, Austria, June 1994.

[31] R. P. Roy, G. Xu, and J. Feng, "Study of main-stream gas ingestion in a rotor-stator disk cavity," AIAA Paper 2000-3372, July 2000.

[32] R. P. Roy, G. Xu, J. Feng, and S. Kang, "Pressure field and main-stream gas ingestion in a rotor-stator disk cavity," in *Proc. of ASME Turbo Expo 2001*, New Orleans, Louisiana, June 2001, ASME Paper 2001-GT-564.

[33] J. M. Feiereisen, R. E. Paolillo, and J. Wagner, "Utrc turbine rim seal ingestion and platform cooling experiments," AIAA paper 2000-3371, June 2000.

[34] D. Bohn, E. Johann, and U. Kruger, "Experimental and numerical investigations of hot gas ingestion in rotor-stator systems with superimposed cooling mass flow," *Journal of Turbomachinery*, June 1995.

[35] D. E. Bohn, B. Rudzinski, N. Surken, and W. Gartner, "Experimental and numerical investigation of the influence of rotor blades on hot gas ingestion into the upstream cavity of an axial turbine stage," in *Proc. of ASME Turbo Expo 2000*, Munich, Germany, May 2000, ASME paper 2000-GT-284.

[36] B. Johnson, G. Mack, R. Paolillo, and W. Daniels, "Turbine rim seal gas path flow ingestion mechanisms," Indianapolis, Indiana, June 1994, AIAA Paper 1994-2703.

[37] K. Teramachi, T. Manabe, N. Yanagidani, and T. Fujimura, "Effect of geometry and fin overlap on sealing performance of rim seals," AIAA Paper 2002–3938, July 2002.

[38] Y. Okita, M. Nishiura, S. Yamawaki, and Y. Hironaka, "A novel cooling method for turbine rotor-stator rim cavities affected by mainstream ingress," in *Proc. of ASME Turbo Expo 2004*, Vienna, Austria, June 2004, ASME Paper GT2004-53016.

[39] A. V. Mirzamoghadam and Z. Xiao, "Flow and heat transfer in an industrial rotor-stator rim sealing cavity," *Journal of Engineering for Gas Turbines and Power*, vol. 124, pp. 125–132, 2002.

[40] D. Choiand D. L. Rhode and A. Mirzamoghadam, "Labyrinth seal design change to reduce rim seal coolant," AIAA Paper 2004-3572, July 2004.

[41] K. Teramachi, M. Hamabe, T. Manabe, and N. Yanagidani, "Experimental and

numerical investigation of sealing performance of turbine rim seals," in *Proc. of the International Gas Turbine Congress*, Tokyo, Japan, Nov. 2003, IGTC2003 Tokyo TS-025.

[42] R. P. Roy, G. Xu, and Y. Zhao, "A study of flow field in a model rotor-stator disk cavity," in *Proc. of ASME Turbo Expo 1999*, Indianapolis, Indiana, June 1999, ASME Paper 1999-GT-246.

[43] O. Gentilhomme, N. J. Hills, A. B. Turner, and J. W. Chew, "Measurement and analysis of ingestion through a turbine rim seal," *Journal of Turbomachinery*, vol. 125, pp. 505–512, 2003.

[44] N. J. Hills, J. W. Chew, and A. B. Turner, "Computational and mathematical modeling of turbine rim seal ingestion," *Journal of Turbomachinery*, vol. 124, pp. 306–315, 2002.

[45] B. Laumert, H. Martensson, and T. H. Fransson, "Simulation of rotor/stator interaction with a 4d finite volume method," in *Proc. of ASME Turbo Expo 2002*, Amsterdam, The Netherlands, June 2002, ASME paper GT-2002-30601.

[46] D. E. Bohn, A. Decker, H. Ma, and M. Wolf, "Influence of sealing air mass on the velocity distribution in and inside the rim seal of the upstream cavity of 1 1.5-stage turbine," in *Proc. of ASME Turbo Expo 2003*, Atlanta, Georgia, June 2003, ASME Paper GT2003-38368.

[47] C. Cao, J. W. Chew, P. R. Millington, and S. I. Hogg, "Interaction of rim seal and annulus flows in an axial turbine," in *Proc. of ASME Turbo Expo 2003*, Atlanta, Georgia, June 2003, ASME Paper GT2003-38368.

[48] R. Jakoby, T. Zierer, K. Lindblad, and J. Larsson, "Numerical simulation of the

unsteady flow field in an axial gas turbine rim seal configuration," AIAA Paper 2004-53829, June 2004.

[49] A. C. Benim, D. Brillert, and M. Cagan, "Investigation into the computational analysis of direct-transfer pre-swirl systems for gas turbine cooling," in *Proc. of ASME Turbo Expo 2004, June 14-17, 2004, Vienna, Austria*, June 2004, ASME paper GT-2004-54151.

[50] J. J. Quirk, "An alternative to unstructured grids for computing gas dynamics flows around arbitrarily complex two-dimensional bodies," *Comput Fluids*, vol. 23, pp. 125–142, 1994.

[51] R. Schneiders, "A grid-based algorithm for the generation of hexahedral element meshes," *Engineering with Computers*, vol. 12, pp. 168–177, 1995.

[52] R. Schneiders, R. Schindler, and F. Weiler, "Octree-based Generation of Hexahedral Element Meshes," in *Proc. of 5th International Conference on Numerical Grid Generation in Computational Field Simulations*, Mississippi State University, Starkville, Mississippi, 1996, pp. 205–216.

[53] R. Schneiders, "Refining Quadrilateral and Hexahedral Element Meshes," in *Proc. of 5th International Meshing Roundtable*, Pittsburgh, Pennsylvania, U.S.A., Oct. 1996, pp. 679–688.

[54] A. Nakano, N. Satofuka, and N. Shimomura, "A cartesian grid approach to compressible viscous flow computations," in *Computational Fluid Dynamics*, pp. 540–546. New York, John Wiley & Sons Ltd, 1996.

[55] K. F. C. Yiu, D. M. Greaves, and S. Cruz, "Quadtree grid generation: information handling, boundary fitting and cfd applications," *Comput Fluids*, vol. 25,

pp. 759–769, 1996.

[56] Z. J. Wang, "A quadtree-based adaptive cartesian/quad grid flow solver for navier-stokes equations," *Comput Fluids*, vol. 27, pp. 529–549, 1998.

[57] R. Schneiders, "Quadrilateral and hexahedral element meshes," in *Handbook of Grid Generation*, pp. 21–1 – 21–27. Boca Raton, Florida, CRC Press, 1999.

[58] L. P. Zhang and Z. J. Wang, "A block lu-sgs implicit dual time-stepping algorithm for hybrid dynamics meshes," *Comput Fluids*, vol. 33, pp. 891–916, 2004.

[59] M. W. Beall, J. Walsh, and M. S. Shephard, "Accessing CAD geometry for mesh generation," in *Proc. of 12th International Meshing Roundtable*, Santa Fe, New Mexico, Sept. 2003, pp. 33–42.

[60] R. E. Chupp, R. G. Loewenthal, and R. P. Menendez, "Advanced seal development for large industrial gas turbines," AIAA paper 1997-2731, June 1997.

[61] Z. V. A. Warsi, "Conservation form of the navier-stokes equations in general nonsteady coordinates," *AIAA Journal*, vol. 19, pp. 240–242, 1981.

[62] P. A. Libby and F. A. Williams, *Turbulent Reacting Flows*, Berlin, Germany, Springer Verlag, 1980.

[63] B. E. Launder and D. B. Spalding, "The numerical computation of turbulent flows," *Computer Methods in Applied Mechanics and Engineering*, vol. 3, pp. 269–289, 1974.

[64] Turner Green, "Effect of external flow on the sealing performance of rotor-stator rim seals," Ph.D. dissertation, University of Sussex, Sussex, United Kingdom, 1994.

[65] N. J. Hills, T. Green, A. B. Turner, and J. W. Chew, "Aerodynamics of turbine rim-seal ingestion," in *Proc. of ASME Turbo Expo 1994*, Orlando, Florida, June 1997, ASME Paper 97-GT-268.

VITA

Jinming Xu was born in Hunan, China in 1975. In 1998, he obtained his B.E. degree in Energy Engineering from Jiangsu Institute of Petrochemical Technology, which is now named Jiangsu Polytechnic University. In 2001, he obtained his M.E. degree in Engineering Mechanics from Tsinghua University. Then he moved to Texas A&M Univeristy and receivived his PhD degree in 2006. His research interests include Computational Fluid Dynamics and the more general Thermofluid area. Jinming Xu married Hongqin Shi in June 2001, enjoying two great daughters so far. He can be reached at his permanent mailing address:

c/o Dr. David Rhode

Department of Mechanical Engineering

Texas A&M University

College Station, TX 77843-3123